MICROCOPY RESOLUTION TEST CHART
NATIONAL BUREAU OF STANDARDS-1963-A

PHOTOGRAPH THIS SHEET

LEVEL

$\underline{III}$

INVENTORY

1

$\underline{DNA\text{-}TR\text{-}81\text{-}138}$ $\underline{1\ April\ 1982}$

DOCUMENT IDENTIFICATION

DISTRIBUTION STATEMENT A
Approved for public release;
Distribution Unlimited

DISTRIBUTION STATEMENT

ACCESSION FOR

NTIS	GRA&I	☒
DTIC	TAB	☐
UNANNOUNCED		☐
JUSTIFICATION		

BY
DISTRIBUTION /
AVAILABILITY CODES

DIST	AVAIL AND/OR SPECIAL	
A.1		

DISTRIBUTION STAMP

DTIC
COPY
INSPECTED
1

DTIC
SELECTED
MAY 2 1985
D

DATE ACCESSIONED

DATE RETURNED

85 05 01 035

DATE RECEIVED IN DTIC

REGISTERED OR CERTIFIED NO.

PHOTOGRAPH THIS SHEET AND RETURN TO DTIC-DDAC

DTIC FORM 70A
DEC 83

DOCUMENT PROCESSING SHEET
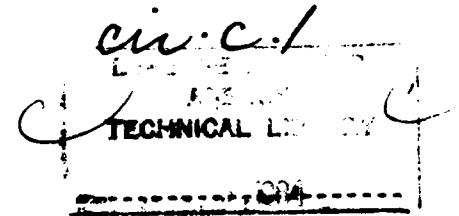
PREVIOUS EDITION MAY BE USED UNTIL
STOCK IS EXHAUSTED.

AD-A153 203

FUEL-AIR EXPLOSIVE NUCLEAR AIRBLAST SIMULATOR: INVESTIGATION OF SECONDARY WAVES

cir·c·l

TECHNICAL L.

T.H. Pierce
M.A. Groethe
S-CUBED, A Division of Maxwell Labs, Inc.
P.O. Box 1620
La Jolla, California 92038

1 April 1982

Technical Report

Prepared for

Director

DEFENSE NUCLEAR AGENCY

Washington, DC 20305

REPORT DOCUMENTATION PAGE		READ INSTRUCTIONS BEFORE COMPLETING FORM
1. REPORT NUMBER DNA-TR-81-138	2. GOVT ACCESSION NO.	3. RECIPIENT'S CATALOG NUMBER
4. TITLE (and Subtitle) FUEL-AIR EXPLOSIVE NUCLEAR AIRBLAST SIMULATOR: INVESTIGATION OF SECONDARY WAVES		5. TYPE OF REPORT & PERIOD COVERED Technical Report
		6. PERFORMING ORG. REPORT NUMBER SSS-R-82-5331
7. AUTHOR(s) T. H. Pierce M. A. Groethe		8. CONTRACT OR GRANT NUMBER(s) DNA 001-81-C-0191
9. PERFORMING ORGANIZATION NAME AND ADDRESS S-CUBED, A Division of Maxwell Labs, Inc. P.O. Box 1620 La Jolla, California 92038		10. PROGRAM ELEMENT, PROJECT, TASK AREA & WORK UNIT NUMBERS Task Y99QAXSD-00012
11. CONTROLLING OFFICE NAME AND ADDRESS Director Defense Nuclear Agency Washington, DC 20305		12. REPORT DATE 1 April 1982
		13. NUMBER OF PAGES 122
14. MONITORING AGENCY NAME & ADDRESS(if different from Controlling Office)		15. SECURITY CLASS (of this report) UNCLASSIFIED
		15a. DECLASSIFICATION/DOWNGRADING SCHEDULE N/A since UNCLASSIFIED

16. DISTRIBUTION STATEMENT (of this Report)

Approved for public release, distribution unlimited.

17. DISTRIBUTION STATEMENT (of the abstract entered in Block 20, if different from Report)

19. KEY WORDS (Continue on reverse side if necessary and identify by block number)

Fuel-Air Explosive
Airblast Simulators
Shock Waves
High Explosive Tests

20. ABSTRACT (Continue on reverse side if necessary and identify by block number)

The small-scale DNA fuel-air explosives airblast facility (1/4 Γ nuclear
airblast equivalent) was modified to increase pressure and photographic instru-
mentation. Additional preparations were undertaken to enable tests to be
conducted under a variety of conditions thought to be responsible for secondary
shock wave formation. A number of experiments were conducted. These indicated
that: (1) detonation was marginally initiated in the fuel-air clouds; (2) cloud
shape did not greatly influence the airblast except in the immediate vicinity of

DD FORM 1473 EDITION OF 1 NOV 65 IS OBSOLETE

20. ABSTRACT (Continued)

the cloud; (3) transverse moving waves were not present external to the cloud boundaries; (4) fuel distribution non-uniformities within the cloud appear to produce local secondary explosions.

TABLE OF CONVERSION FACTORS TO SI UNITS

To Convert From	To	Multiply By
angstrom	meters (m)	1.000 000 x E −10
atmosphere (normal)	kilo pascal (kPa)	1.013 25 x E +2
bar	kilo pascal (kPa)	1.000 000 x E +2
barn	meter^2 (m^2)	1.000 000 x E −28
British thermal unit (thermochemical)	joule (J)	1.054 350 x E +3
cal (thermochemical)/cm^2	mega joule/m^2 (MJ/m^2)	4.184 000 x E −2
calorie (thermochemical)	joule (J)	4.184 000
calorie (thermochemical)/g	joule per kilogram (J/kg)	4.184 000 x E +3
degree Celsius	degree kelvin (K)	$T_K = t^\circ_C + 273.15$
degree (angle)	radian (rad)	1.745 329 x E −2
degree Fahrenheit	degree kelvin (K)	$T_K = (t^\circ_F + 459.67/1.8)$
electron volt	joule (J)	1.602 19 x E −19
erg	joule (J)	1.000 000 x E −7
erg/second	watt (W)	1.000 000 x E −7
foot	meter (m)	3.048 000 x E −1
foot-pound-force	joule (J)	1.355 818
gallon (U.S. liquid)	meter^3 (m^3)	3.785 412 x E −3
inch	meter (m)	2.54 000 x E −2
kilotons	terajoules	4.183
kip (1000 lbf)	newton (N)	4.448 222 x E +3
kip/inch^2(ksi)	kilo pascal (kPa)	6.894 757 x E +3
ktap	newton−second/m^2 (N−s/m^2)	1.000 000 x E +2
micron	meter (m)	1.000 000 x E −6
mil	meter (m)	2.540 000 x E −5
mile (international)	meter (m)	1.609 344 x E +3
ounce	kilogram (kg)	2.834 952 x E −2
pound-force (lbf avoirdupois)	newton (N)	4.448 222

TABLE OF CONVERSION FACTORS TO SI UNITS
(continued)

To Convert From	To	Multiply By
pound-force inch	newton-meter (N·m)	$1.129\ 848 \times E\ -1$
pound-force/inch	newton/meter (N/m)	$1.751\ 268 \times E\ +2$
pound-force/foot^2	kilo pascal (kPa)	$4.788\ 026 \times E\ -2$
pound-force/inch^2(psi)	kilo pascal (kPa)	$6.894\ 757$
pound-mass (1bm avoirdupois)	kilogram (kg)	$4.535\ 924 \times E\ -1$
pound-mass-foot^2 (moment of inertia)	kilogram-meter^2 (kg·m^2)	$4.214\ 011 \times E\ -2$
pound-mass/foot^3	kilogram-meter^3 (kg/m^3)	$1.601\ 846 \times E\ +1$
shake	second (s)	$1.000\ 000 \times E\ -8$
slug	kilogram (kg)	$1.459\ 390 \times E\ +1$
torr (mm Hg, 0°C)	kilo pascal (kPa)	$1.333\ 22 \times E\ -1$

TABLE OF CONTENTS

LIST OF ILLUSTRATIONS

4

LIST OF ILLUSTRATIONS (Continued)

5

LIST OF ILLUSTRATIONS (Continued)

LIST OF ILLUSTRATIONS (Concluded)

LIST OF TABLES

1. INTRODUCTION

Over the past several years, S-Cubed has carried out various investigations relating to the development of a reusable fuel-air explosive (FAE) nuclear airblast simulator (References 1-3). The objective was to develop the technology for free field (full 2π steradian) simulation at the 1 kiloton nuclear equivalent level. A permanently installed FAE simulator of this scale could potentially supplement or replace conventional high-explosive stacks as an air-blast source for military testing. Due to the low near-field pressures that would be generated by the FAE, site rehabilitation between tests would be minimal, reducing both test turnaround time and cost. In addition, an FAE airblast source would not produce significant amounts of debris, ejecta, or ground shock.

As a part of the investigations, a small-scale prototype FAE airblast simulator was built. Airblasts equivalent to a 1/4-ton nuclear burst were produced by detonating nominally hemispherical, 4.58 m (15 ft) radius dispersions (clouds) of liquid fuels in air. These unconfined dispersions were formed in approximately 1/2 second by impulsively injecting the fuel into the atmosphere. The fuel was forced through a cluster of 600 and 1400 radially-directed hydraulic nozzles located at the ground surface. A small quantity of high explosive (< 0.5 kg), positioned near the nozzle cluster was then exploded to detonate the cloud. The fuel used most frequently with the simulator was propylene oxide.

The quality of the airblasts produced by this prototype simulator was variable. In some tests, blastwaves with well-behaved Friedlander type overpressure waveforms were generated. In other tests, however, the waveforms contained superimposed pressure excursions with incremental amplitudes comparable to that of the lead shock. These excursions were considered to be a serious simulation flaw in those cases for which the associated incremental impulse contributed significantly to total positive phase impulse.

9

Some initially postulated causes for the secondary waves were discussed in Reference 3. The possible causes that were considered are: asymmetric initiator (high explosive) position; nonuniform or asymmetric fuel distribution; excessive or insufficient initiator strength, an extensive fuel-air detonation reaction zone (due to large fuel spray droplets); and an additional energy release by the cloud (due to a sudden chemical equilibrium shift).

In order to attempt experimentally to discriminate between these several possibilities, it was clear that, as a minimal step, the spatial resolution of pressure diagnostics would have to be unusually fine. Prior to the presently reported effort, static pressure transducer spacings varied from 3-6 m (9.8-19.6 ft). For detailed blastwave structure experiments, however, it was felt that the transducers should be no more than about 0.5 m (1.6 ft) apart. This spacing would represent about 5 percent of the maximum radius to which secondary waves were observed in blastwaves from the 1/4-ton simulator. In addition, it was felt that much more photographic instrumentation than the single high-speed camera used previously would be necessary in order to try to trace the origins of secondary waves.

Accordingly, under the presently reported contract, extensive facility revisions were undertaken in order to accommodate extensive pressure and photographic diagnostics. A matrix of experiments to investigate the origins of secondary waves was devised. After a series of initial equipment check-out tests, a number of the test-matrix experiments were conducted. Although the cause of secondary waves was not isolated in these limited tests, the experiments represented a first step in the search.

2. FACILITY MODIFICATIONS

The objective of the FAE facility modifications that were undertaken as part of this contract was to improve photographic and pressure measurement resolution, emphasizing coverage in the immediate vicinity of the fuel-air cloud. A major alteration of the test pad was accomplished, the accommodations for photographic coverage were expanded, and pressure diagnostics were greatly increased and improved.

2.1 Test Pad

The FAE test pad consists of a 9.2 m (30 ft) diameter, concrete-paved area over which fuel-air clouds are formed and detonated. The fuel dispenser is located in the center of this area, below the ground surface. Concrete instrumentation runways, 1.8 m (6 ft) wide, extend from this central area. The runways contain recesses covered with steel plates, on which transducers are mounted. Signal wires are routed from these troughs through underground conduit to the control bunker.

When this test pad was originally built, two perpendicular runways, designated 0° and 90°, were included. The 0° leg is 14 m (46 ft) long and the 90° leg is 30 m (98 ft) long. On both of these legs, fixed-position instrumentation troughs were located at 3, 6, 10, and 14 m (9.83, 19.7, 32.8, and 45.9 ft) from the fuel dispenser. The 90° leg also has troughs at 19, 24, and 30 m (62.3, 78.7, and 98.4 ft). These spacings were selected in order to compare FAE overpressure waveforms with those from nuclear airblasts in the 7-700 kPa (1-100 psi) range.

In order to increase the number of transducers that could be mounted along an instrumentation leg, either a new leg would have to be built or one of the existing legs modified. The former option was chosen. The general orientation of the new leg is shown on Figures 1 and 2; Figure 3 is a closeup photograph. The leg is approximately 12.2 m (40 ft) long and is separated by 45° from the

11
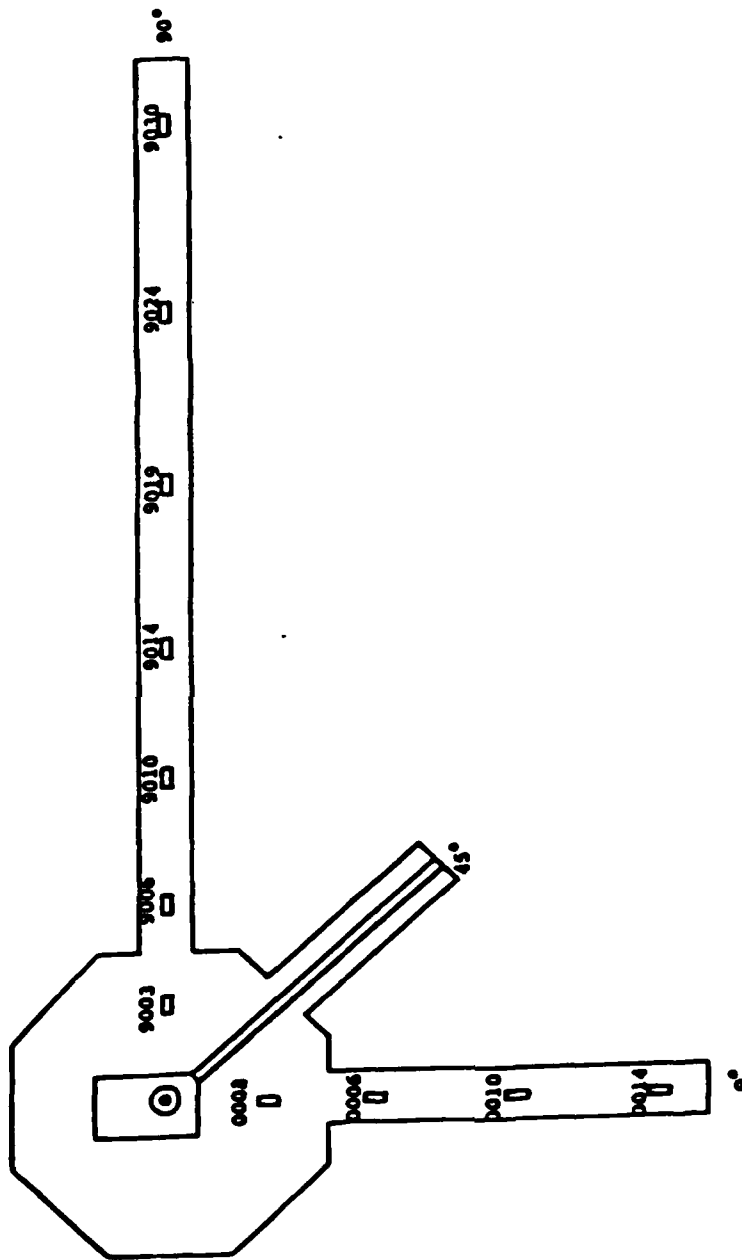
Figure 1. FAE pad layout, showing locations of fixed instrumentation mounting points. The last two digits of each position number represent the nominal distance (in meters) from the dome nozzle head in the pad center.

Figure 2. Overall view of fuel-air explosives test site. Cloud is formed in central area. Static and stagnation pressures are measured along paved instrumentation legs.

13
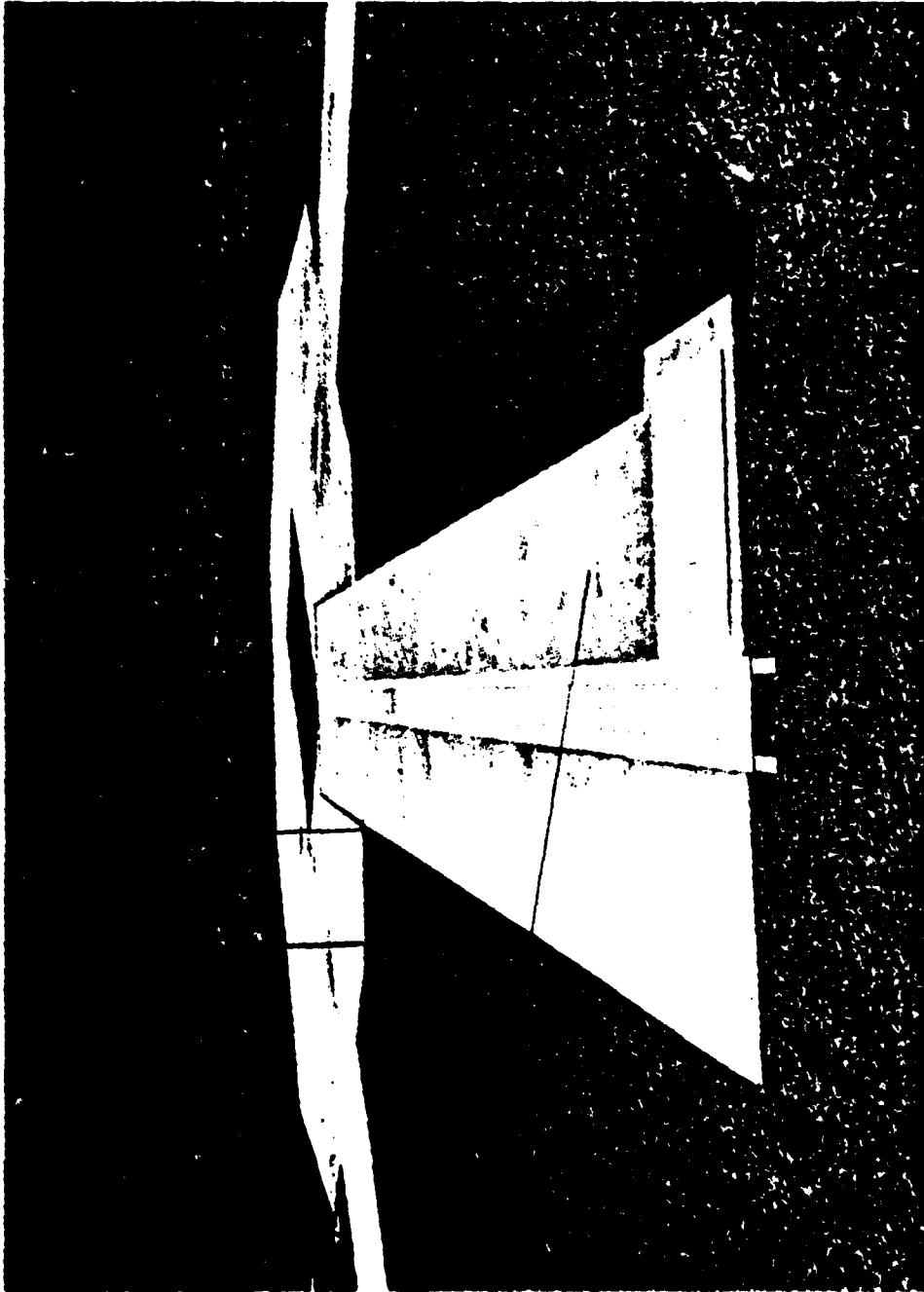
Figure 3. Instrumentation leg with continuous instrumentation trough. Signal wire junction box is located under blast cover adjoining trough in lower part of photograph.

14

older runways. Like the other instrumentation legs, the 45° leg is 1.8 m (6 ft) wide, and was fabricated of concrete that was heavily reinforced with steel. The depth of the concrete is 38 cm (15 in) along the centerline of the leg and about 15 cm (6 in) at the edges. The new (45°) leg was built with a continuous instrumentation trough (rather than fixed-position recesses). The continuous trough has a vertical cross section which is in the shape of a tee. Steel angle iron was imbedded in the concrete to protect the sharp-cornered shoulders that are exposed on the upper surface.

A photograph of a 55 cm (22 in) section of the instrumentation trough is shown on Figure 4. Transducers are mounted on 15.2 x 15.2 x 6.4 cm (6 x 6 x 2.5 in) steel blocks which are supported on the shoulder of the tee. The blocks are secured with recessed allen head cap screws to prevent them from being dislodged during the negative phase of the airblast.

The size of the transducer mounting blocks and the material they are made of were selected so as to be compatible with the existing in situ pulse pressure calibrator. The principal feature of this calibrator (Reference 3) is that a magnetic hold-down is used to engage an O-ring seal around the transducer being tested (which is installed on the mounting block). For this reason, the mounting blocks had to be ferrous and large enough as to accommodate the magnet head. Without these requirements, lead-brick mounting blocks would have been chosen for their high-density and superior ability to damp mechanical vibrations. The performance of the steel mounting blocks used in the new instrumentation leg is discussed in Appendix A. Blank mounting blocks are installed as spacers between those used with transducers so that the entire trough is covered during a test.

Signal wires from individual transducers are routed through the lower part of the continuous trough. The wires pass through a feed-through where they connect to a 24-connector junction box (Figure 5). The junction box is in a concrete lined recess adjacent to the trough. This recess is protected by a steel blast cover
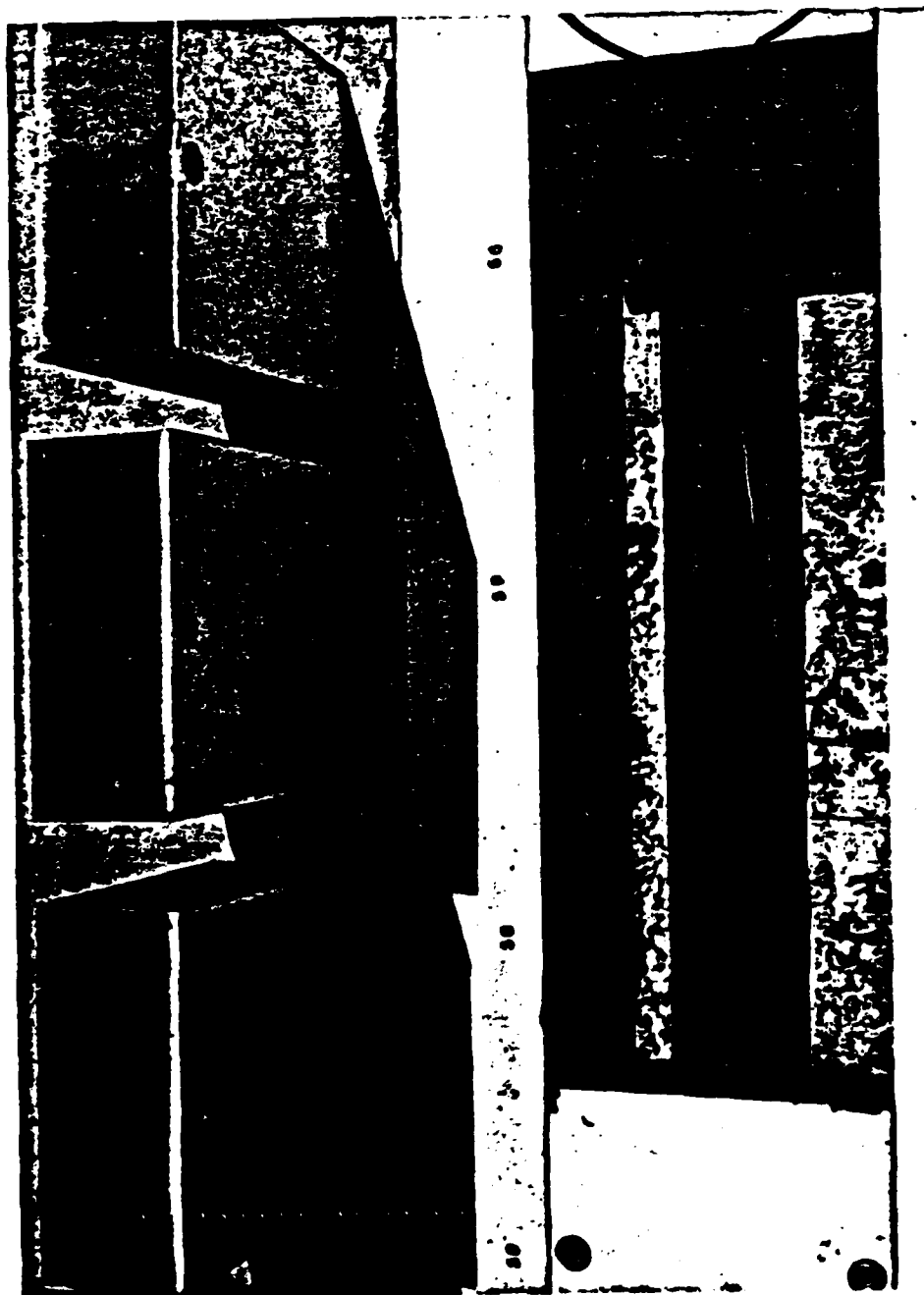
Figure 4. Closeup photograph of continuous trough with transducer mounting blocks removed, showing cable runway and mounting block supports. The mounting blocks are steel plates, 15.2 x 15.2 x 6.4 cm.

16
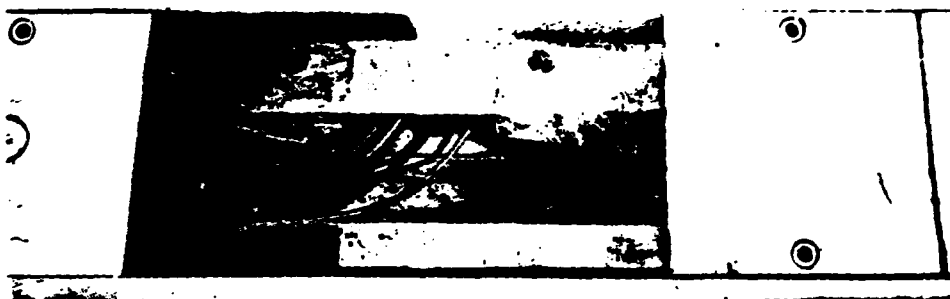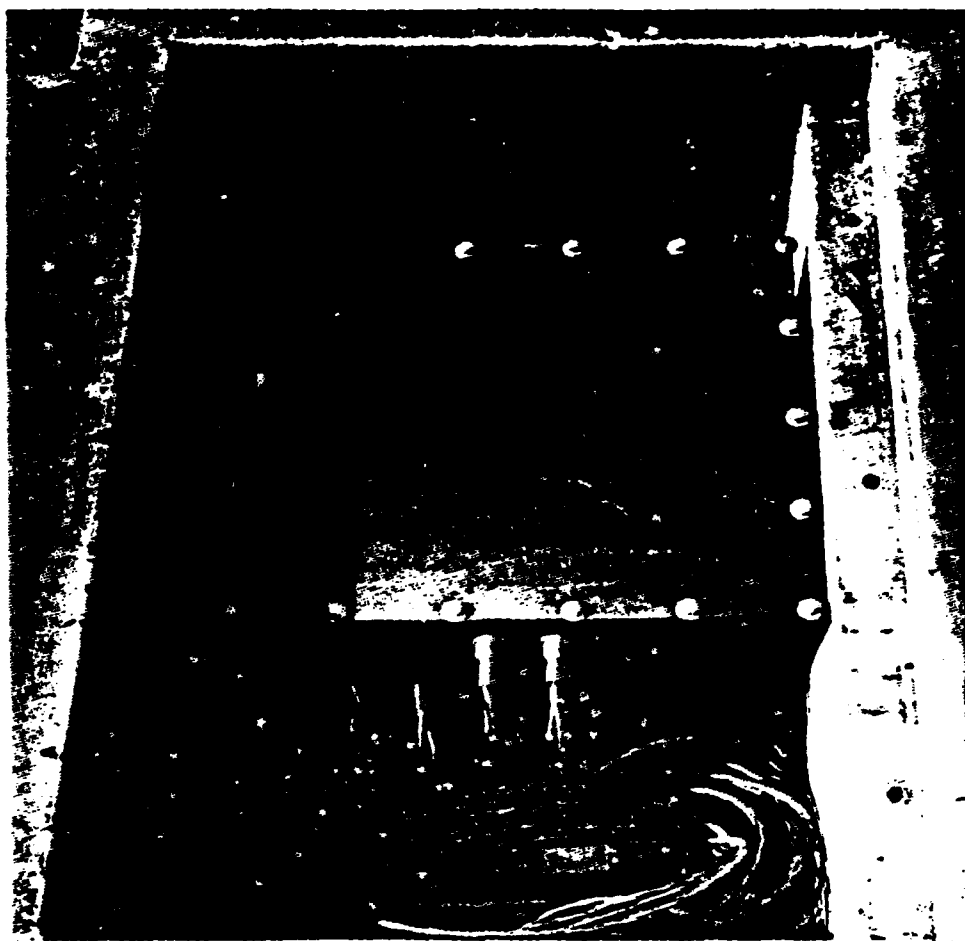
Figure 5. Signal-wire junction box serving continuous instru-
           mentation trough. Junction box is protected by
           steel blast covers (Figure 3) during use.

17

during use. An inside view of the junction box appears on Figure 6. Two 27-pair cables extend from this junction box through 5.1 cm (2 in) steel conduit to the control bunker where they are terminated in a second junction box. This particular wiring arrangement provided reusable-service capability for up to 24 four-wire transducers, with three four-wire lines as spares.

2.2 Photographic

Provisions for photographic coverage were expanded under this contract by adding a large reusable refraction screen and two camera shelters. The camera shelters were placed in surveyed positions 92 m (300 ft) from the center of the test pad. One of the shelters, designated "north camera position" (NCP), has a line of sight that is perpendicular to and passes through the midpoint of the 45° instrumentation leg. This was the principal photographic station. The steel reinforced wooden shelter is shown on Figure 7. The top row of windows is at a vertical height above the test pad of approximately 2 m (6.5 ft). This is approximately at the vertical midpoint of a field of view that would just include the vertical height of the fuel/air clouds.

The secondary photographic equipment shelter, designated the "south camera position" (SCP), is perpendicular to the 0° instrumentation leg along a line of sight passing through its midpoint. Construction of this shelter is similar to the north camera position. The windows are about 5 m (16 ft) above the plane of the pad so that films taken at this position look down on the fuel-air clouds slightly.

Both camera shelters contain two levels of sturdy shelving on which cameras can be mounted. In addition, both shelters were hard wired for A.C. power, as well as with signal wires for triggering equipment.

The refraction screen was installed so as to be facing the north camera position. Its size is sufficient to nearly fill the entire 9.2 x 12.2 m (30 x 40 ft) field of view consisting of the

18
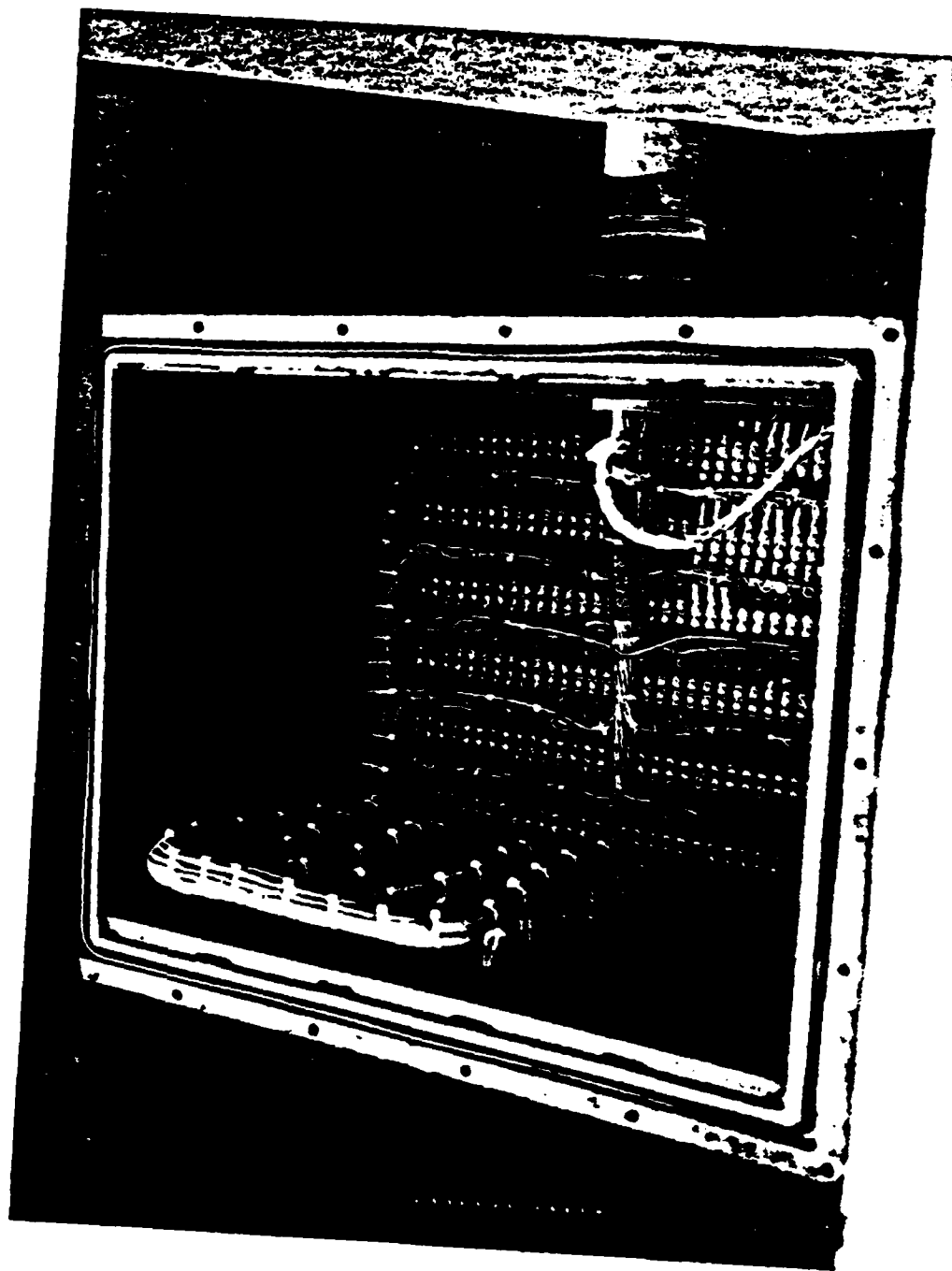
Figure 6. Closeup photograph showing wiring inside junction box. The box is made of steel and is watertight. Signal wires are routed through steel conduit to control bunker.

19
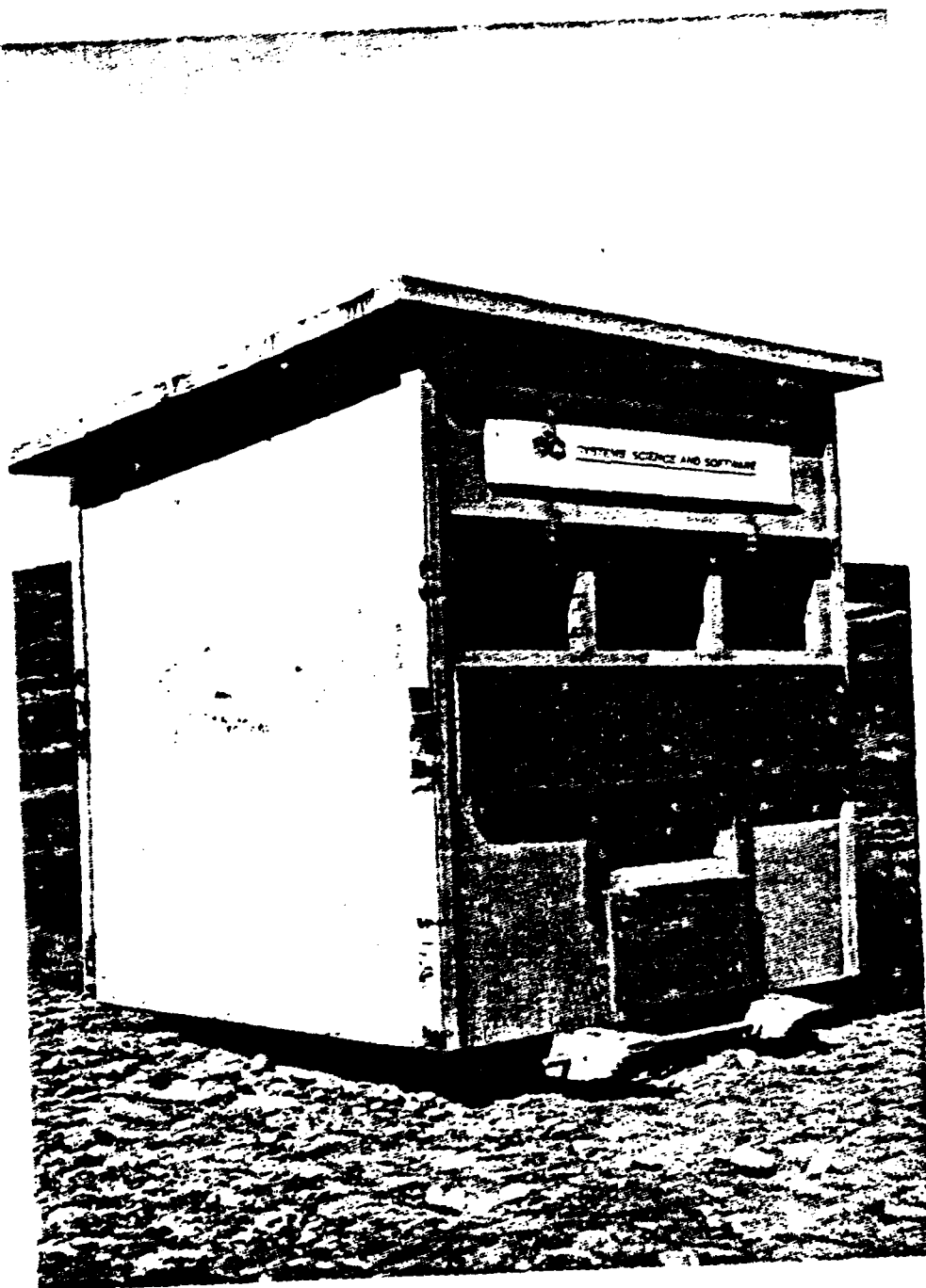
Figure 7. Field shelter used to house high-speed cameras and other photographic equipment. The two shelters are hard-wired for A.C. power and with signal wires for starting equipment.

20

quarter-plane defined by a vertical line through the center of the test pad and the 45° leg. A motion picture frame (taken from test CD15, discussed later) which shows this field of view with the refraction screen in place is given on Figure 8.

The refraction screen is a large tarpaulin made of 10 oz. vinyl/polyester fabric reinforced with a mesh of polyester thread. The tarpaulin was manufactured by chain stitching alternate black and white strips of material. The tarpaulin edges were hemmed and 1/2-inch brass grommets inserted on 1.5 m (5 ft) spacings. This is an extremely durable construction which is similar to that used in the manufacture of athletic field covers.

The tarpaulin was securely staked to a hillside that rises abruptly beginning approximately 20 m (65 ft) behind the 45° leg, with respect to the north camera position (NCP) line of sight. The hill is not perpendicular to this line of sight, nor is its slope constant over the region covered by the tarpaulin. For this reason, the shape of the tarpaulin when laid out on a flat surface is a large, irregular, four-sided figure which covers an area of about 800 m² (8600 ft²).

The glossy surface of the screen made mandatory the use of a polarizing filter when filming in the morning. Later in the day, the sun's angle changed with respect to the hillside such that reflections were not a problem. Excellent contrast could then be obtained without the polarizing filter. The screen proved to be very durable and survived many tests.

2.3 Dispenser

The fuel dispenser in use during previous testing was improved by adding switches that would accurately indicate the actual onset and end of dispensing. These switches were intended to be used in some of the planned tests in order to accurately set the cloud formation time (total time between the start of dispensing and cloud detonation) and to enable a measurement of the cloud dwell time (time between end of dispensing and cloud detonation). Pressure
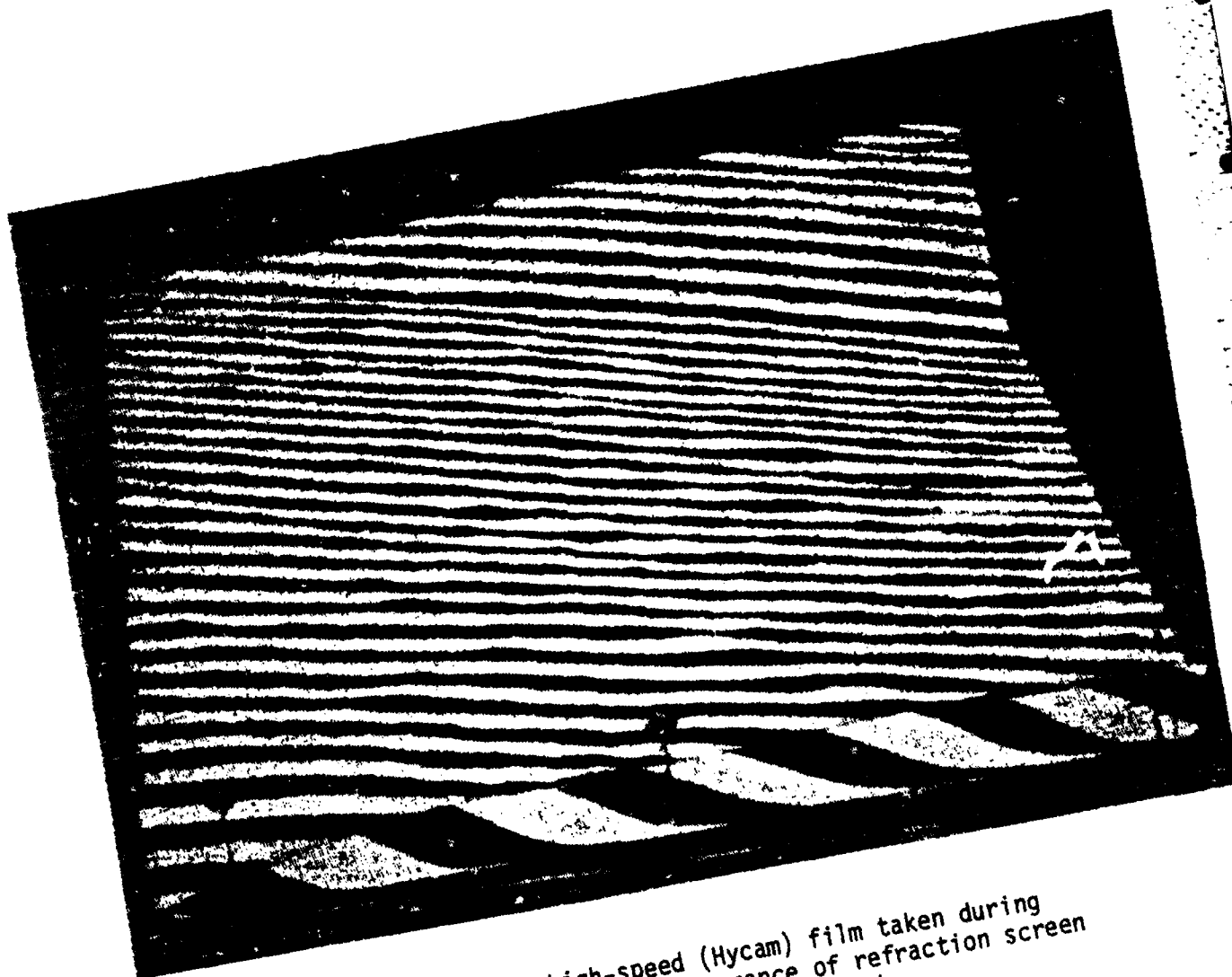
Figure 8.   Frame from high-speed (Hycam) film taken during test CDI5A showing appearance of refraction screen mounted on hillside behind test pad.

transducers were tested for these applications, but the details of the pressure rise at the onset of dispensing and the pressure drop-off at the end of dispensing were found to be complex and variable (Figure 9). An accurate and reliable triggering circuit based on the dispenser pressure history would have been commensurately complex. Instead, it was decided to use simple contact switches.

One of the two switches consists of a pair of foil leaves, each of which is approximately 0.64 x 2.5 cm (0.25 x 1 in). The leaves are initially separated by about a 2 mm gap. This switch is placed outside the dispenser dome nozzle head so as to block one of the 60 horizontal-facing nozzle holes. When fuel dispensing begins, the force of the liquid jet emerging from the nozzle closes the switch. This closure triggers a simple electronic circuit which in turn generates an output pulse. The foil switch is not physically shielded and is destroyed during a cloud detonation test. However, its simplicity is such that many such "start dispense" switches can be easily prepared in a few hours time.

The end-of-dispense switch is also very straightforward. It simply consists of a steel spring that is mounted in a hole within an externally-threaded Teflon body. This switch is installed in the dispenser in such a way that the spring protrudes by about 3 mm from the shoulder against which the dispenser piston seats at the end of its travel. When the aluminum piston reaches this shoulder, it acts as a bridge to complete a circuit between the spring and the steel shoulder. This closure is used as a short-to-ground triggering event. The end-dispense switch was designed to fit into a blast protected recess machined into the top cover of the dispenser, and so it was not necessary to replace the switch between tests.

Figures 9 to 11 illustrate the general features of the dispensing pressure variations with time, and also the operation of the two indicator switches. The cylinder stagnation pressure in Figure 9 was measured with a transducer placed in the end-dispense switch location. As the piston nears the shoulder, the pressure rises significantly above the true stagnation pressure. This is due

23
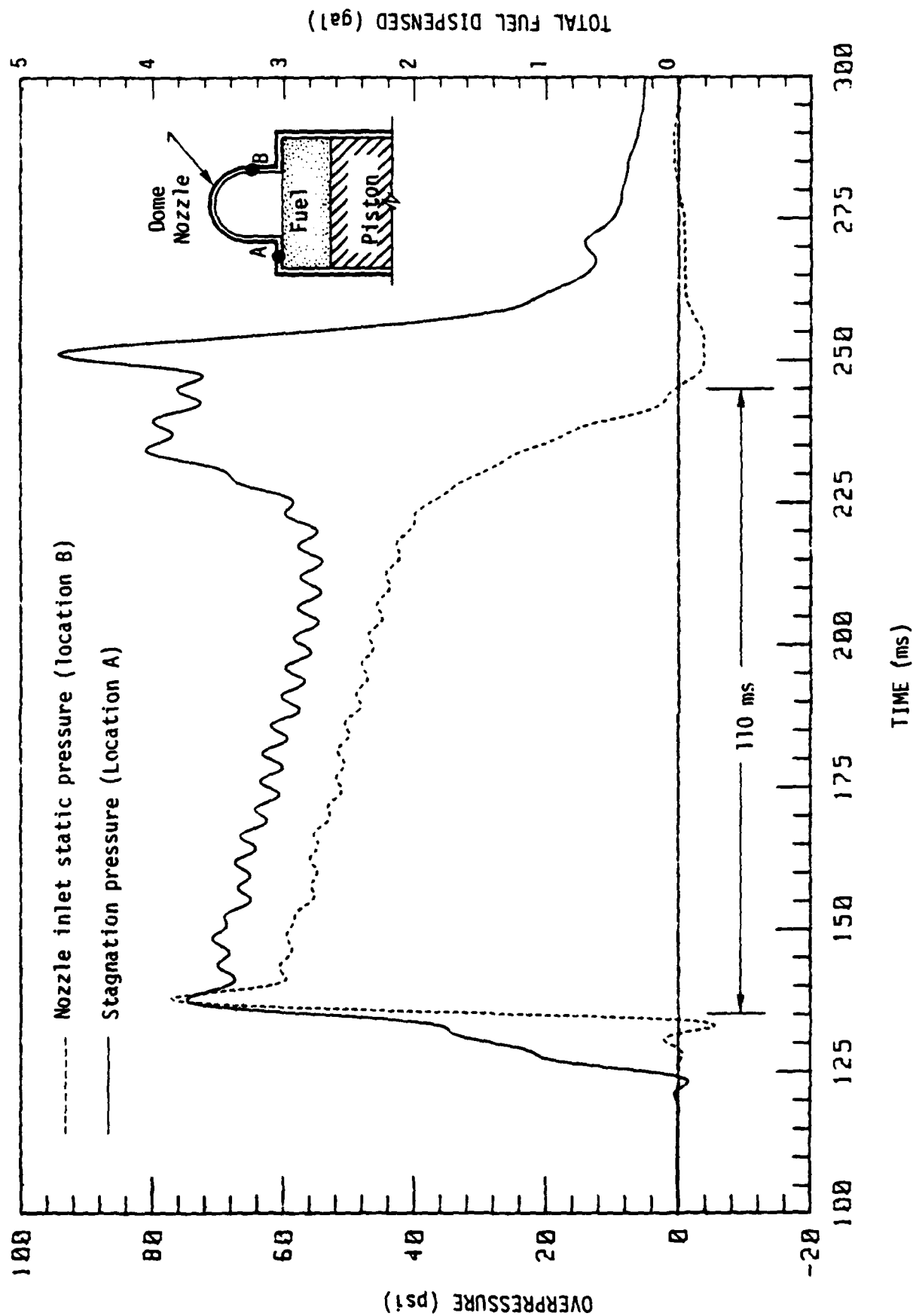
Figure 9. Pressure records taken during operation of impulsive liquid fuel dispenser, Test CF22; 2.91 gal. propylene oxide.

24
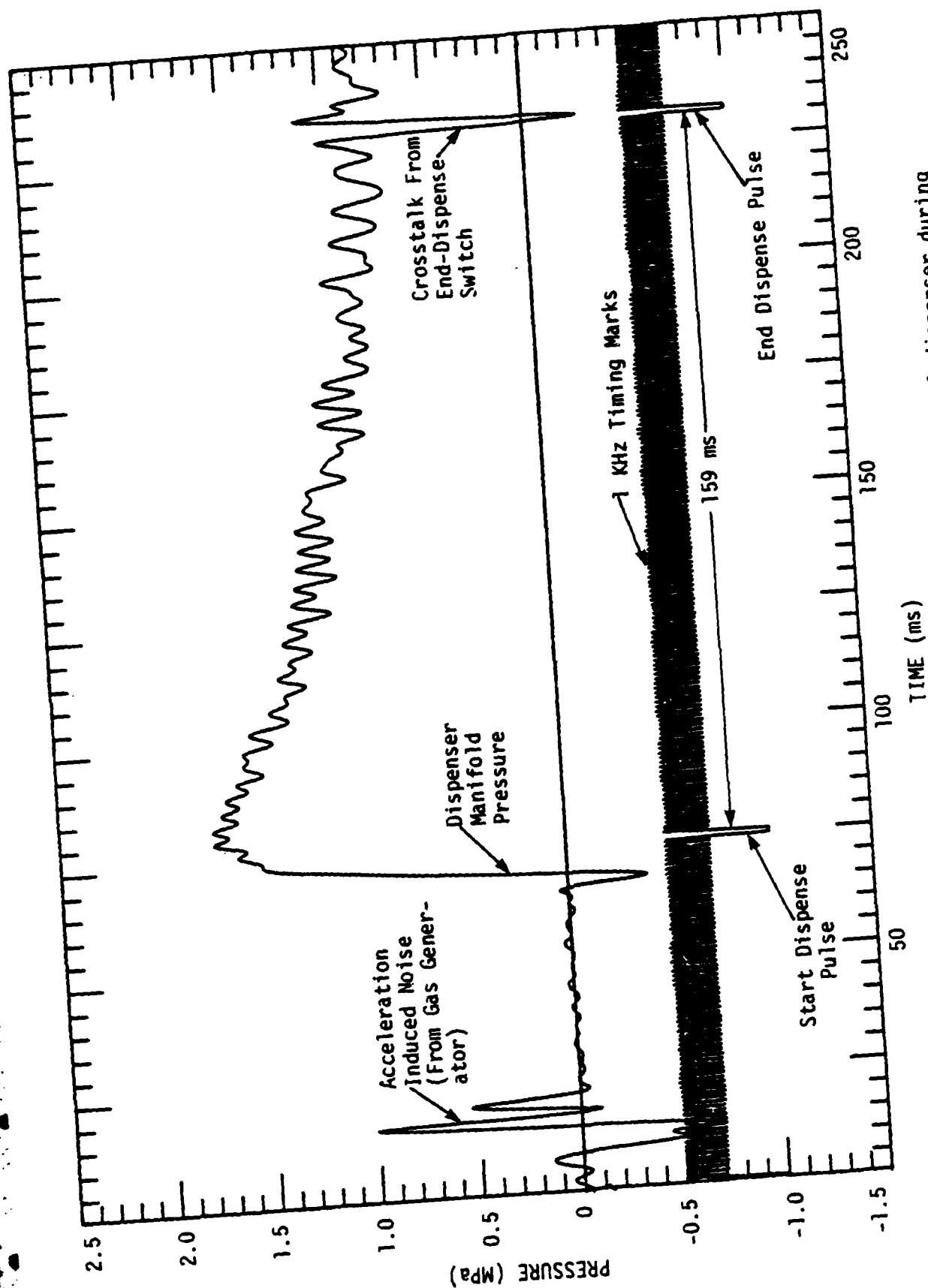
Figure 10. Freevolume pressure (pressure behind piston) in fuel dispenser during
FAE Test CD15A, with reference timing mark record and superimposed output
pulses from dispenser start/stop indicators.

25
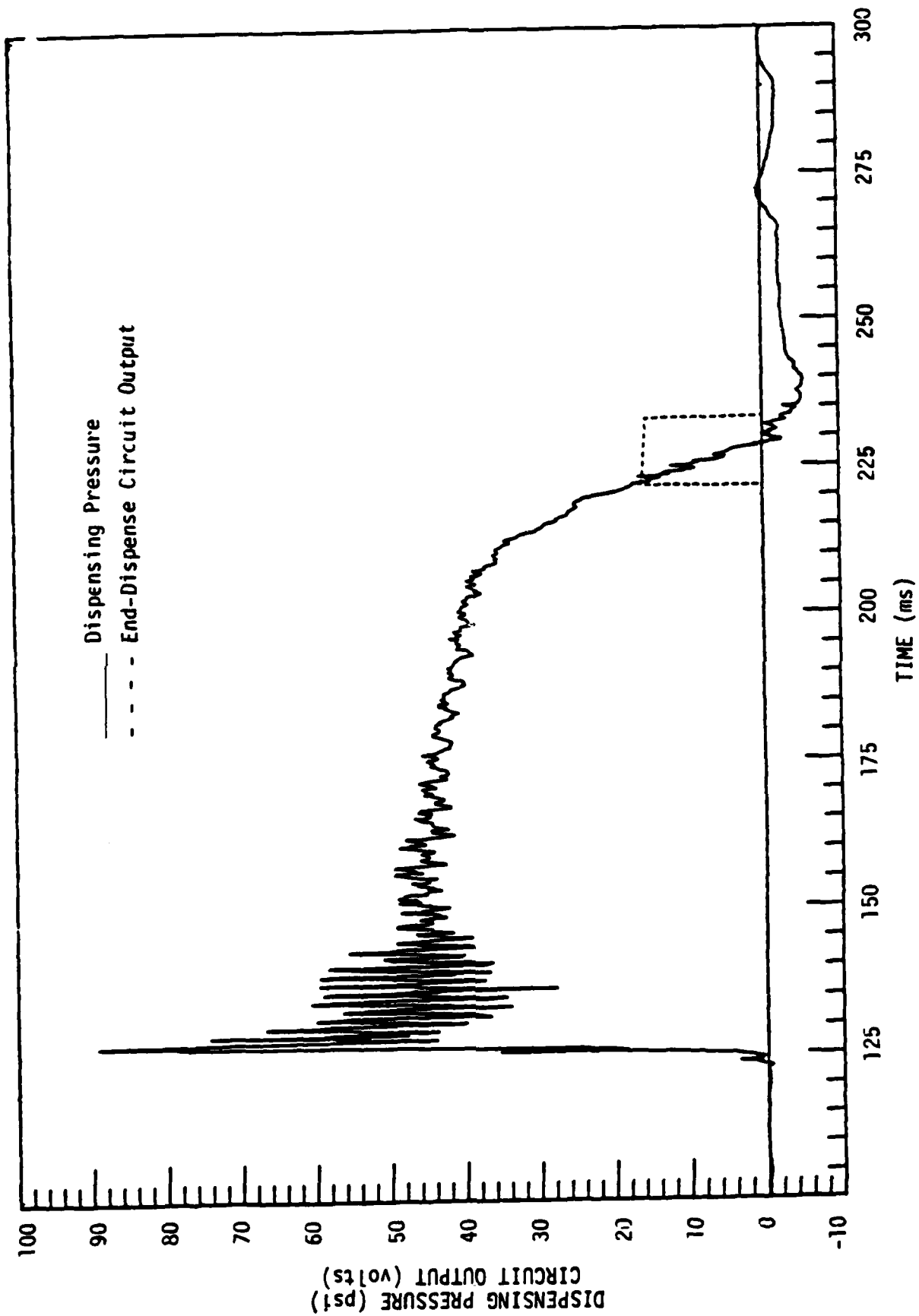
Figure 11. Dispensing pressure during cloud formation Test CF23. Transducer location corresponds to position "B" on Figure 9. End-dispense indicator output is superimposed.

26

to the geometry of the top part of the piston, which was designed to throttle the flow that is forced out of the region between the piston and shoulder. The resulting rise in pressure reduces the piston velocity before it impacts the shoulder, preventing damage to both parts. The static pressure was measured just ahead of the dome nozzle on the constant-area part of the inlet (see Figure 9). As can be seen, the stagnation pressure rises about 10 ms prior to the static pressure rise. This is the time required to hydraulically fill the dome nozzle head. Because of its hemispherical shape, the nozzle head cannot be completely filled before a test to a level above the lowermost row of drilled nozzle holes.

Figure 10 is a sample showing the pressure variation on the back side (gas generator side) of the piston, which is the pressure normally measured during an experiment. The start and end dispense switch pulses are superimposed on this figure. The start dispense switch is engaged at very nearly the same moment that the manifold pressure reaches its peak value. On Figure 11, the end-dispense switch pulse is superimposed on the static pressure profile from a dispenser test. On this test, piston contact with the end-dispense switch occurred 7 ms before the flow static overpressure reached zero (which was assumed to correspond to actual stoppage of fluid flow from the dispenser). Therefore, some fuel was dispensed beyond this time. However, an approximate calculation using the measured pressures indicated that less than 2.5 percent of the total quantity of fuel was dispensed in the last 7 ms on this test, and this accuracy was considered satisfactory.

2.4   Pressure Instrumentation

Additional pressure transducers were obtained to augment diagnostics near and under the fuel-air cloud. This is a region in which ground motions from the FAE, while not severe, are of such magnitude that transducers with acceleration sensitivities much above about 15 Pa/g (0.002 psi/g) will exhibit significant pre-shock response. Accordingly, an initially high priority specification for selection of the new transducers was acceleration sensitivity.

27

A set of 37 pressure transducers was received as GFE through DNA. Ten of these were Kulite Model HKS-11-375 and the remainder Kulite Model XTS-190. Both models are fast response strain gage transducers. The XTS models were supplied in various ranges from 0.07-7 MPa (10-1000 psi). All of the HKS models were 14 MPa (2000 psi) range transducers.

Each of the Kulite transducers was carefully tested in an S-CUBED, uncalibrated shock tube and compared in performance with PCB type 102M58 transducers. Each transducer was also tested for acceleration response using a drop-bar facility. Thermal response of selected samples was also tested using radiative heating from a photographic flashlamp. The drop-bar and radiative heating procedures used for these tests are described in Reference 3.

Figure 12 is an illustrative sample showing the shock tube response of one of the Kulite transducers. A 217 KHz ringing was excited in the HKS sample shown. The average amplitude of the ringing was about ± 6 percent of the mean pressure level except during the first 63 µs where it was considerably greater.

As a group, the Kulite XTS transducers exhibited relatively longer shock tube rise time, but there was no high-amplitude ringing at the leading edge. A sample shock tube response is shown on Figure 13. The rise time was 34 µs in this case.

An example of the acceleration response of these Kulite transducers is given on Figure 14. The peak acceleration induced by the drop bar was about 980 m/s^2 (100 g). All of the transducers responded in a qualitatively similar fashion to this particular acceleration pulse, but the amplitude of the responses differed widely between samples.

Figure 15 is a worst-case example of Kulite XTS thermal response, with a peak thermally-induced excursion equivalent to 116 percent of the full scale transducer output. The thermal performance of the Kulite HKS model was far superior. Here it is noted that thermal protection is routinely applied to PCB transducers when
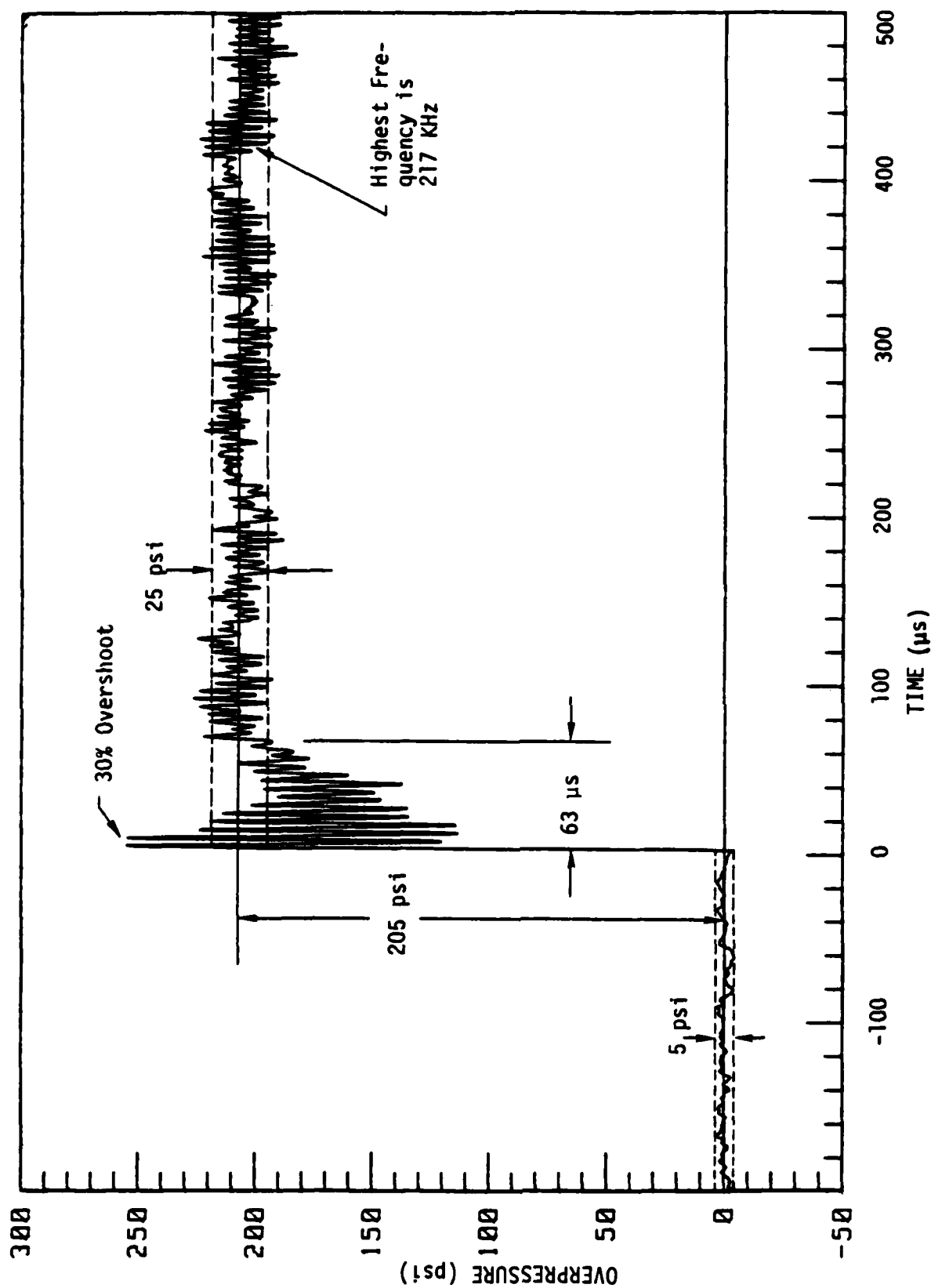
Figure 12. Shock tube response of Kulite HKS transducer, SN 5-9X.

29
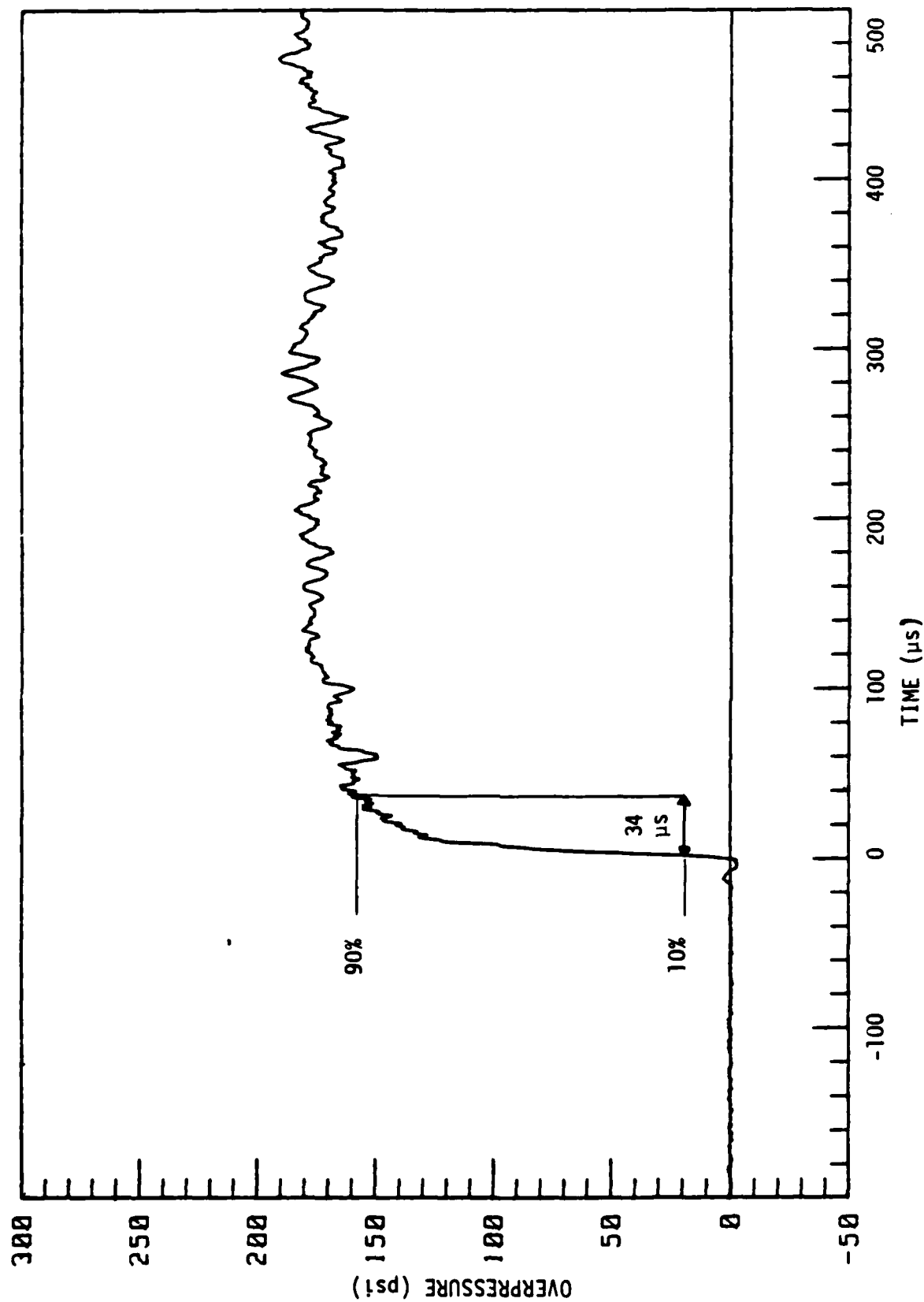
Figure 13. Shock tube response of Kulite XTS transducer, SN A-30.

30
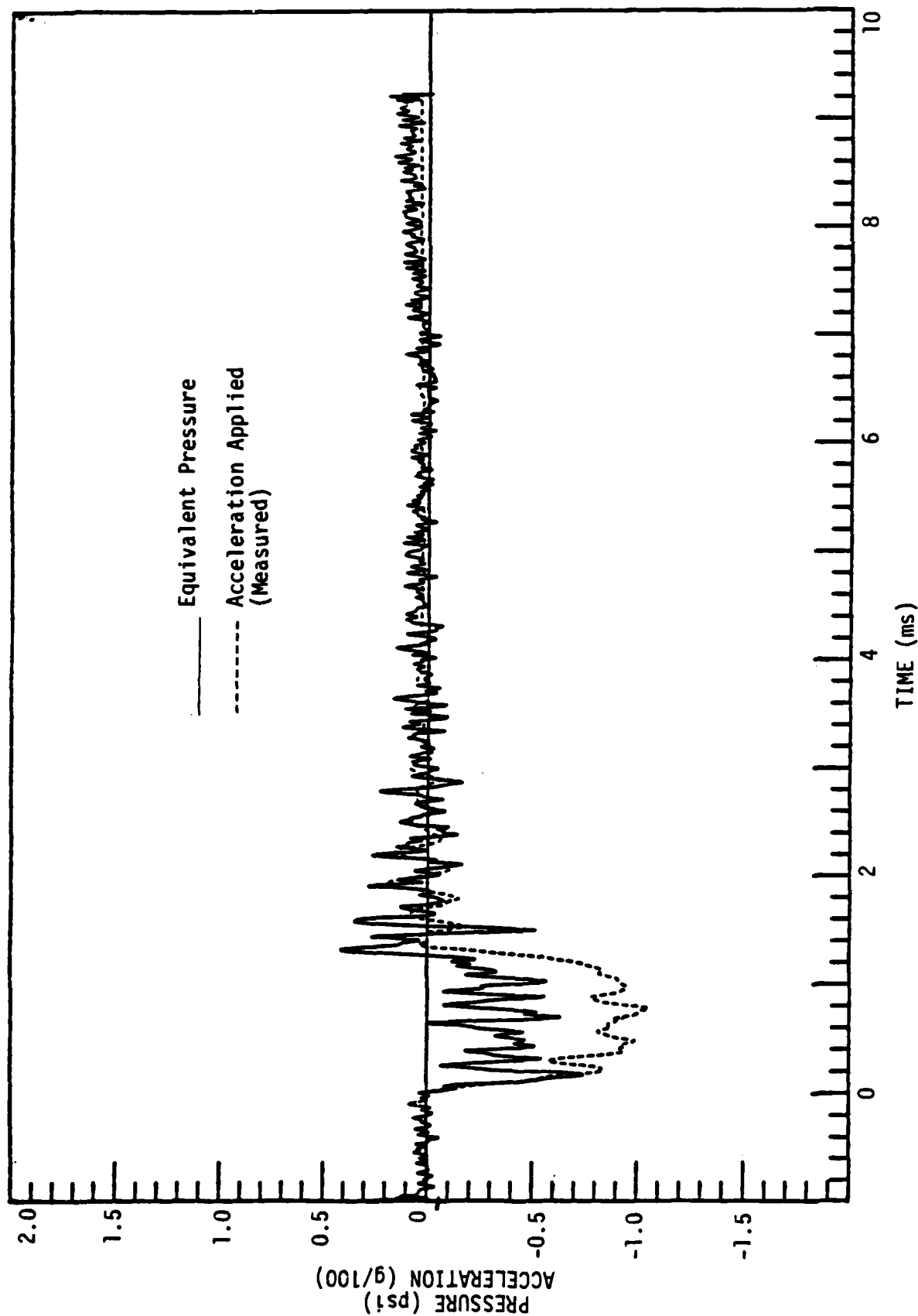
Figure 14. Acceleration sensitivity test of Kulite HKS transducer, SN 3-16. Transducer output is expressed as an equivalent pressure. Output from accelerometer on transducer mounting is superimposed.

31
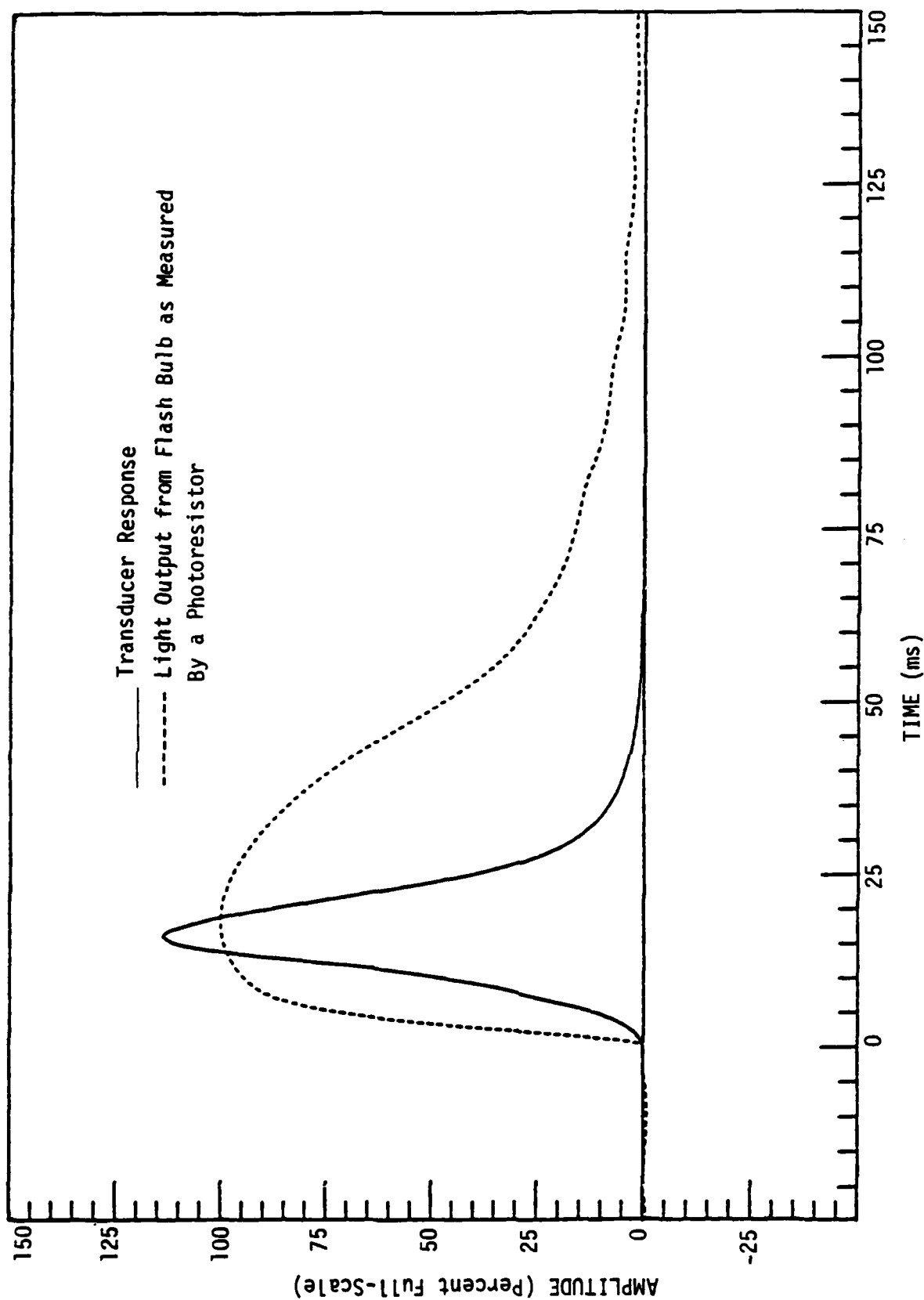
Figure 15. Response of Kulite XTS transducer, SN Z1-37, to thermal radiation.

32

used on FAE tests. The Kulite HKS models were supplied with a previously applied RTV ablative coating. The Kulite XTS models could not be protected in either of these ways by virtue of their design, which incorporates a protective screen over the sensing element.

Table 1 summarizes the characteristic performance of the PCB and Kulite transducers. None of these three transducers is superior to both others in all performance aspects. The Kulite XTS transducers were initially rejected for FAE experiment service due to the unsatisfactory thermal response of the sample tested. However, the average acceleration sensitivity of the Kulite XTS is far superior to both the HKS and PCB, and the XTS also had no measurable overshoot in shock tube tests (Figure 13). The acceleration sensitivity of the HKS was disappointingly higher than had been expected based on the manufacturer's published specifications. It was thought, however, that the special RTV coating on this particular set of transducers may have compromised their acceleration sensitivity.

Of the Kulite transducers received, only the HKS model units were used in the FAE tests initially. However, when two of these transducers failed in service, it was expedient to substitute XTS replacements. The service performance of the XTS was unexpected; the adverse thermal response was not manifest in use. It is presently thought that the effective capture angle of the XTS transducers with respect to non-axial thermal radiation is very small due to the length and location of the holes in the perforated cover (protective screen).

33

TABLE I

COMPARATIVE SUMMARY OF PRESSURE TRANSDUCER PERFORMANCE

Parameter	PCB	Kulite HKS	Kulite XTS
Shock Rise Time (μs)	1	1	30
Shock Response Overshoot (Percent Full-scale)	<5	20	0
Shock-Excited Ringing (Peak-Peak, Percent Ave. Level)	0	50	10
Acceleration Sensitivity (psi/g)	0.002-0.01 (0.004 ave.)	<0.001-0.01 (0.004 ave.)	0.0003-0.01 (0.0005 ave.)
Thermal Response (Percent max output)	10. (unprotected) 0.5 (protected)	1.0 (protected)	110. (Unprotected)

34

3. EXPERIMENTAL TEST PLANS

A planning meeting was held at S-Cubed on 17 June 1981 to discuss experiments which could be used to investigate the origins of secondary waves in fuel-air explosions. In addition to S-Cubed personnel, representatives from Ballistic Research Laboratory, Defense Nuclear Agency, Denver Research Institute, Electromagnetic Systems, and H-Tech Labs were present.

Only experiments which would make use of the existing cloud formation technique (impulsive fuel dispenser) were considered. The list of potential experiments which appears on Table 2 was accordingly compiled and discussed at this meeting. Each of the effects listed had been suggested as a possible source of secondary waves. Most of these effects are discussed in Reference 3. Some additional comments are given here for completeness.

a. Initiator Symmetry

The high explosive used as an initiator in the FAE tests was C-4. The C-4 was formed by hand or in spherical molds, depending on the charge size (i.e., the availability of an existing mold). Because the charge must be located inside the cloud it may be subjected to impact by fuel jets emerging from the dispenser nozzles. In recent tests, the charges have therefore been securely supported to hangers, usually by pressing them onto a plastic rod and then applying cloth tape to hold the charges in place. Some distortion of the spherical charge shape is inevitable during this mounting procedure.

There has been some concern as to whether these initiator charges detonate uniformly and cleanly, due to asymmetries introduced by composition, density, shape, and manner of support. On many of the films taken during tests conducted prior to this contract, it appeared that

35

TABLE 2

POSSIBLE SOURCES OF SECONDARY WAVES IN FUEL-AIR EXPLOSIONS
AND POSSIBLE EXPERIMENTS

Effect	Experiment	Qualifications
Initiator symmetry	Attempt to fabricate HE sphere to improve sphericity of initiator blastwave	--
Fuel distribution in cloud	Reduce cloud volume (by reducing nozzle diameter); dispense variable quantity of fuel into this volume.	Changing nozzle dia. also affects droplet size, extent of prevaporization, initiation requirements, reaction zone length.
Initiator offset	Vary vertical and horizontal position of initiator.	Single-point initiator cannot be placed at cloud center.
Marginal initiation	Vary initiator size from 50-5000 gm	Maximum feasible initiator source may not be sufficient; large initiators cannot be placed near nozzle head.
Droplet diameter (reaction zone thickness)	Change dispensing pressure between 50 and 350 psi.	Dispensing pressure also affects cloud geometery and size; upper pressure bound is limited.
Fuel density near cloud center	Vary initiation dwell time, including zero and negative dwell.	Changing dwell affects cloud size and shape, extent of prevaporization, initiation requirements.

36

the detonation front near the initiator was not spherically symmetric. This could certainly be due to an asymmetric initiation source. It could also be due to asymmetric fuel density within the fuel-air cloud or asymmetric drop size distribution in the immediate vicinity of the initiator. The occurrence of such asymmetries in the detonation front was not correlated with the appearance of secondary waves, however.

b. Fuel Distribution

From photographic observations, the fuel distribution in fuel-air clouds formed by the existing impulsive liquid fuel dispenser is clearly nonuniform radially and also with respect to elevation angle. There are additional local azimuthal nonuniformities. It was thought that problems due to these nonuniformities might be circumvented by increasing the global fuel density (see discussion in Reference 2).

c. Initiator Offset

In recent prior work, the vertical height of the initiator was varied between approximately 10 and 30 percent of the nominal cloud radius. Even if the initiator were mounted directly on the dispenser nozzle head (dome nozzle cluster), the vertical offset would still be about 3 percent. Not only would such mounting permanently damage the nozzle head, but the initiator charge would then block several of the topmost nozzles. For any given size initiator charge there is a minimum height above the nozzle head corresponding to which no more than one of the radially-directed nozzles will be blocked. The topmost nozzle is always blocked. More blockage than this can degrade the fuel-air cloud shape. In addition, the initiator might possibly be dislodged by a number of high velocity jets impinging on it at close range.

37

Horizontal initiator offset can only be controlled
by carefully conducting tests in near-windless condi-
tions. This is a test requirement that, for given
climatic conditions, becomes more severe as the physical
scale of the FAE cloud is reduced. With respect to the
nominally 4.5 m (15 ft) radius clouds detonated in these
experiments, a 10 percent horizontal offset asymmetry can
be produced by a 0.75 m/s (1.7 mph) wind, assuming a
typical cloud formation time of 600 ms. Moreover, wind-
induced cloud displacements cannot be expected to affect
all parts of the cloud equally; i.e., the fuel dispensed
first will be displaced first. Smaller droplets (and
fuel vapor) will be displaced more than larger droplets.
In the experiments described later in this report,
extreme care was exercised to ensure that wind would not
contribute to cloud asymmetries.

d.   Marginal Initiator Strength

There is at present no simple way to estimate the
minimum initiator energy for mixed-phase (two-phase)
detonations. There has been some experimental and
theoretical work in this area (e.g., Reference 4) but
many questions remain. It does appear that the physical
details of the blast initiation process depend strongly
on the blast energy level. In the case of spray
detonations, even nonmarginal initiation is apparently
characterized by oscillations in wave front velocity
during the transition from blastwave to detonation.
Moreover, the presence of any fuel vapor dramatically
enhances the initiation process.

The smallest initiator used with repeated success on
FAE experiments during past work (Reference 1) was 25 gm
(0.055 lbm). It is significant, however, that the
vertical offset of the initiators in those tests was on
the order of 25 percent of the cloud radius, and, in

38

addition, the cloud formation times were quite long, on the order of 1.5-2.0 s. This means that the initiator was almost surely immersed in a detonable portion of the cloud and also that there was a considerable amount of fuel which had evaporated prior to initiation (reducing the initiator energy requirement). Smaller charges than 25 gm were not successful as initiators under any conditions. This could in part be due to difficulties in detonating small C-4 charges.

Fewer tests with variable initiator sizes have been conducted with clouds formed in less than 1.05 s. The minimum initiator size for these rapidly formed fuel-air explosives is not known.

The appearance of secondary waves in past work did not correlate with either initiator height or size, and so reliable, large initiators (> 350 gm) were used in the more recent tests (References 2 and 3). There was, however, concern expressed at the planning meeting that the combustion products (fireball) from initiators of this magnitude might produce large, hot pockets within the exploded fuel-air clouds, and that gas dynamic reflections from these pockets could possibly generate some of the undesirable secondary waves. One initial directive resulting from the planning meeting was to reduce all FAE initiator sizes below 350 gm, while hopefully remaining above the minimum mass required for marginal fuel-air cloud initiation.

e.   Droplet Diameter

The size of the fuel droplets in the fuel-air cloud is determined by the diameter of the dispenser nozzles and by the dispensing pressure history. The droplet size distribution in these clouds is not known, but it is

likely that the largest droplets are on the order of the nozzle diameter, and that the smallest sizes extend to perhaps one percent of the maximum size. It is also likely for some fuel vapor to be present in the cloud.

Droplet size affects detonation reaction zone thickness. For example, this thickness can typically encompass three orders of magnitude between that of a pure vapor-phase detonation and that of a stoichiometrically equivalent detonation in a spray of 2 mm dia. droplets. A very thick reaction zone would displace a large mass of the fuel-air mixture from the center of the cloud during the detonation stage and could accordingly preclude the development of a steady Chapman-Jouget detonation in small clouds. This is discussed in Reference 3.

f. Fuel Density Near Cloud Center

This is a special case of nonuniform fuel-air distribution that has been of particular concern. During formation of the fuel-air clouds, fuel is ejected through the radial dispenser nozzles until a fixed supply is exhausted. In all of the FAE tests, this dispensing period was followed by a waiting (dwell) period in which the cloud was allowed to develop its near maximum radius. In addition, during this period, individual fuel jets were allowed time to break up and to spread laterally, so as to overlap and fill in the cloud with fuel. However, during the dwell period, fuel moving away from the cloud center could possibly leave a void region there, unless a sufficient amount of residual spray recirculates in that region.

On consideration of these six effects, it was the collective opinion of the advisory committee that five test series could be contemplated. These are the following:

40

a. Gross Offset Initiation

A single-point H.E. initiator would be placed near the edge of the fuel/air cloud. The changes in shape of the detonation front observed on high speed films as the front passes through the cloud center might then indicate whether the cloud has a fuel-lean core.

b. Central Initiation

Two experiments were suggested. A smaller single-point initiator than that used on recent FAE tests would be tested at minimum vertical offset. Also, a multi-point initiator consisting of a cluster of small H.E. charges mounted around the dispenser nozzle-head base, could be tried. This latter configuration might produce the same effect as initiation originating from the virtual center of the dispenser nozzle cluster.

c. Rich Fuel-Air Ratio

Smaller clouds than previously generated could be produced. Varying amounts of fuel could be injected into these clouds to obtain globally lean, stoichiometric, and fuel-rich clouds. Fuel-rich clouds might obviate the need for uniform fuel distribution.

d. Initiator Position

In addition to the gross-offset experiment (a), the vertical and horizontal position of the initiator could be varied systematically.

e. Dwell Time

The initiator dwell time could be varied from previously used values to zero. The measurement of dwell time could be linked to the motion of the dispenser piston. This experiment could reduce the possibility of a fuel-lean core.

41

Subsequent to the planning meeting, a specific test matrix was developed for conducting the above recommended experiments. The test matrix as originally proposed appears in Table 3. Tests are designated by the prefix CD (cloud detonation), and the numbering continues in sequence from earlier work. Two repetitions of each test were initially planned. The order of listing represents the sequence priority that was established.

The baseline experiment from which the tests on the matrix were derived had previously been conducted as tests CD6, CD8, CD13, CDP1 and CDP2 (References 2 and 3). In each of these five previous experiments, 0.0265 m^3 (7 gal) of propylene oxide was dispensed at ~1.4 MPa (200 psi) through a dome nozzle head containing 600, 3.18 mm (0.125 in) dia. drilled and countersunk, radially directed holes (nozzles). The initiator in each test was 500 gm of C-4 located 0.421-0.445 m (1.38-1.46 ft) above the virtual center of the nozzle cluster (i.e., above the ground surface). The cloud formation time prior to initiation (fuel dispensing time plus dwell time) was approximately 600 ms. The clouds formed in this time were nominally of 4.6 m (15 ft) radius having a global equivalence ratio of one (stoichiometric).

In the first of the new test series, CD15-16, the initiator would be moved to the edge of the cloud, R = 4.6 m (15 ft). This would yield the largest detonation front radius of curvature as the detonation propagates through the cloud center. A much smaller initiator (but not the minimum thought to be the smallest possible initiator strength) would be used. It would be placed at an azimuthal position such that a line through it and the cloud center would be perpendicular to the line of sight from the north camera position. (Azimuth is specified in the conventional way with respect to the 0° instrumentation leg, as indicated on Figure 1.) The charge would ideally be mounted at zero elevation so as to produce a nearly normal detonation front along the ground surface, simplifying interpretation of any shape changes on passing through the vicinity of the cloud center. However, as the edges of the fuel-air clouds are almost always lifted above the ground surface,

42

TABLE 3

PRELIMINARY MATRIX OF PLANNED FAE EXPERIMENTS
TO INVESTIGATE SECONDARY WAVES

TEST		CLOUD					DISPENSER				INITIATOR[5]			LOCATION		
ID (CD-)	TYPE[1]	FUEL	FUEL QTY. (Gal.)	RADIUS[3] (Ft.)	GLOBAL EQUIV. RATIO[3,4]	FORM. TIME (ms)	NO. NOZ.	NOZ. DIA. (in.)	PEAK PRESS.[3] (Psi)	DISPENSE TIME[3] (ms)	TOTAL MASS (gm)	TYPE[6]	DWELL[3,7] (ms)	RADIUS[8] (ft)	AZIMUTH	ELEV.
15-16	GOI	P.O.[2]	7	15	1	600	600	0.125	200	100	250	SPC	500	14.0	225	10
17-18	CI	P.O.	7	15	1	600	600	0.125	200	100	25	SPC	500	0.5	--	90
19-20	CI	P.O.	7	15	1	600	600	0.125	200	100	90	MCA	500	0[9]	--	--
21-22	ER/DT	P.O.	2.33	10	1	300	1000	0.0860	70	100	25	SPC	200	0.5	--	90
23-24	ER/DT	P.O.	4.67	10	2	300	1000	0.0860	70	200	25	SPC	100	0.5	--	90
25-26	ER/DT	P.O.	7	10	3	300	1000	0.0860	70	300	25	SPC	0	0.5	--	90
27-28	IP	P.O.	7	15	1	600	600	0.125	200	100	50	SPC	500	7.5	45	10
29-30	IP	P.O.	7	15	1	600	600	0.125	200	100	50	SPC	500	7.5	--	90
31-32	IP	P.O.	7	15	1	600	600	0.125	200	100	50	SPC	500	7.5	225	10

NOTES:

1. Test designations
   GOI: Gross Offset Initiation
   CI: Central Initiation
   ER/DT: Equivalence Ratio/Dwell Time
   IP: Initiator Position
2. Propylene oxide
3. Approximate
4. Actual F/A ratio
   normalized with respect to stoich.
   F/A ratio

5. High explosive type C-4
6. SPC: Single Point Charge
   MCA: Multiple Charge Array
7. (Dwell time) = (Cloud formation time)
   - (Dispensing time)
8. Measured from center of nozzle head
9. Effective

43

an elevation angle of 10° was chosen for the initiator position. This is slightly in excess of the normally occuring lifting angle of the cloud edge with respect to the cloud center. At 4.6 m (15 ft) radius, this angle gave an initiator height of 0.8 m (2.6 ft).

As indicated earlier, two techniques were suggested for the "central initiation" tests in order to attempt a reduction in vertical initiator offset. In Tests CD17-18, it was proposed to mount a 25 gm charge at a height of 15 cm (6 in) above the virtual center of the nozzle head. This is a vertical offset of 3.3 percent with respect to the nominal cloud radius. This initiator position is the minimum that could be used without blocking more than the topmost nozzle.

The second recommended technique to generate a central initiator source (Tests CD19-20) would consist of an array of five H.E. charges. Four 10 gm hemispherical charges would be located at 90° spacings around the equator of the dome nozzle head; one spherical 20 gm charge would be located at the pole. This arrangement would provide equal spacing between charges. It is also symmetrical with respect to a mirror image of the hemispherical nozzle head across the ground plane. All five charges in this configuration would be at a radius of 16 cm (6.25 in.) from the center of the nozzle head. The polar charge would be mounted on a vertical rod threaded into the topmost nozzle. The four charges on the equator would be placed on 1/8 in. styrofoam and mounted directly on the top cover of the fuel dispenser.

For this latter initiator configuration, a special cover plate for the dispenser was designed and built. The plate was designed to facilitate mounting the surface H.E. charges. The plate was a retrofit to the fuel dispenser which covers bolt heads and other protruding parts of the dispenser so as to provide a smooth, reflective surface over the entire top of the dispenser. It was designed in such a way that it would directly replace the clamp ring which secures the dome nozzle head to the dispenser body (Reference 2). The five point H.E. charge array was tested in three dry runs

44

in which H.E. charge sizes up to 30 gm were placed on the plate surface and detonated, with no unrepairable damage to the cover plate ring. The simultaneity of the five H.E. charge detonations was also checked in separate tests and found to be better than 1 μs.

An experimental procedure to separately test changes in fuel-air cloud stoichiometry and cloud dwell time could not be devised. With present dispensing hardware it is necessary to change both. To clarify this point, dwell time, τ, is the interval between the end of dispensing and cloud initiation. That is, the total cloud formation time, t_F, is

$$t_F = t_D + \tau ,$$

where t_D is the fuel dispensing time. In order to investigate the effects on an FAE of changing τ, the formation and dispensing times must be incremented in such a way that the difference, $t_F - t_D$, is varied systematically. For this purpose either t_F or t_D can be controlled individually or both could be varied simultaneously. However, any changes in t_F affect the size and geometry of the fuel-air cloud. In addition, if t_D were held constant, the global stoichiometry of the cloud would also be affected by any variations in t_f. The only viable alternative was to maintain t_F constant and to vary τ by incrementing t_D. To do this, the amount of fuel dispensed can be varied. In that way, the overall cloud volume and geometry could be maintained as a control, although the global equivalence ratio would of course vary between tests. This last procedure was the approach selected.

The maximum amount of fuel that can be dispensed with existing hardware is 0.0265 m^3 (7 gal). In a 9.2 m (30 ft) diameter hemispherical propylene oxide (P.O.)/air cloud this amount of fuel yields a global equivalence ratio of approximately one (stoichiometric). Without increasing the capacity of the dispenser, globally fuel rich clouds can only be formed by reducing the cloud size. It was decided to set global equivalence ratios between one (stoichiometric) and three (three times stoichiometric amount of fuel). If

45

0.0265 m^3 (7 gal) of P.O. is used, the cloud diameter should be 6.1 m (20 ft). This requirement necessitated fabricating a new dome nozzle head with smaller, 2.18 mm (0.0860 in) diameter nozzles. Since in previous work (References 2, 3) it was observed that 600 nozzles produced poorly filled-in but reasonably hemispherical clouds, while 1400 nozzles produced well filled-in but more distorted clouds, an intermediate number of nozzles, 1000, was chosen for the new nozzle head.

With respect to dwell time variations in this series of tests, one point of clear interest was zero dwell, in which case a completely fuel-void region in the cloud center would be precluded. This particular condition would be accomplished by setting $t_D = t_F$. With the 1000-hole nozzle head, it was estimated that the highest dispensing pressure for which this matching could be accomplished was ~0.48 MPa (70 psi). At any higher dispensing pressure, t_F would be less than t_D (with 0.0265 m^3 (7 gal) dispensed), while at any lower pressure, fuel atomization would be severely compromised. At 0.48 MPa (70 psi), the estimated cloud formation time was 300 ms. On this basis, the test specifications appearing in Table 3 for FAE Tests CD21-26 were devised.

Three cold, fuel-air cloud formation tests (CF21-23) were carried out in the planning stage to verify the estimates of dispensing and cloud formation times obtainable with the 1000-hole nozzle. In addition, repeatability of the cloud shape was of initial concern when different amounts of fuel were to be dispensed with the same cloud formation time. In each of these three tests, the dispensing pressure was nominally 0.48 MPa (70 psi).

On Test CF21, 0.0265 m^3 (7 gal) of P.O. was dispensed. The approximate dispensing time inferred from fuel manifold pressure measurements was 240 ms. On Tests CF22 and CF23, 0.00883 m^3 (7/3 gal) was dispensed in each case and dispensing times of 110 and 95 ms were measured, respectively.

These dispensing times did not agree with the respective estimates of 300 and 100 ms. However, FAE Tests CD21-26 were

46

specified to incorporate the start and end-dispense indicators described in Section 2.3. The cloud formation time would thereby be set exactly. Using the start dispense switch, a delay generator would be triggered, and after 300 ms delay, this generator would in turn trigger the H.E. detonator. The dwell time would be measured after the test from the time indicated by the end-dispense switch. Therefore, dwell time repeatibility was not thought crucial.

Films taken of the cloud formation on Tests CF21 and CF22 showed excellent cloud shape repeatibility 300 ms after the onset of fuel dispensing. The superimposed profiles of the coulds in these two CF tests at 300 ms are shown on Figure 16 (with equal horizontal and vertical scales).

The last proposed type of experiment to investigate secondary wave origins was a further test of the effects of initiator offset. Such tests would extend and complement the gross-offset initiation experiment as well as the two central initiation experiments (both of which are actually special cases of initiator offset).

Ideally, a group of test conditions would be formulated in which initiator radius, azimuth, and elevation would be individually incremented. Since any test array of that magnitude would be pro-hibitively time consuming, a highly truncated three-test matrix was planned instead. The initiator would in this series be placed at a radial offset equal to 50 percent of the nominal cloud radius. The charges would be located in a vertical plane passing through the centerline of the 45° instrumentation leg. The specific initiator locations (listed on Table 3) were chosen to emphasize offset asymmetry relative to the 45° leg. As in CD15-16, the H.E. charges themselves would be made slightly larger than the anticipated minimum of 25 gm, due to the charge locations in regions of the cloud having uncertain stoichiometry.
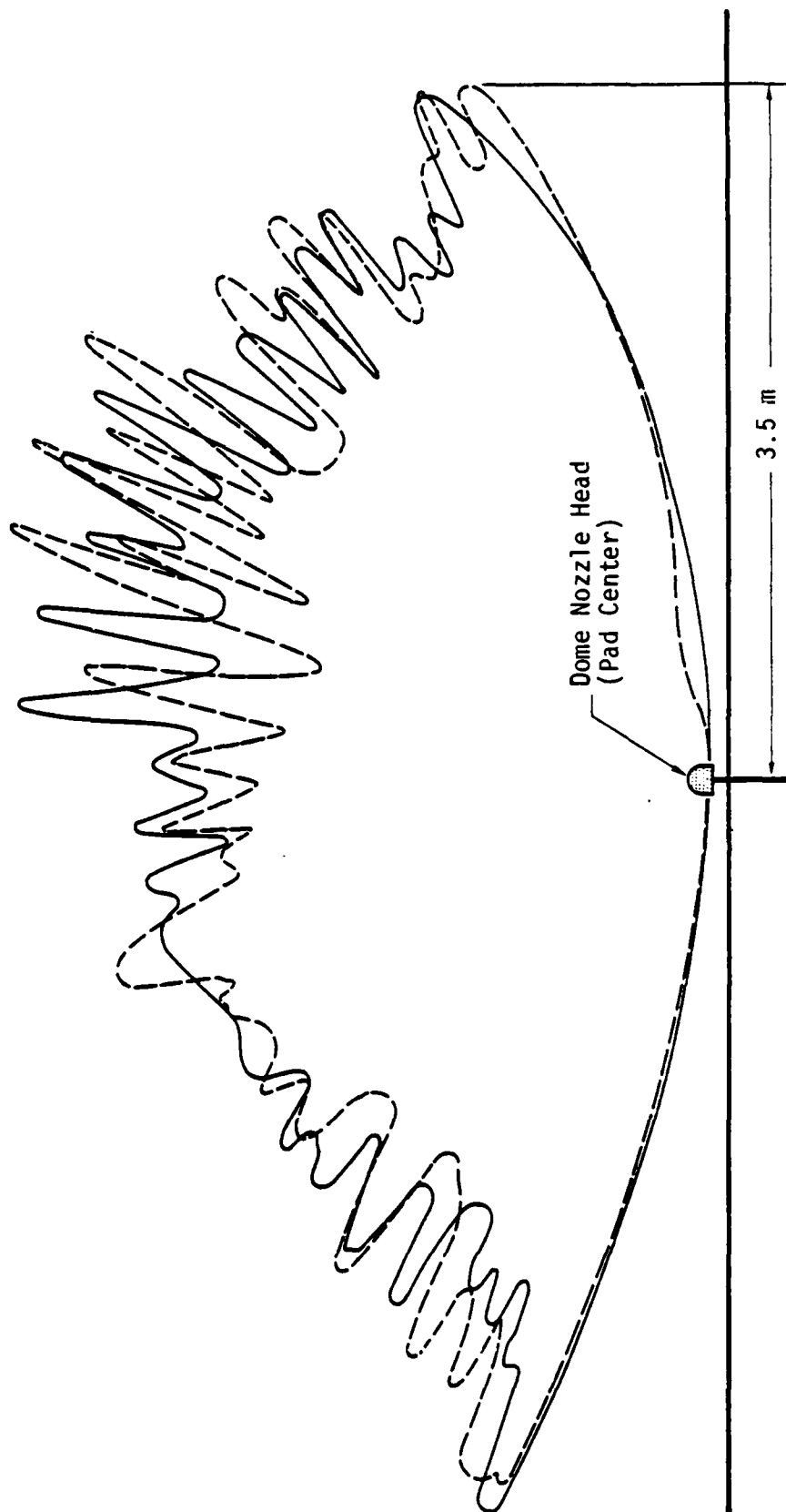
Figure 16. Superposition of cloud boundary outlines from two cloud formation tests at t = 300 ms. Test CF21, 7 gal. fuel dispenser; Test CF22, 7/3 gal. fuel dispensed.

48

4. FAE SECONDARY WAVE EXPERIMENTS

The originally proposed test matrix in Table 3 required several revisions prior to the start of actual testing. It was not possible to conduct all of the experiments that had been recommended due to time and budgetary constraints. Eight fully instrumented FAE tests were ultimately carried out. The test numbering is consistent with the type of experiment, described in the previous section. The conditions for these eight tests are listed on Table 4. One further experiment was conducted to compare acceleration-induced transducer noise on the 0° and 90° instrumentation legs with that on the new 45° leg. This special, preliminary check-out test, designated Test CT-1, is described in Appendix A.

On all tests listed in Table 4, essentially identical pressure instrumentation was used. Changes were made only in the specific transducers used at given locations, and then only in the event of transducer failure. All transducers were placed along the 45° leg on 0.458 m (18 in) spacings. Their locations, with respect to the virtual center of the dispenser nozzle cluster, were as follows: 1.39, 1.85, 2.30, 2.76, 3.22, 3.67, 4.13, 4.59, 5.05, 5.51, 5.96, 6.42, 6.88, 7.33, 7.79, 8.25, 8.71, 9.16, and 9.62 m (4.56, 6.07, 7.54, 9.05, 10.6, 12.0, 13.5, 15.1, 16.6, 18.1, 19.5, 21.0, 22.6, 24.0, 25.5, 27.0, 28.6, 30.0, 31.5 ft).

Kulite transducers were used at the first eight positions; the remainder were PCB transducers. One Kulite gage was used as a dummy at the 4.13 m (13.5 ft) position, mounted in a blind hole on the underside of a transducer mounting block on which an active Kulite gage was also installed. Redundant gages were installed adjacent to primary gages at the 5.05 m (16.6 ft) and 8.25 m (27.0 ft) positions. In each case the redundant gage was of opposite manufacture from the primary gage (i.e., Kulite or PCB).

Photographic instrumentation on Test CD15 is described separately below. On all remaining tests, photographic coverage was provided under separate contract with DNA by Denver Research Institute. Through this arrangement, DRI supplied, set up,

49

TABLE 4

LISTING OF FAE TESTS CONDUCTED

TEST			CLOUD[2]		DISPENSER						INITIATOR[7]		
												Location	
I.D.	Type[1]	Date	Fuel Qty. (gal.)	Form. Time (ms)	No. Noz.	Noz. Dia. (in.)	Peak Press (psi)	Dispenser Time (ms)	Mass (gm)	Dwell (ms)	Radius[5] (ft)	Azimuth	Elevation
CD15B	GOI	10-28-81	7	600[3]	600	0.125	245	159[4]	250	441[3]	14	225	10
CD17A	CI	12-9-81	--	--	--	--	--	--	2000	--	1.04	--	90
CD17B	CI	12-10-81	7	600[3]	600	0.125	NM[6]	150[3]	200	450[3]	1.04	--	90
CD17C	CI	12-11-81	7	588[4]	600	0.125	230	159[4]	200	429[4]	1.04	--	90
CD18	CI	12-11-81	7	590[4]	600	0.125	188	169[4]	50	421[4]	0.63	--	90
CD23	ER/DT	12-12-81	4.67	300	1000	0.086	56	187[4]	200	113[4]	1.33	--	90
CD25	ER/DT	12-12-81	7	300	1000	0.86	102	235[4]	200	63[4]	1.33	--	90
CD29	IP	12-13-81	7	595[4]	500	0.125	212	160[4]	950	435[4]	3.5	--	90

NOTES:

1. Test designations:
   ER/DT (equivalence ratio/dwell time)
   GOI (gross offset initiator)
   CI (central initiator
   IP (initiator position)

2. Propylene oxide

3. Approximate

4. Measured

5. From center of nozzle head to center of charge.

6. No measurement

7. C-4

50

and operated the cameras, and S-CUBED provided all necessary support facilities (electric power, camera triggering, equipment shelving and enclosures, and film processing).

Five high-speed cameras were positioned on shelves in each of the two camera shelters (north and south camera positions). Each shelter was supplied with A.C. power from portable 10 KW diesel generators. Various film types, speeds, and fields of view were used with Fastax, Hycam, and Dynafax cameras. However, the Dynafax, which can achieve framing rates in excess of 20,000 FR/s, was abandoned after two tests. The long-duration light pulse emitted by the FAE led to write-over on the film in this camera. (The Dynafax operates without a shutter, repeatedly exposing a short length of film on a drum.)

In addition to the available-light framing cameras, two streak Fastax cameras were used, in conjunction with a strobe light source and large, expendable Scotchlite panels for shadowgraph photography. The two Fastax cameras were mounted on top of a plywood box built to house the strobe electronics. The box was placed in a trench dug to a depth such that the camera line of sight would approach ground level. This temporary third camera position was located 30.5 m (100 ft) from the center of the 45° instrumentation leg.

The layout of the streak cameras and Scotchlite screen is shown on Figure 17. The Scotchlite reflective sheeting (3M Company) was mounted on 4.9 x 4.9 m (16 x 16 ft) frames constructed of 2 x 4 wood members and covered on one side with 1/4 in. thick hardboard. The Scotchlite sheeting was attached to these frames with roofing nails. Except for a 0.6 x 4.9 m (2 x 16 ft) strip along the top of the frame, the entire frame surface was covered with Scotchlite.

The horizontal position of the Scotchlite screen was varied between tests. A schedule showing the position on each test is given in Figure 17. Without sacrificing too much of the screen in the horizontal direction due to obscuration by the cloud itself, it was hoped that details of the shockfront structure emerging from the cloud could be seen by positioning the screen to overlap the
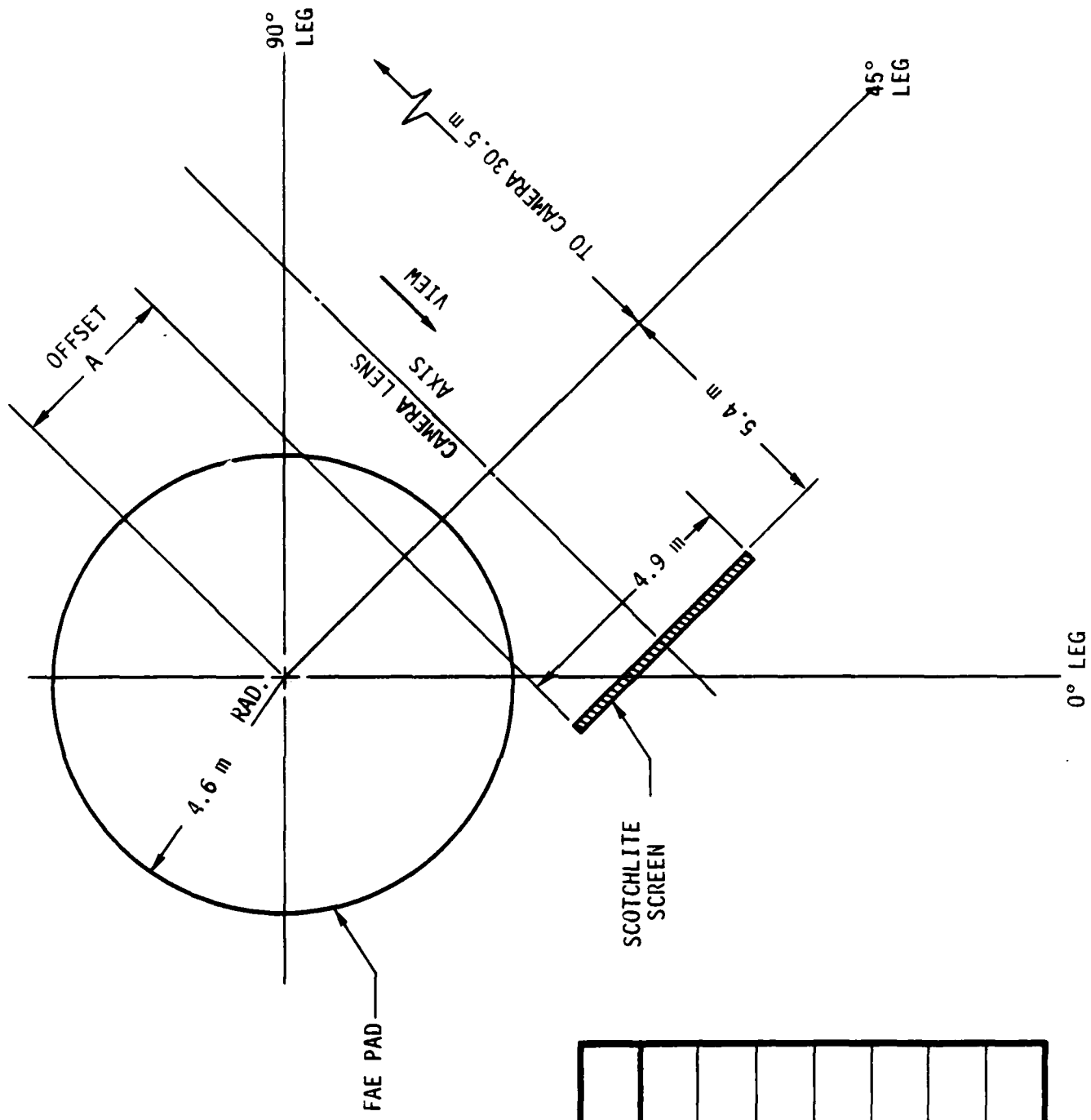
TEST I.D.	A (m)
CD17A	2.73
CD17B	2.73
CD17C	4.74
CD18	2.65
CD23	1.90
CD25	1.90
CD29	2.26

Figure 17. Scotchlite screen layout for shadowgraph photography.

52

cloud edge. (The cloud nominally extends to a radius of ~4.5 m.) This procedure was partially successful, but the film exposure requirements for optimal tradeoff were exacting.

The Scotchlite screen was replaced or repaired as necessary between tests, and frame debris from the previous experiment was removed from the test pad area. All pressure transducers were spot calibrated in situ before and after each test. The pulse pressure transducer calibrator described in Reference 3 was used for this purpose. Heat sink compound was applied to each PCB transducer after the pre-shot calibration was complete. A dry run to test the dispenser gas generator ignition system and the pulsar electronics, which fires the H.E. detonator, preceded each experiment. All of the tests were conducted during periods of complete atmospheric calm.

4.1 Test CD15 (Gross Offset Initiator)

This test was conducted without the extensive photographic coverage supplied in the remaining experiments by DRI. For Test CD15, a Milliken camera operating at 128 fr/s and a Hycam camera operating at 4000 fr/s were placed at the north camera position. A second Hycam camera, operated at 4000 fr/s, was placed at an azimuth of 45° and radial distance of 61 m (200 ft). This latter camera was aligned with the 45° instrumentation leg axis so as to observe the advancing combustion front head on.

A misfire occurred on the first attempt to conduct this test. The problem was traced to a firing circuit malfunction and corrected. The test was repeated on the following day, accordingly designated CD15B.

The fuel-air cloud on Test CD15B was slightly smaller than normal. The maximum radial cloud dimension in the direction of the H.E. initiator was approximately 3.8 m (12.5 ft). The H.E. initiator was at a horizontal range of 4.21 m (13.8 ft) and was not in contact with the cloud. The visible edge of the fuel-air cloud and the position of the H.E. initiator, traced from the Hycam film taken at the north camera position, is reproduced on Figure 18. The
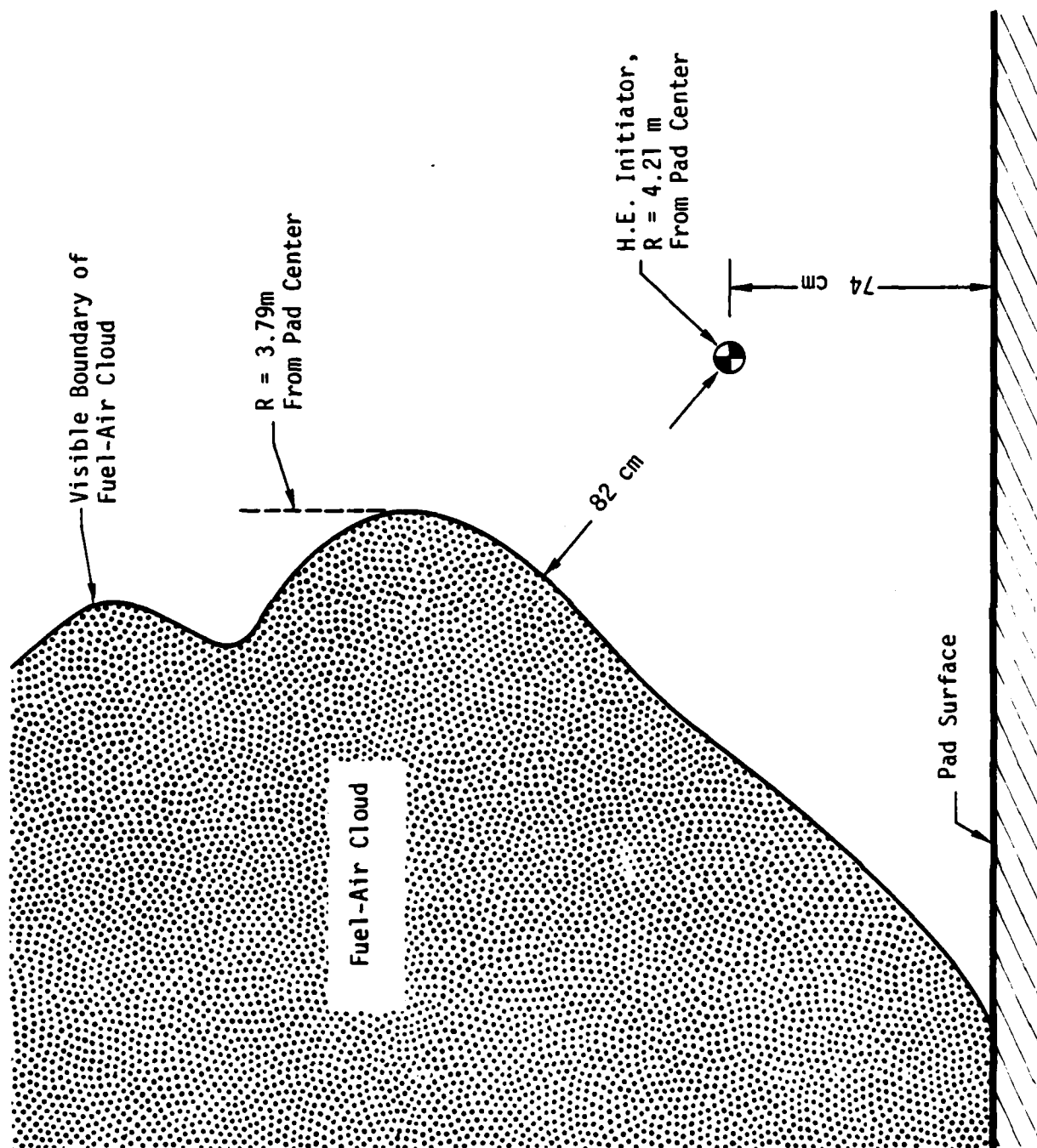
53

Figure 18. Tracing from high-speed film showing edge of fuel-air cloud and initiator location on Test CD15, ~250µs prior to H.E. detonation.

54

distance from the 250 gm initiator to the nearest point of contact with the visible cloud boundary (spray) was 82 cm (2.7 ft). At this distance the blastwave shock would have decayed to a Mach number of about 2.5. The remainder of the cloud was at still greater distances.

The H.E. blastwave failed to initiate the fuel-air cloud to detonation on this test. The late time H.E. fireball ignited a deflagration which propagated through the cloud. Nothing was learned about the initial fuel distribution in the cloud from films of the deflagration, since the blastwave from the initiator, and compression waves from the flame itself, induced significant fuel redistribution ahead of the flame.

The reason for the smaller than normal cloud size was not determined. The fuel dispenser pressure, which cannot be controlled precisely in the existing hardware, was about 8 percent higher than the characteristic value of 1.55 MPa (225 psi). One possibility is that this increased dispenser pressure lead to additional cloud shape distortion (lifting). The higher pressure may also have reduced the reach of individual fuel jets in the nozzle cluster (Reference 2).

4.2   Test CD17 (Central Initiation)

Three repetitions of this test were conducted, designated CD17A, B, and C. Test CD17A failed due to a faulty connector on the cable supplying the firing pulse to the gas generator ignitor. (The gas generator drives the fuel dispenser.) The fuel was not dispensed and the only event on CD17A was H.E. detonation.

Tests CD17B and CD17C were very successful in the sense that the fuel-air cloud formed well and detonated cleanly, and almost all of the extensive pressure and photographic instrumentation operated properly. On these two tests, a 200 gm initiator was located 32 cm (1.04 ft) above the nozzle head center. This is a nominal vertical offset of about 7 percent of the cloud radius.

The results from Tests CD17B and CD17C were very similar. The nineteen primary pressure records obtained from CD17C are presented on Figures 19-22. (On this test the last transducer was moved to

55
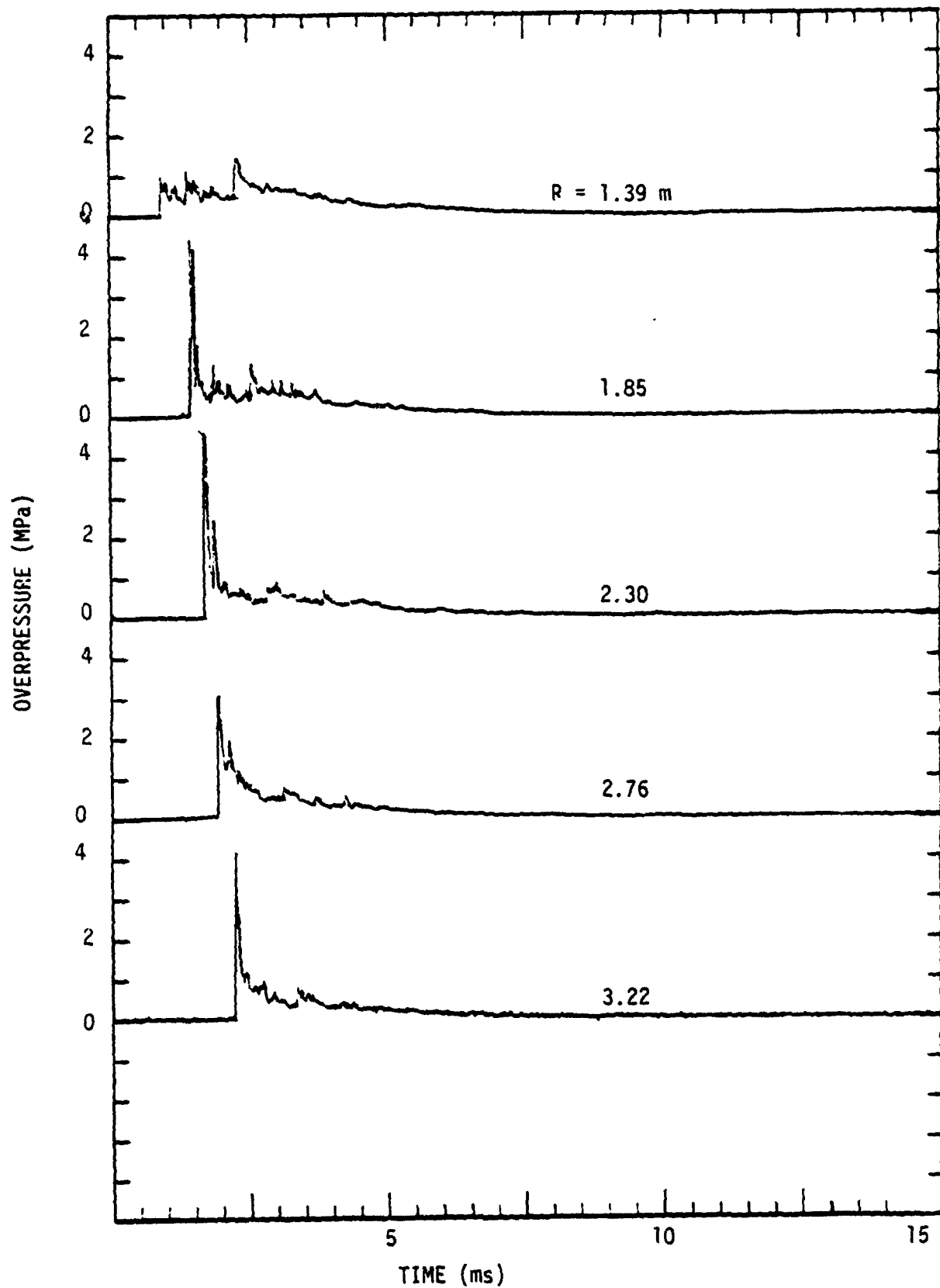
Figure 19. Pressure records from test CD17C, R = 1.39 m to
R = 3.22 m.

Figure 20. Pressure records from Test CD17C, R = 3.67 m to R = 5.51 m. Region below and to left of dashed line is visible on shadowgraph films.

57

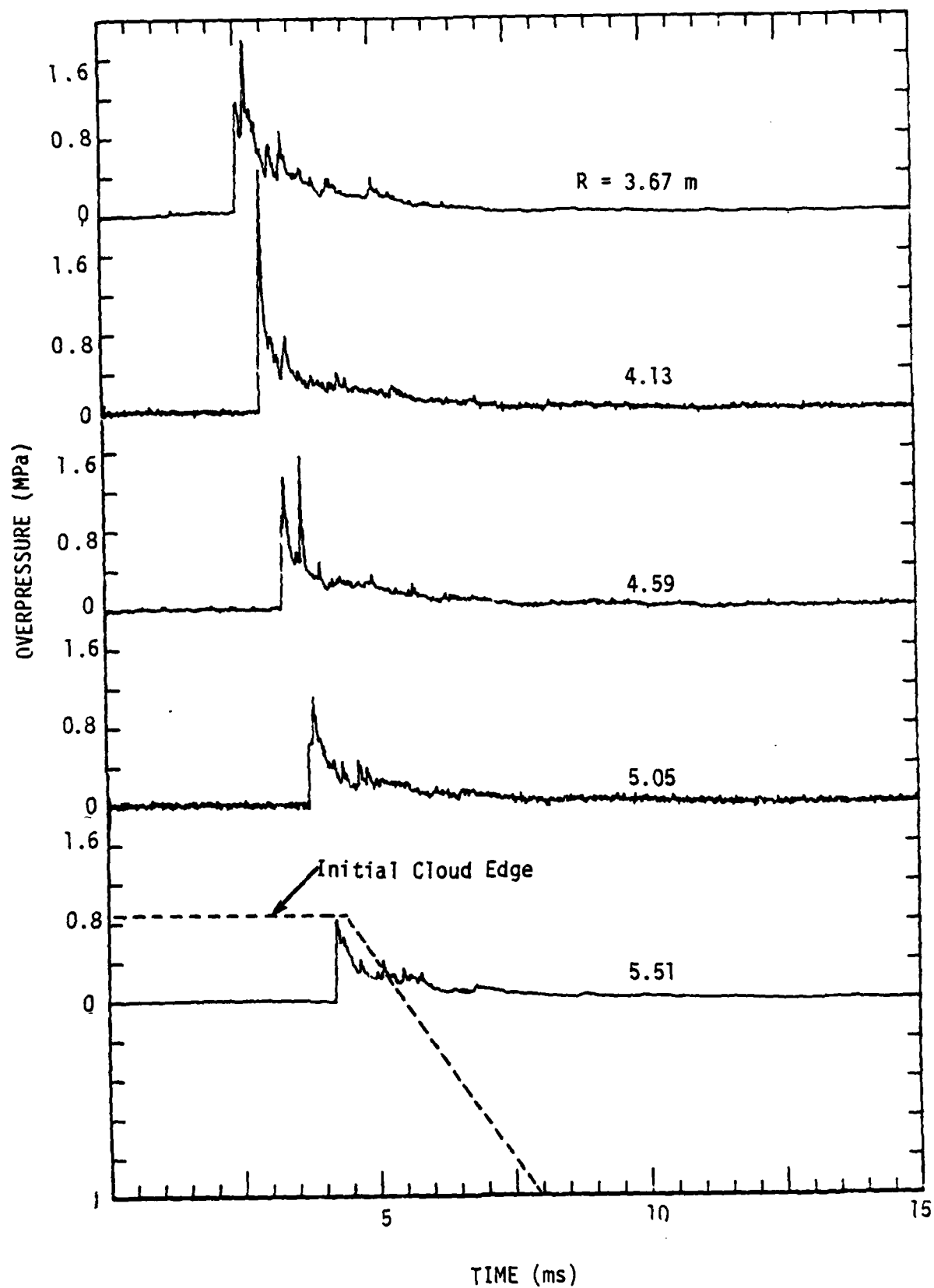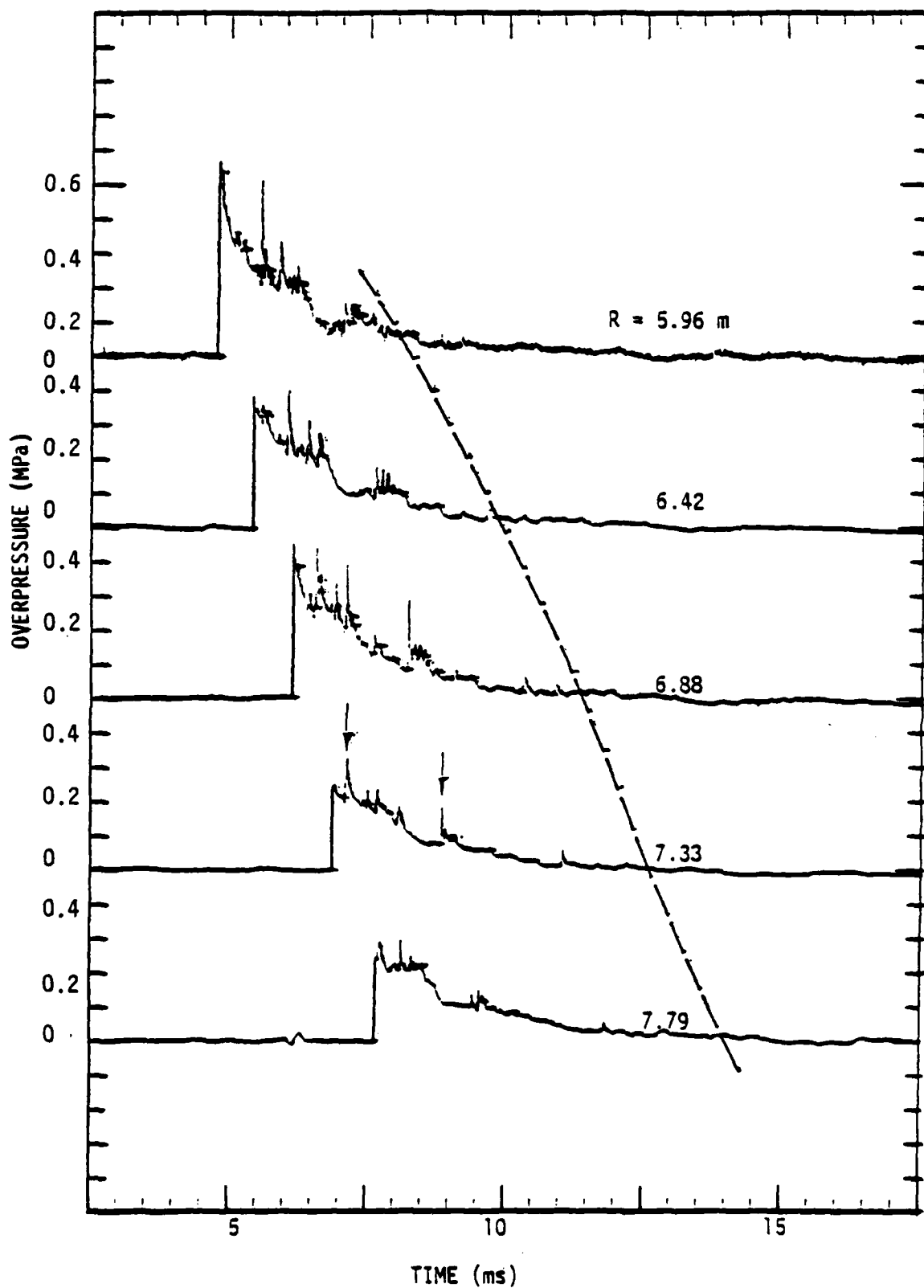Figure 21. Pressure records from Test CD17C, R = 5.96 m to R = 7.79 m. Region to left and below dashed line is visible on shadowgraph films.
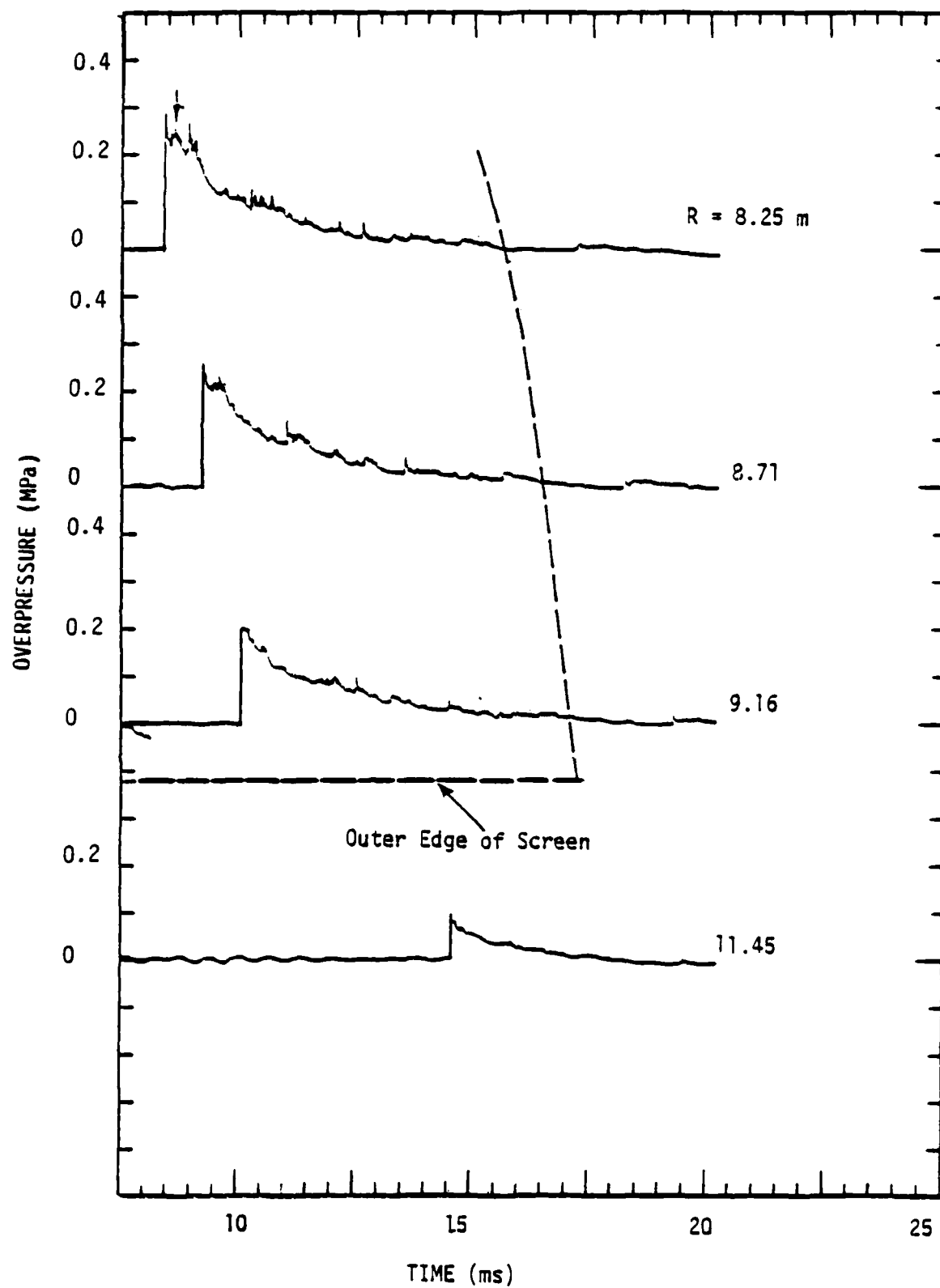
Figure 22. Pressure records from Test CD17C, R = 8.25 m to
R = 11.45 m. Region to left of dashed line is
visible on shadowgraph films.

59

the most distant position possible on the 45° leg, 11.45 m (37.5 ft)). The dashed line sketched on these figures represents roughly the usable limits of the streak shadowgraph photography. This region was bounded by the physical size of the Scotchlite screen on one side, and on the other by an effective boundary resulting either from obscuration by the expanding FAE fireball or by the progressive breakup of the screen framework. As can be seen, most of the features of interest on this test were included within this region made visible by shadowgraph photography.

A series of shadowgraph photographs from Test CD17C (taken from the strobe/streak high speed film) is given on Figures 23-26. The shockfront surface was bulged as it emerged from the cloud, a characteristic that appeared to correspond to the fuel-air cloud shape. This bulge quickly healed, however, after the blastwave front separated from the cloud. The two secondary shock fronts that extend to the ground in Figure 24 occur approximately at the positions marked with arrows on the 7.33 m pressure record on Figure 21. With further expansion, the blast front became increasingly uniform and the secondary waves merged with the leading shock. The long, single secondary shock seen extending to the ground on Figure 25 corresponds approximately to the position marked by an arrow on Figure 22.

This stage of the blastwave development was reached slightly earlier in Test CD17B. Figure 27, which was taken from CD17B, compares in range with Figure 24. It was noted with interest that the long, secondary shock was repeated on both of these tests.

Many of the pressure excursions on the transducer records could not be correlated with features on the shadowgraph films. Those waves which could be seen on these films appeared to emerge from within the cloud, but the image of the cloud itself, which shows as a blurred streak through the film, obscurred their origins. Although none were visible on the shadowgraphs, this left in question the possibility of transverse-moving waves (i.e., in a generally vertical direction).
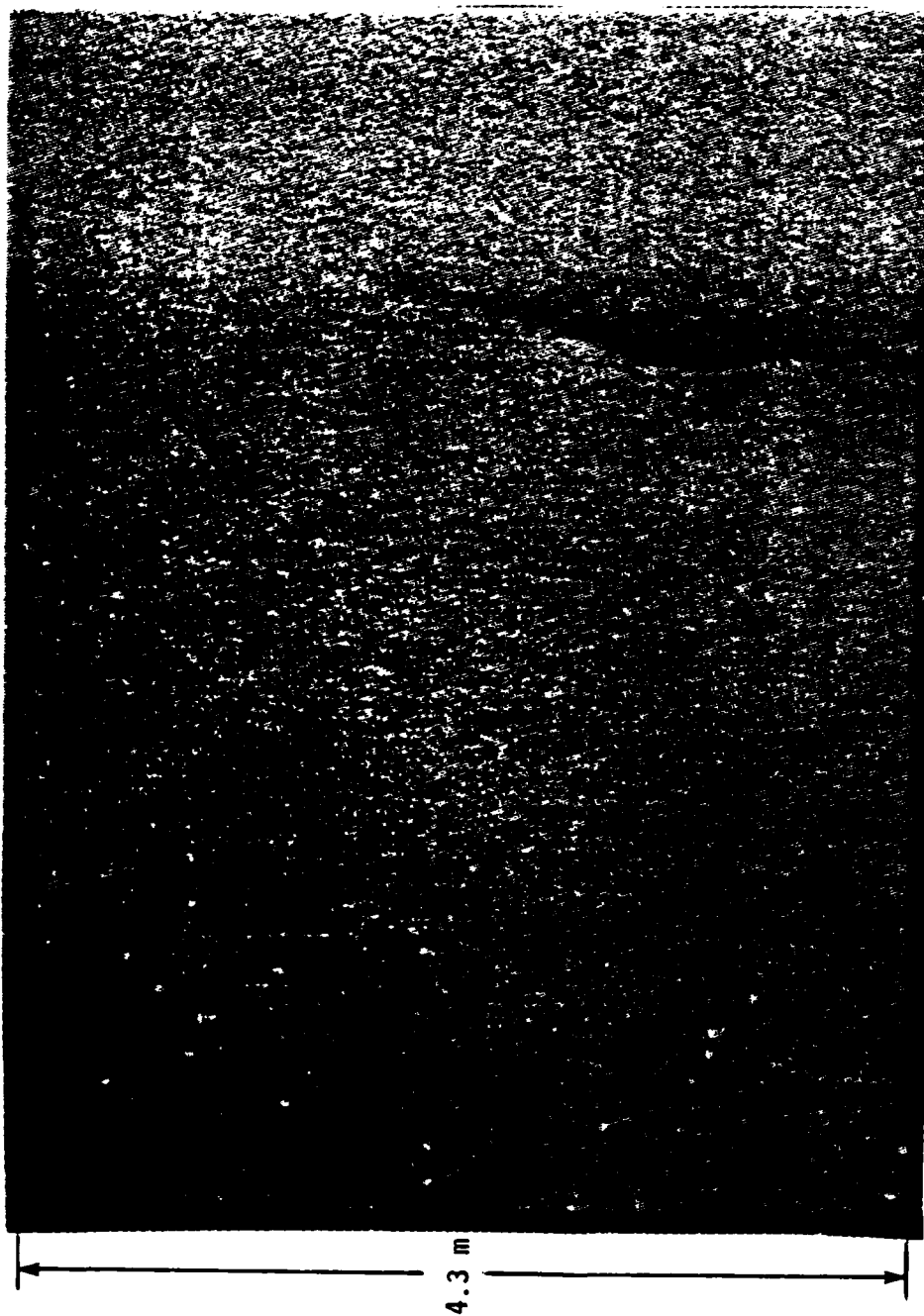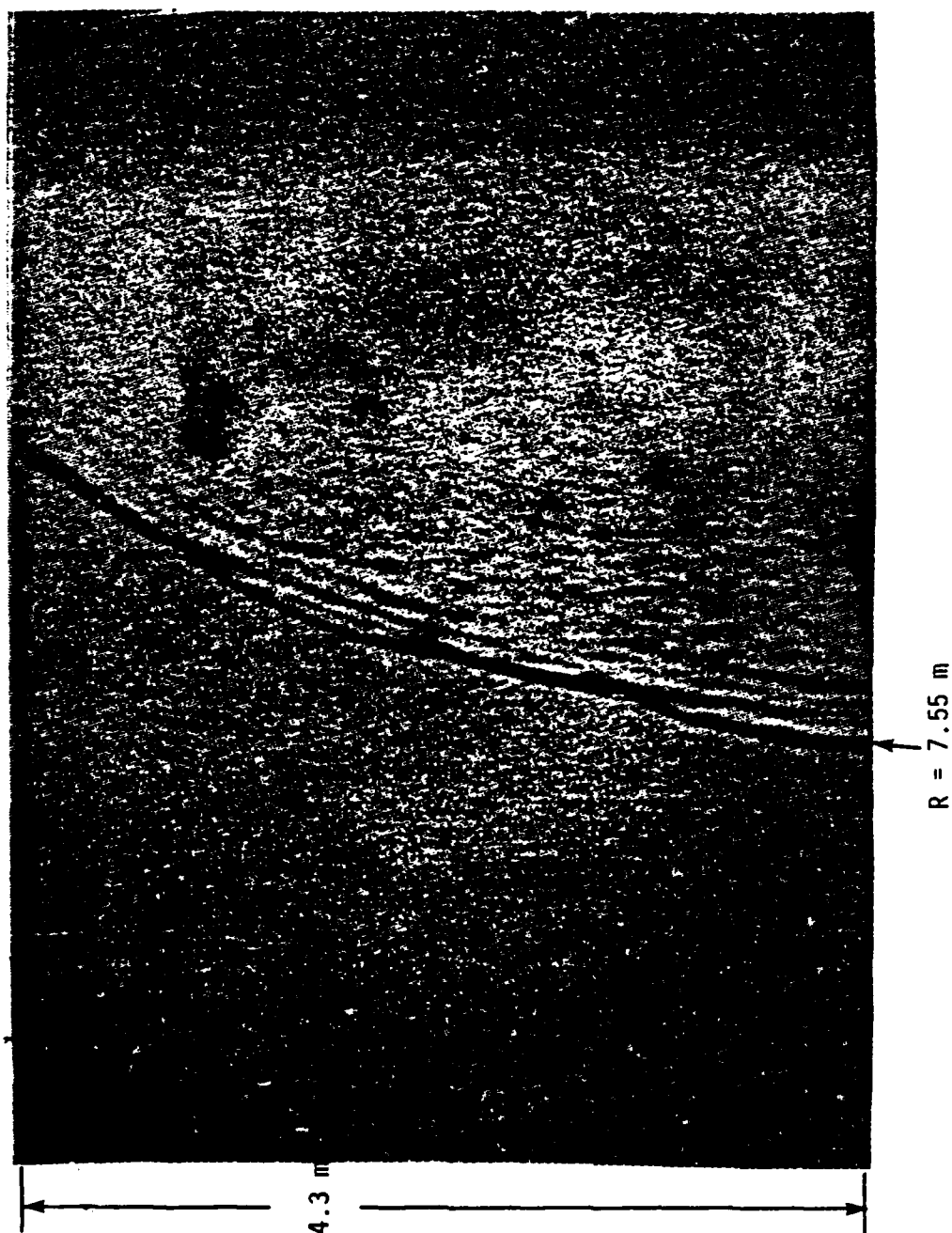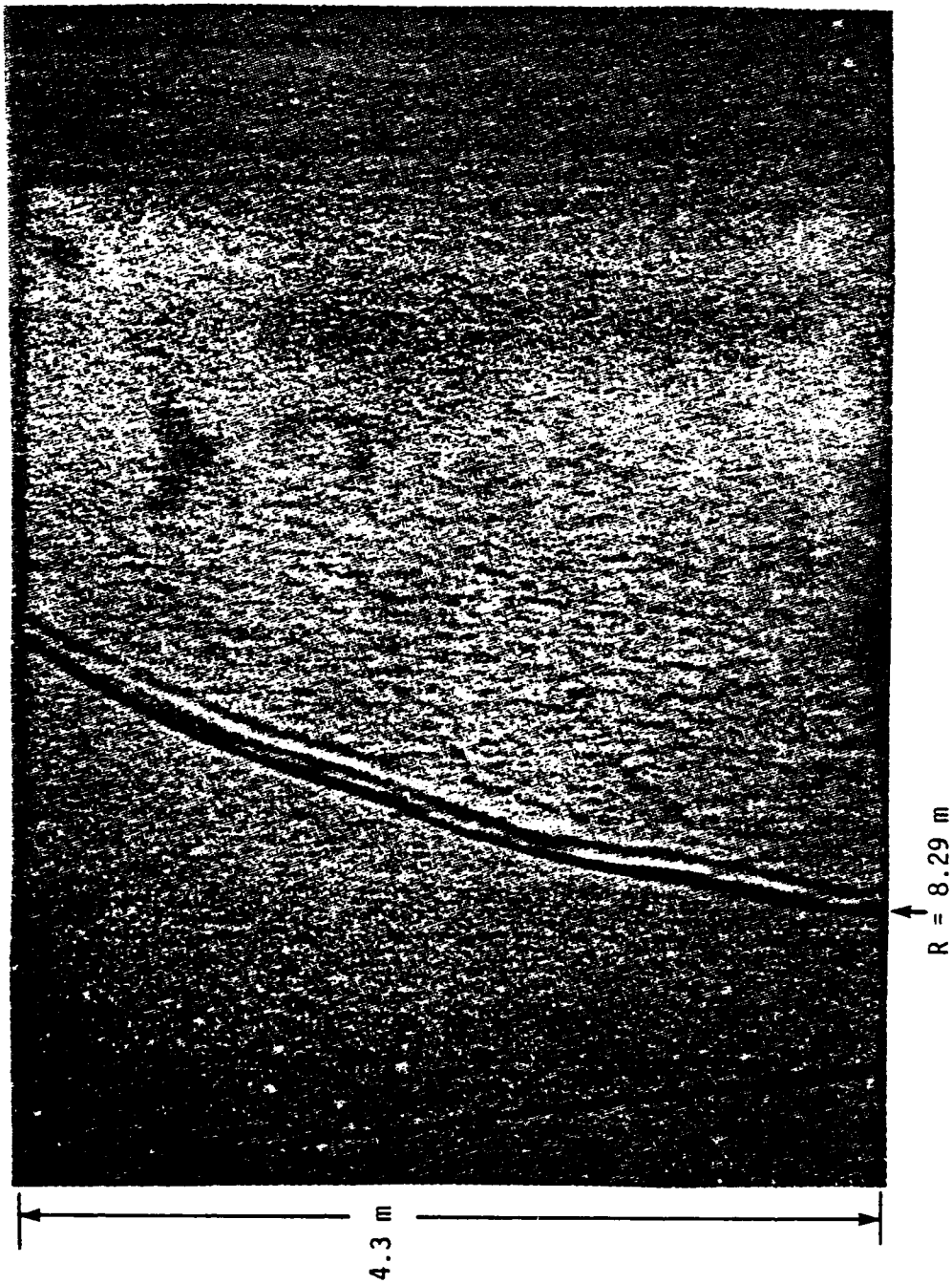
R = 5.58 m

4.3 m

Figure 23. Shadowgraph photograph, from Test CD17C.

Figure 24. Shadowgraph photograph from Test CD17C.

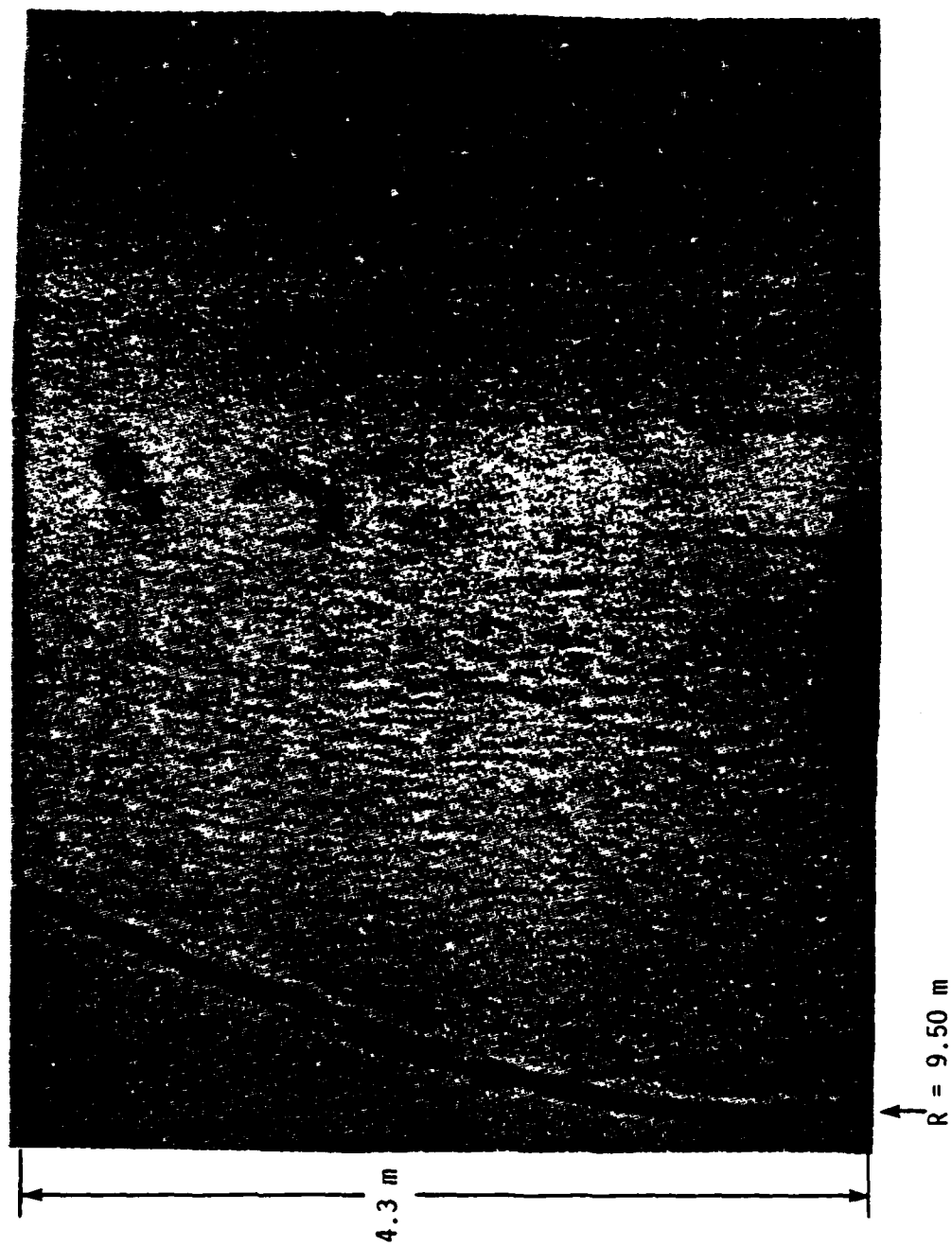R = 7.55 m

4.3 m

Figure 25. Shadowgraph photograph from Test CD17C.

4.3 m

R = 8.29 m

4.3 m

R = 9.50 m

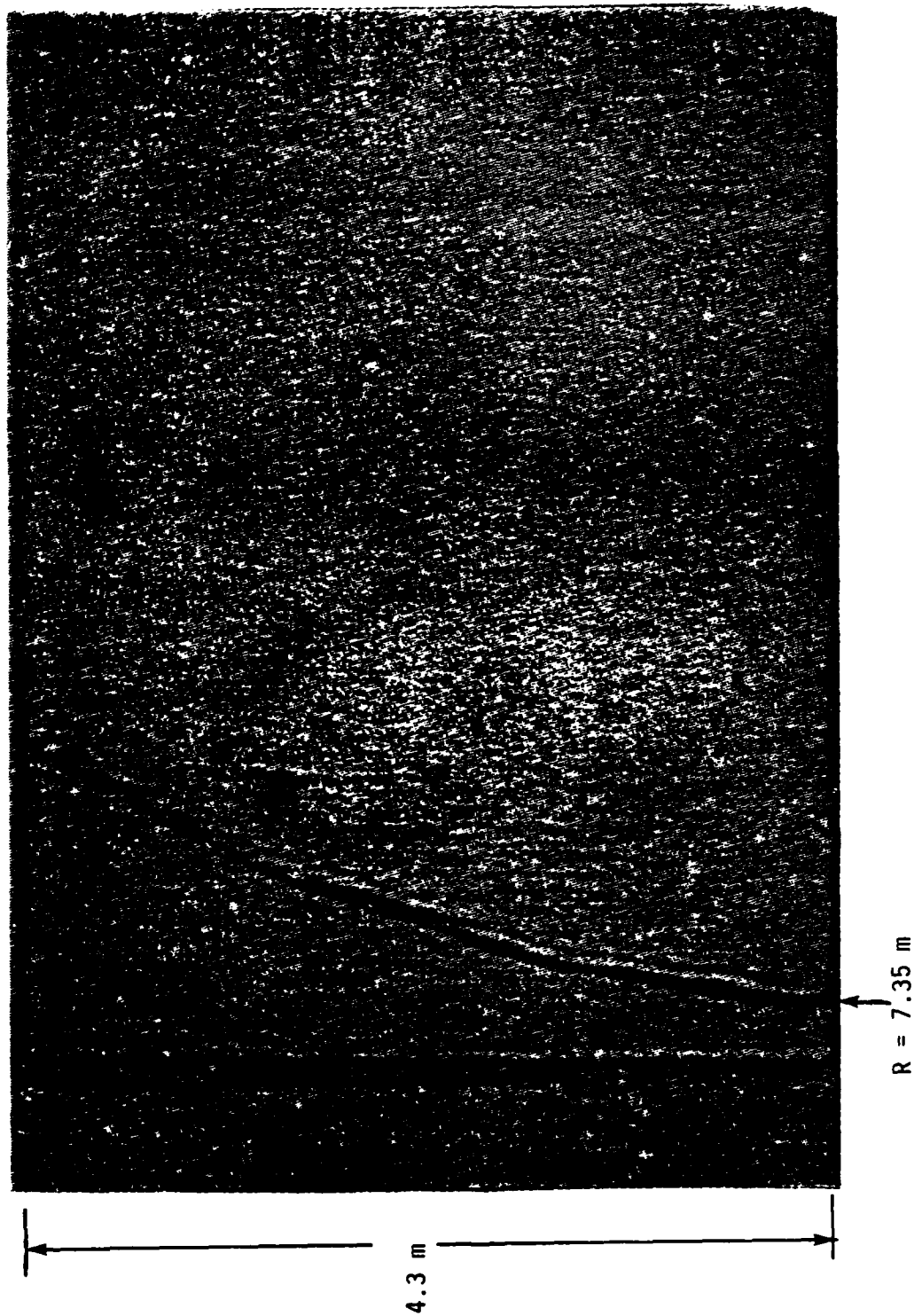Figure 26. Shadowgraph photograph from Test CD17C.

64

Figure 27. Shadowgraph photograph from Test CD17B, t = 6.48 ms.

R = 7.35 m

4.3 m

In an attempt to track the secondary waves further, the pressure records on Figures 19-22 were replotted in a three-dimensional format, Figure 28. Here several groups of waves can be seen propagating toward the lead shock. It was difficult to clearly identify many of the individual wave packets at radii much smaller than 3-4 m. At greater radii, they were relatively clear. It appeared from this plot that the wave groups developed from phenomena occurring within the clouds, but the specific source was not obvious.

Within the cloud, the pressure-time plots show peaks that are considerably in excess of the normal detonation pressure (which is about 1.7 MPa). This was thought to be due to reflection of the FAE detonation from the ground, since the initiator was not surface-flush.

The detonation front velocity, measured from times of arrival at the transducers, was near the stoichiometric theoretical value of 1800 m/s only at radii less than about 2.5 m (8.2 ft). This was the case on both Tests CD17B and CD17C (Figure 29). Beyond that range the front velocity rapidly fell below the lean and rich limit detonation velocities (1520 m/s and 1620 m/s, respectively). These subnormal velocities suggest a marginal detonation initiation condition.

The front velocity also appeared to be resurgent. This was especially noticible on CD17C wherein the front velocity increased over the first 2.5 m and then dropped off. Outside the cloud, sudden increases in wave velocity (such as that at 5.76 m on CD17B) are believed to be caused when compression wave packets overtake the blastwave leading shock. Beyond a range of about 6 m, both tests displayed little further front velocity irregularities. Some of the apparent resurgence, however, may be attributable to errors in interpretation of times of arrival (TOA) from the pressure records. For example, two independent readings of TOAs on test CD17C were made. Both are plotted on Figure 29. The average error between the two readings was 4.7 percent, and the extent of resurgence differed between the two readings.
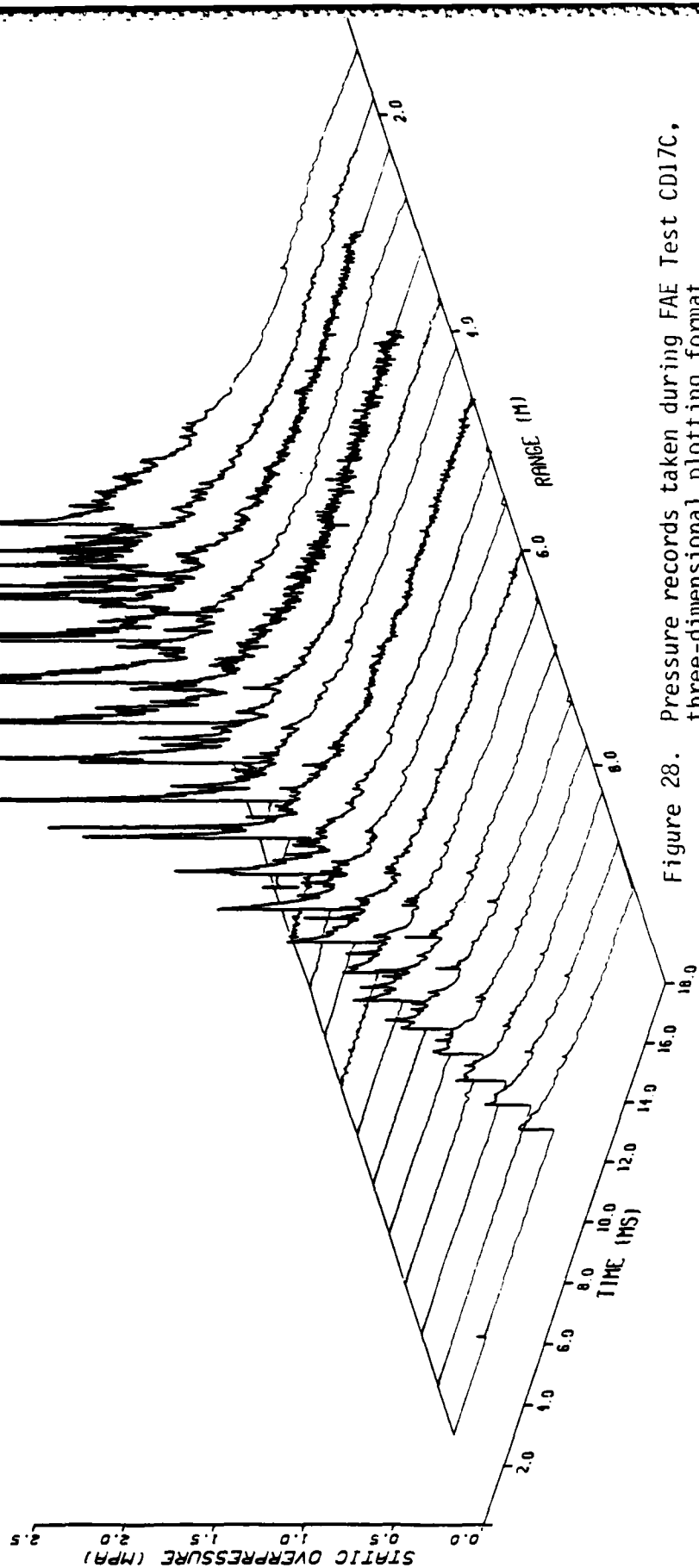
66

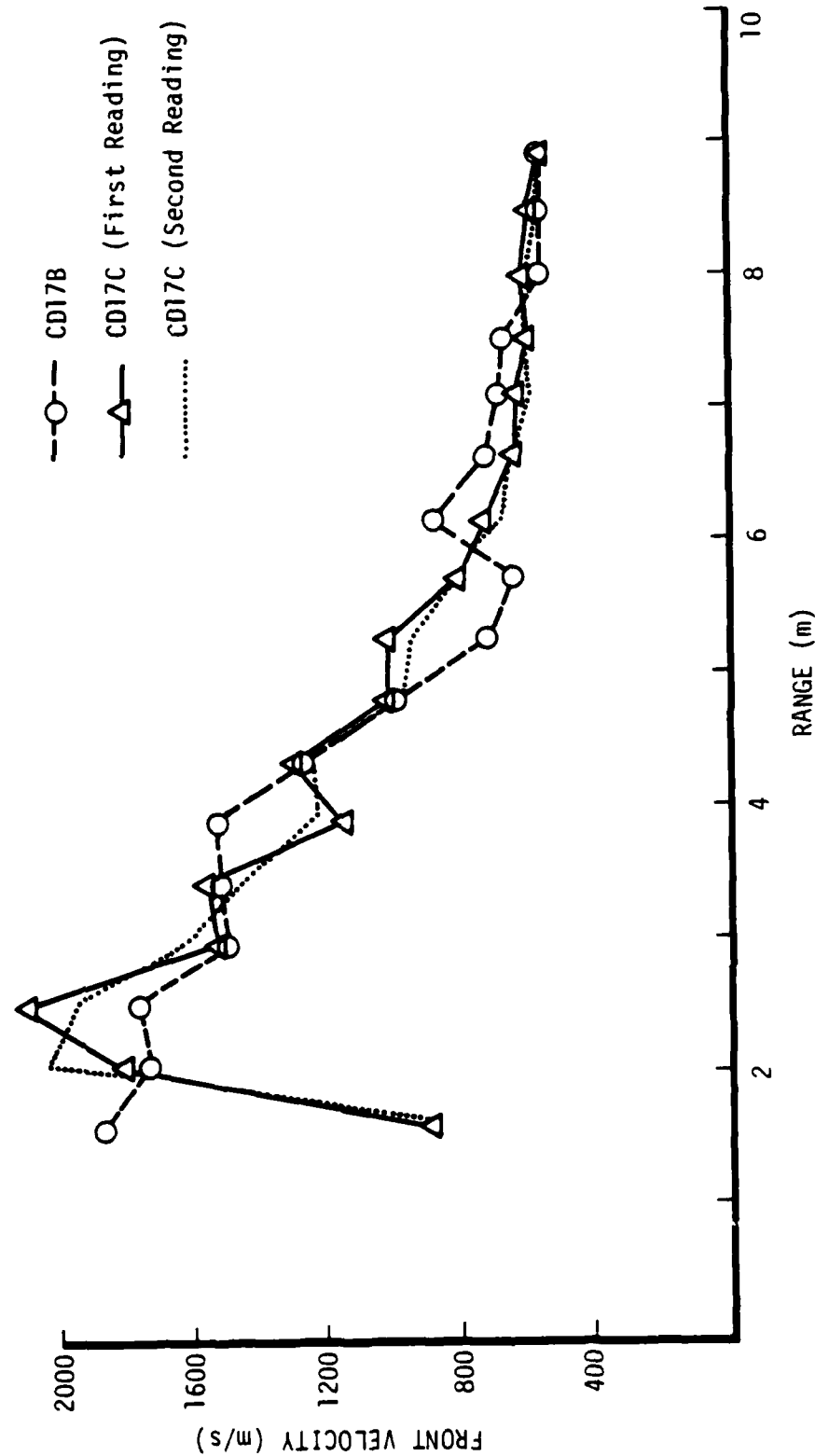Figure 28. Pressure records taken during FAE Test CD17C, three-dimensional plotting format.

Figure 29. Shock front velocity versus range on Tests CD17B and CD17C, from time of arrival data.
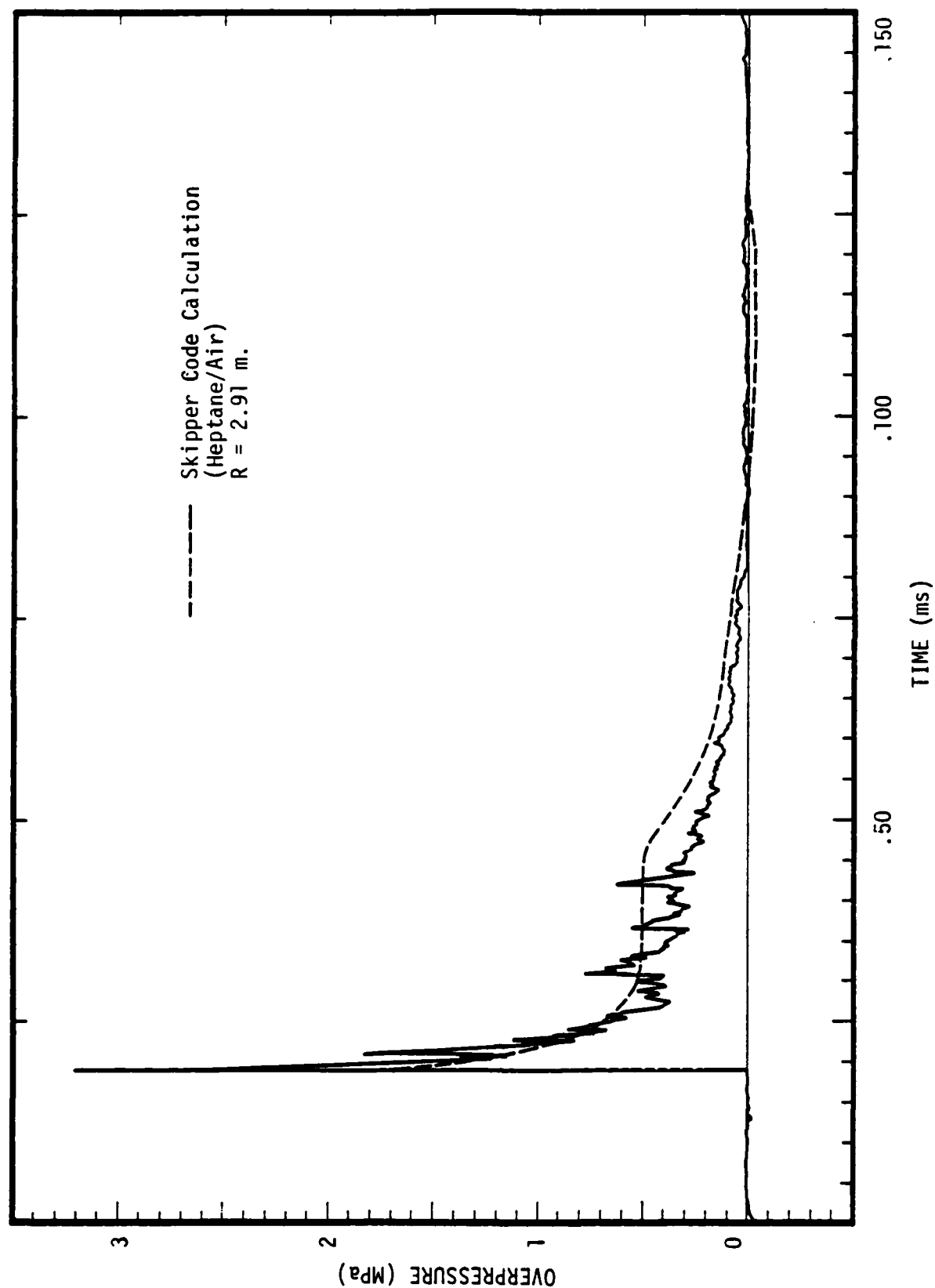
68

Figure 30. Comparison of pressure record during Test CD17C at R = 2.76 m with calculated pressure-time profile for similar FAE cloud at R = 2.91 m.

One of the pressure records from the set taken on Test CD17C nas been reploted on Figure 30. The qualitative character of this trace is characteristic of the pressure histories at positions under the cloud, on both tests. The average overpressure dropped rapidly in the first millisecond, leveled off for about 2 ms, and then finally decayed smoothly to zero.

To help interpret this particular waveform, the pressure-time curve from a numerical calculation (Reference 2) at approximately the same radial position has been superimposed on Figure 30. The calcultion was carried out for a hemispherical heptane-air FAE cloud with roughly the same total energy release as the experimental propylene oxide fuel-air clouds.

From the calculation, the origin of the pressure plateau seems clear. In an ideal fuel-air explosion, the pressure-radius profile is self-similar, consisting of a monotonic decay from the shock front, until a level which is approximately 1/3 the front pressure is reached at about half the front radius. Further inward, the pressure is constant to the explosion center. Therefore, at any fixed position near the cloud center, the pressure will rise to the detonation front level, decay to about 1/3 this level, and then remain constant. However, because the fuel-air cloud is of finite dimensions, the expansion wave reflected from the cloud/air interface will eventually pass over the fixed point (as it propagates toward the cloud center), relieving the pressure there. The resulting temporary pressure plateau is not the development of a secondary wave but rather a natural characteristic of fuel-air explosion.

The cellular character of the detonation front as it emerged from the cloud was made easily visible on infared films. Figures 31 and 32 are frames from films taken from Test CD17C in which this type of film was used (Figure 32 is a frame from a split-frame camera). With infared film it was possible to see through the

Figure 31. Frame from high-speed camera with infrared film taken during Test CD17C. Cloud radius is approximately R = 3.95 m, time is approximately t = 2.4 ms.
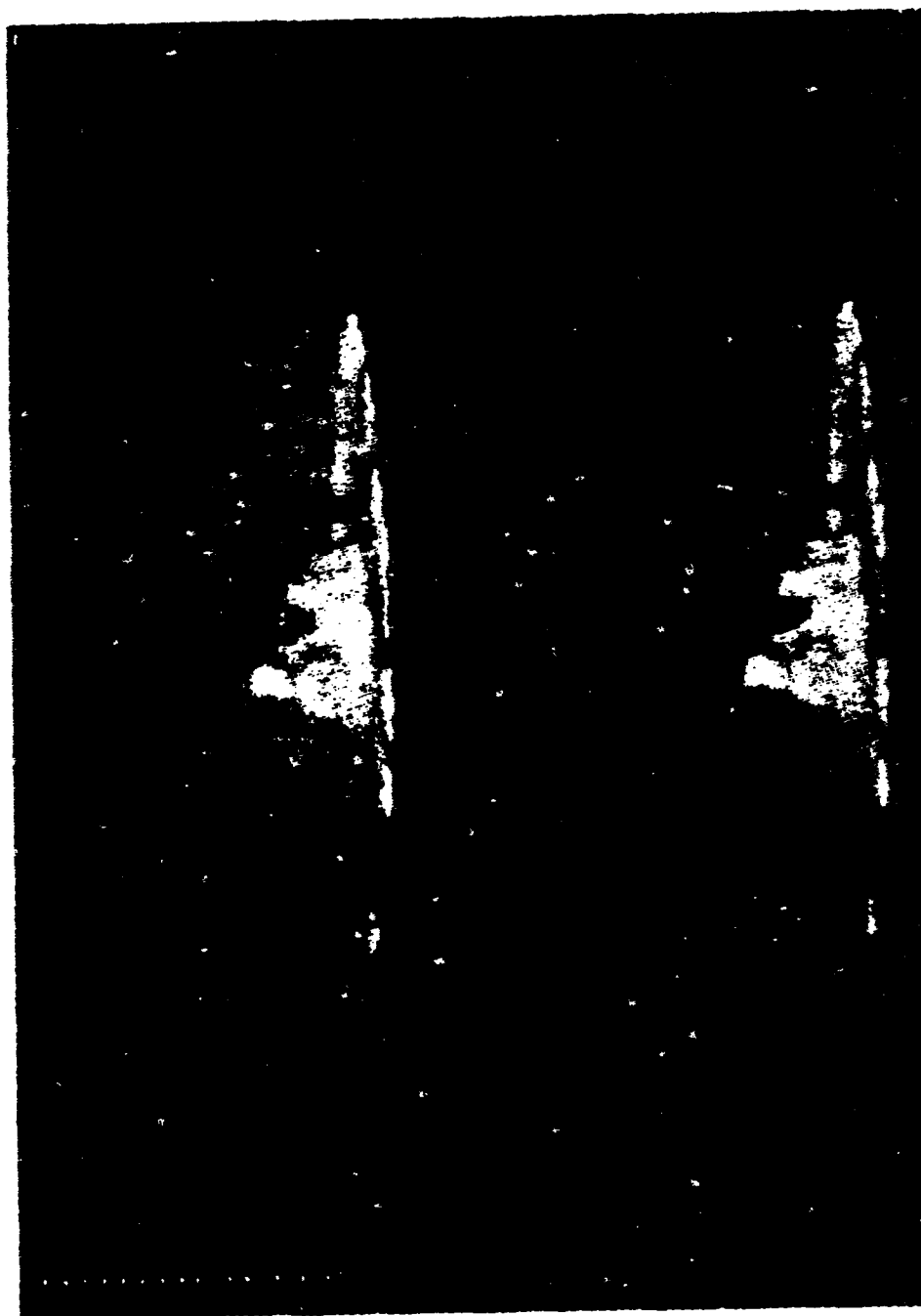
71

Figure 32. Split frame from high-speed camera with infrared film, Test CD17C.

cloud. The illuminated oval footprint of the detonation on the con-
crete pad is clearly visible as are the detonation products. The
combustion appears to be nonuniform in the cloud, with many luminous
pockets. When the high-speed film was viewed at 16 fr/s, the
detonation seemed to sparkle internally, as though these pockets
were igniting at different times. The inference from these films
was that some of the unmixed fuel and air in the cloud had reacted
after a time delay associated with secondary mixing (following
initial passage of the detonation front).

4.3   Test CD18 (Central Initiation)

This test was identical in all respects to CD17 except for the
initiator size and height (Table 4). On test CD18, the 50 gm
initiator was located at the minimum possible height above the
ground, 0.192 m (0.63 ft).

The cloud on Test CD18 formed well and the initiator triggered
properly. The cloud deflagrated. The initiator blastwave, made
visible by the spray, appeared to be very symmetrical until it
passed the cloud boundaries. The blastwave caused an increase in
the nominal radius of the cloud of about 10 percent by dragging fuel
droplets behind it.

The initiator blastwave was also faintly visible on the
strobe/streak shadowgraph films using the Scotchlite screen. The
blast front appeared to be slightly wavy but quite hemispherical on
these films. A Mach wave was not seen, nor were there any visible
secondary waves. Figure 33 is the pressure record nearest the
initiator. There was no indication of any anomalies in this record.

That the cloud failed to detonate on this test indicated a
marginal initiator strength or sub-minimal initiator height.
Detonation was initiated twice (on CD17B, C) with a 200 gm charge at
0.32 m (1.04 ft), but on CD18 initiation was not successful with a
50 gm charge at 0.192 m (0.63 ft). In earlier experiments
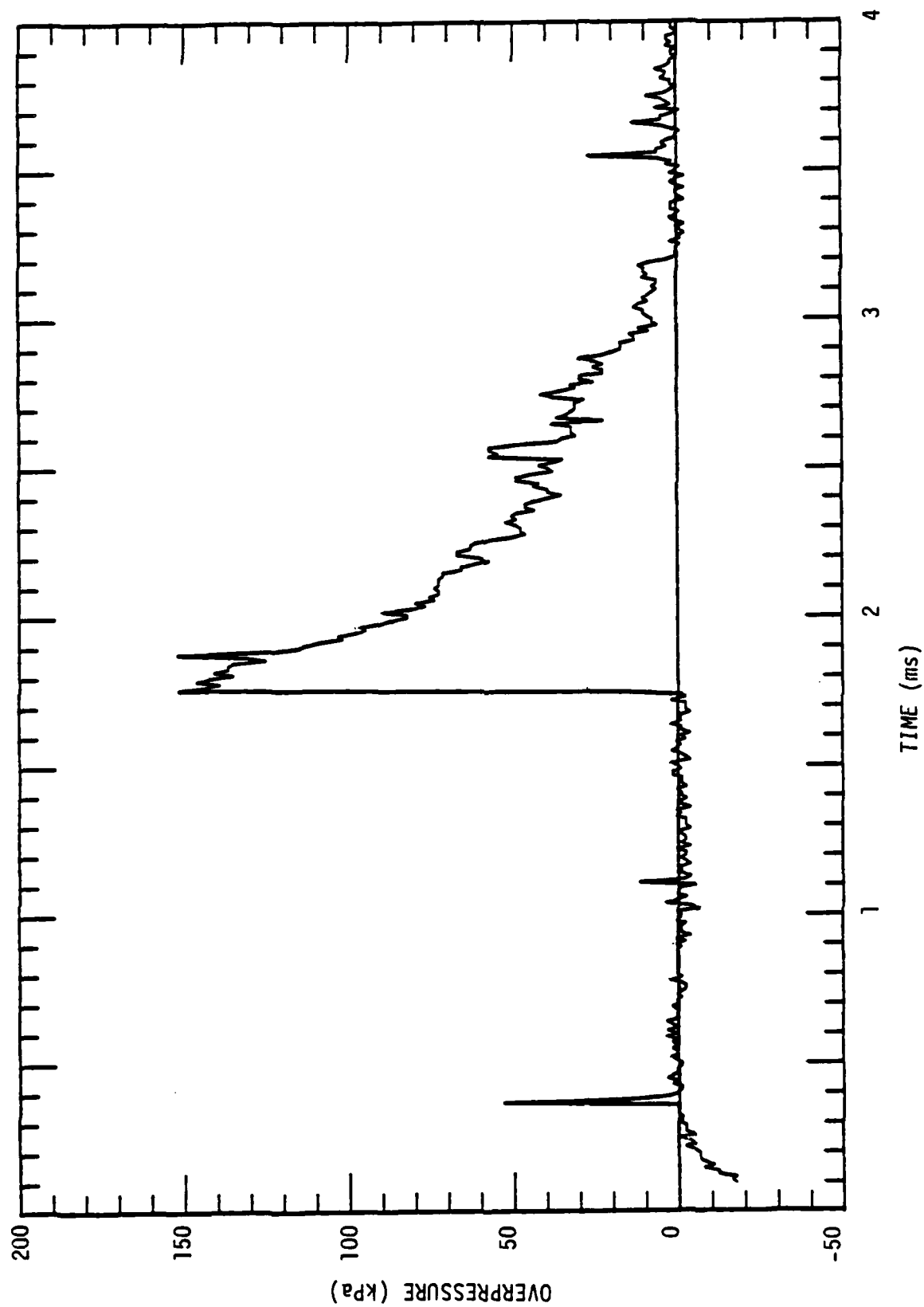(Reference 1), 25 gm charges had repeatedly been used with success

73

Figure 33. Pressure record from Test CD18 at R = 1.39 m.

to initiate similar propylene oxide/air clouds. However, the charges in those tests were located much higher in the clouds, and a longer dwell time was used (more fuel vapor). On Test CD18, it was thought that insufficient fuel vapor had collected in the vicinity of the initiator.

4.4   Tests CD23 and CD25 (Equivalence Ratio/Dwell Time)

Chronologically, Test CD25 was conducted before Test CD23. Test CD25 was an experiment in which three times the stoichiometric quantity of fuel was injected into a fuel-air cloud. At the same time, the dwell time was to have been near zero. However, the dispenser gas generator produced a higher than normal pressure on this test, and the resulting dispensing period was thereby reduced so that it was 63 ms short of the cloud formation time (i.e., the actual dwell time was 63 ms).

Test CD23, on the other hand, was to have a nominal dwell time of 100 ms. This was attained with reasonable approximation. Test CD23 was a test in which the cloud contained twice the stoichio-metric quantity of fuel. In both experiments, a 200 gm initiator was used in place of the originally planned 25 gm, in view of the experience on Test CD18.

Detonation was not achieved on either Test CD23 or CD25. In both cases, the initiator blastwave caused a significant increase in the cloud size and altered its shape (Figure 34). Also, on both tests, as the blastwave emerged from the cloud, a clear Mach reflec-tion was visible on the strobe/streak films (Figures 35 and 36). The shadow of the cloud edge, cast on the Scotchlite screen, shows the relation of these Mach reflections to the cloud.

Although detonation was not achieved in Tests CD23 and CD25, the test results may nevertheless have significance with regard to secondary wave formation. Figures 37 and 38 are pressure traces taken just beyond the cloud boundaries on CD25 and CD23, respec-tively. (The noise level was high on these traces since amplifier gains had been set in anticipation of pressures one order of magnitude greater.)

75

(a)
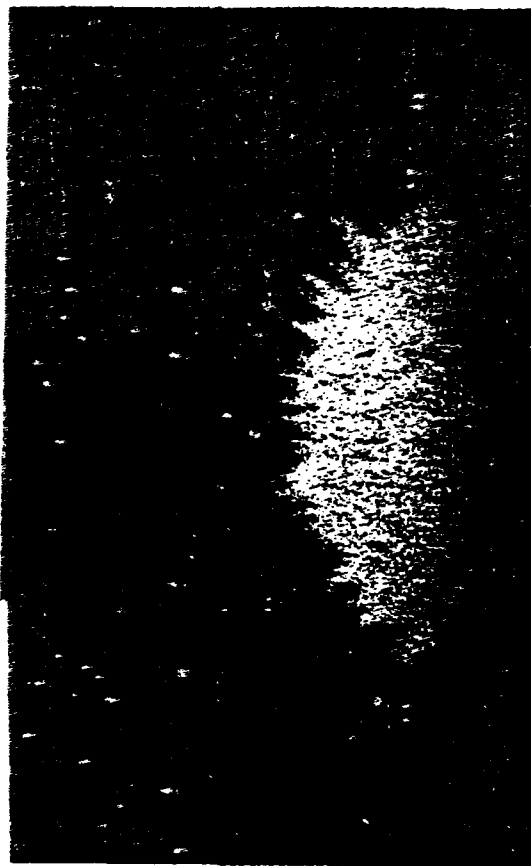
(b)

Figure 34. Fuel-air cloud expansion caused by blastwave from sub-minimal H.E. initiator, Test CD25. (a) Just prior to H.E. initiation, cloud vertical height is 2.83 m, horizontal width is 5.37 m. (b) Following passage of blast wave but prior to flame propagation. Cloud height is 3.09 m, width is 6.97 m.
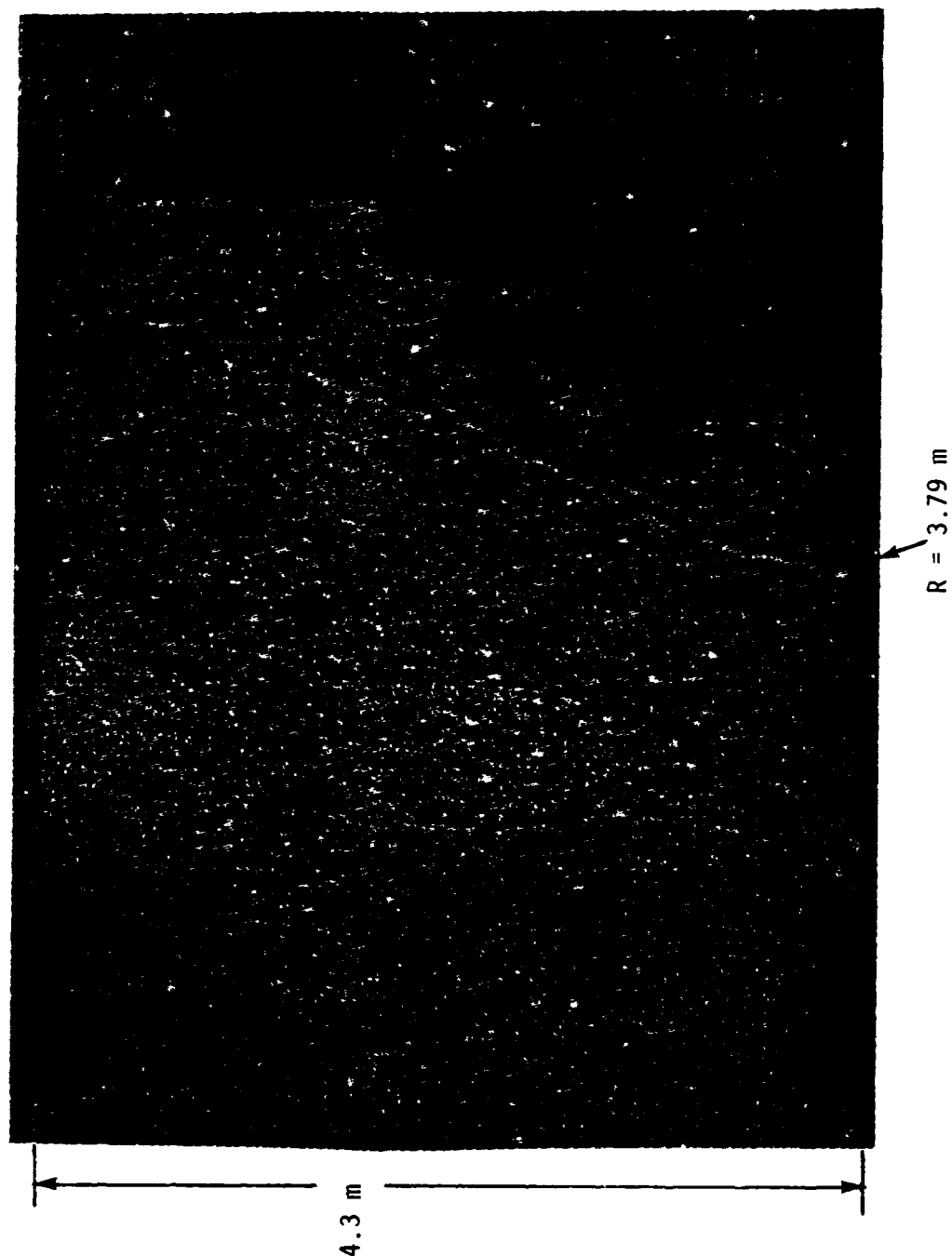
4.3 m

R = 3.79 m

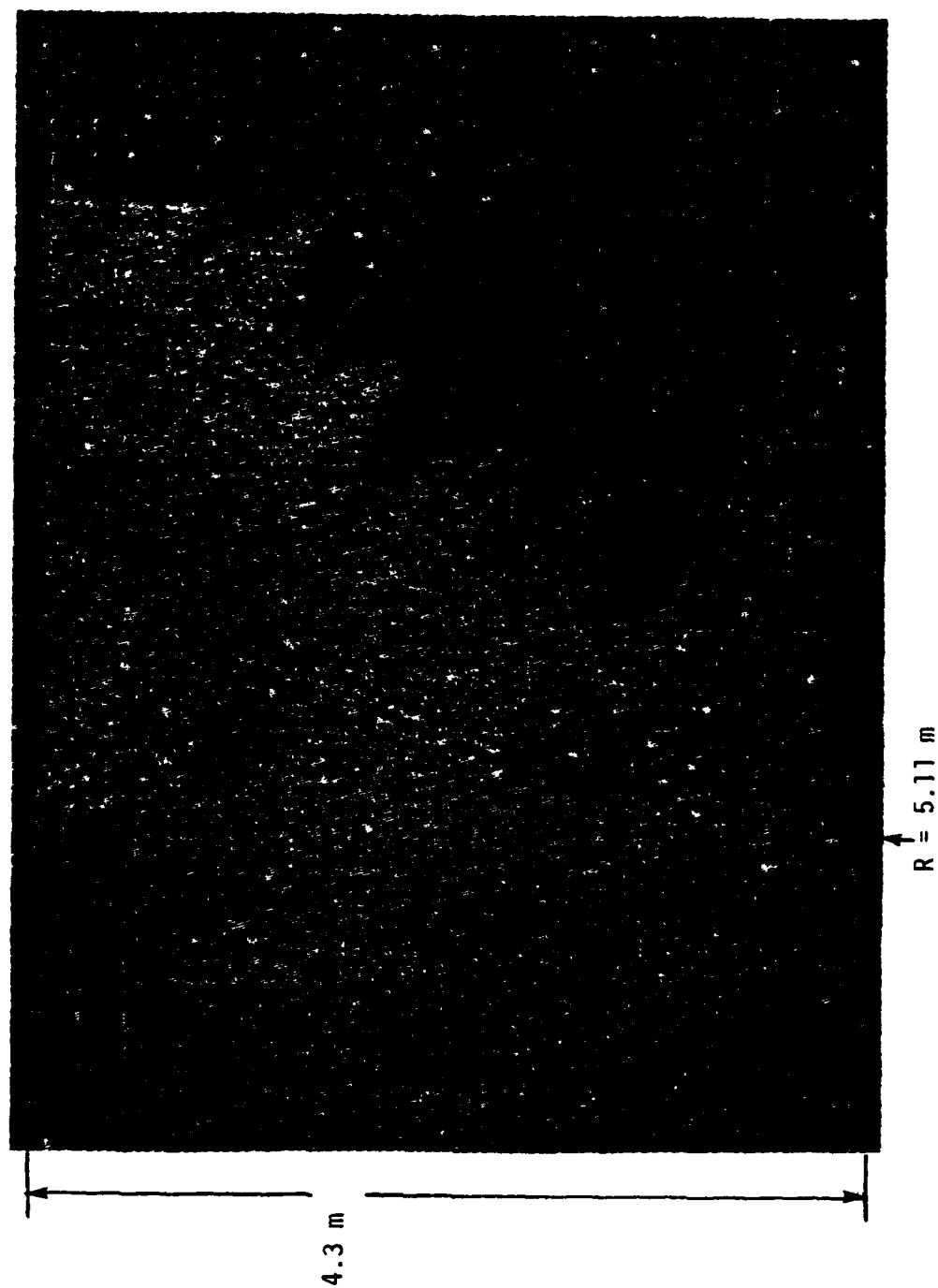Figure 35. Strobe/streak shadowgraph photograph taken during Test CD23.

4.3 m

R = 5.11 m

Figure 36. Strobe/streak shadowgraph photograph from Test CD25.
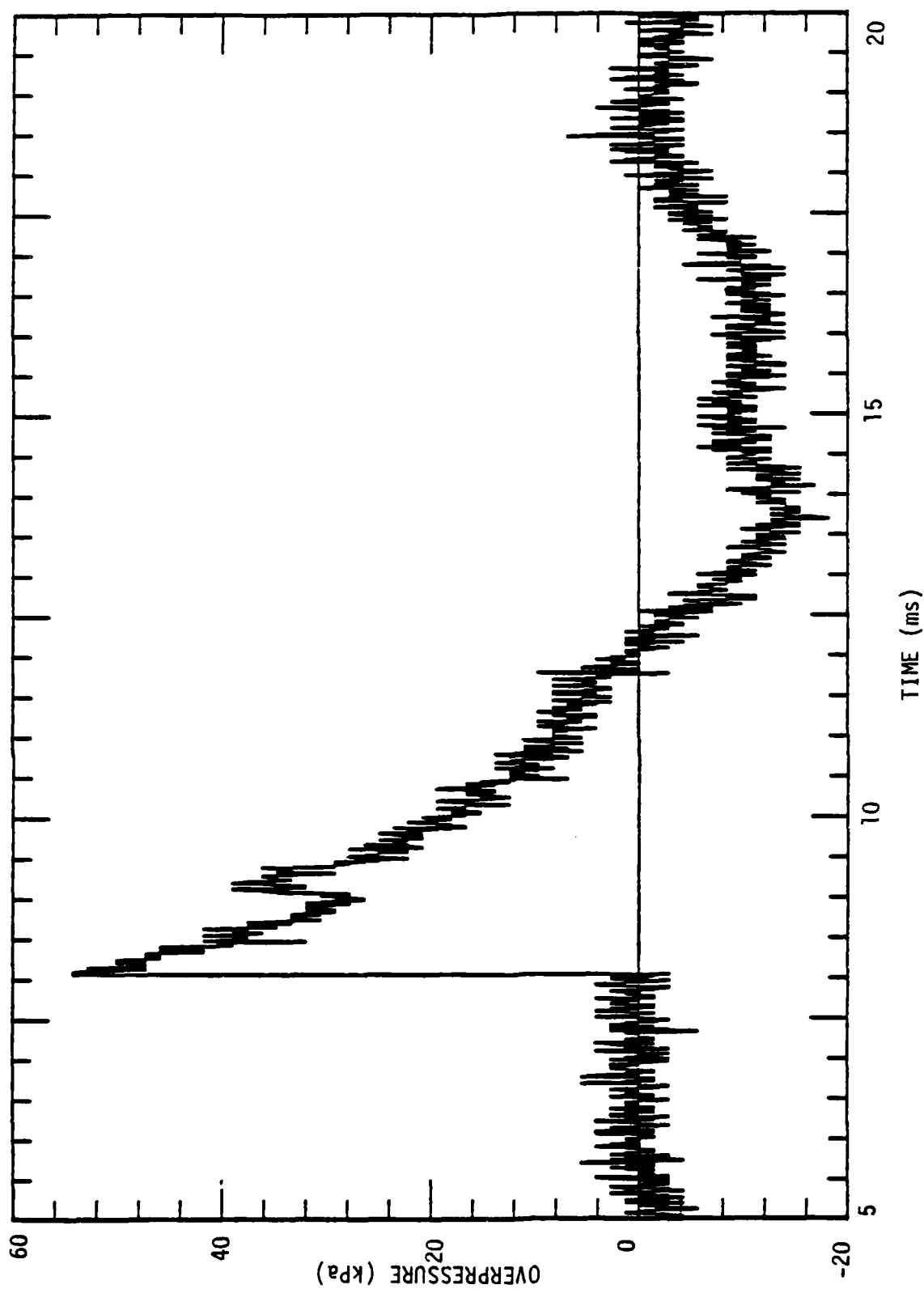
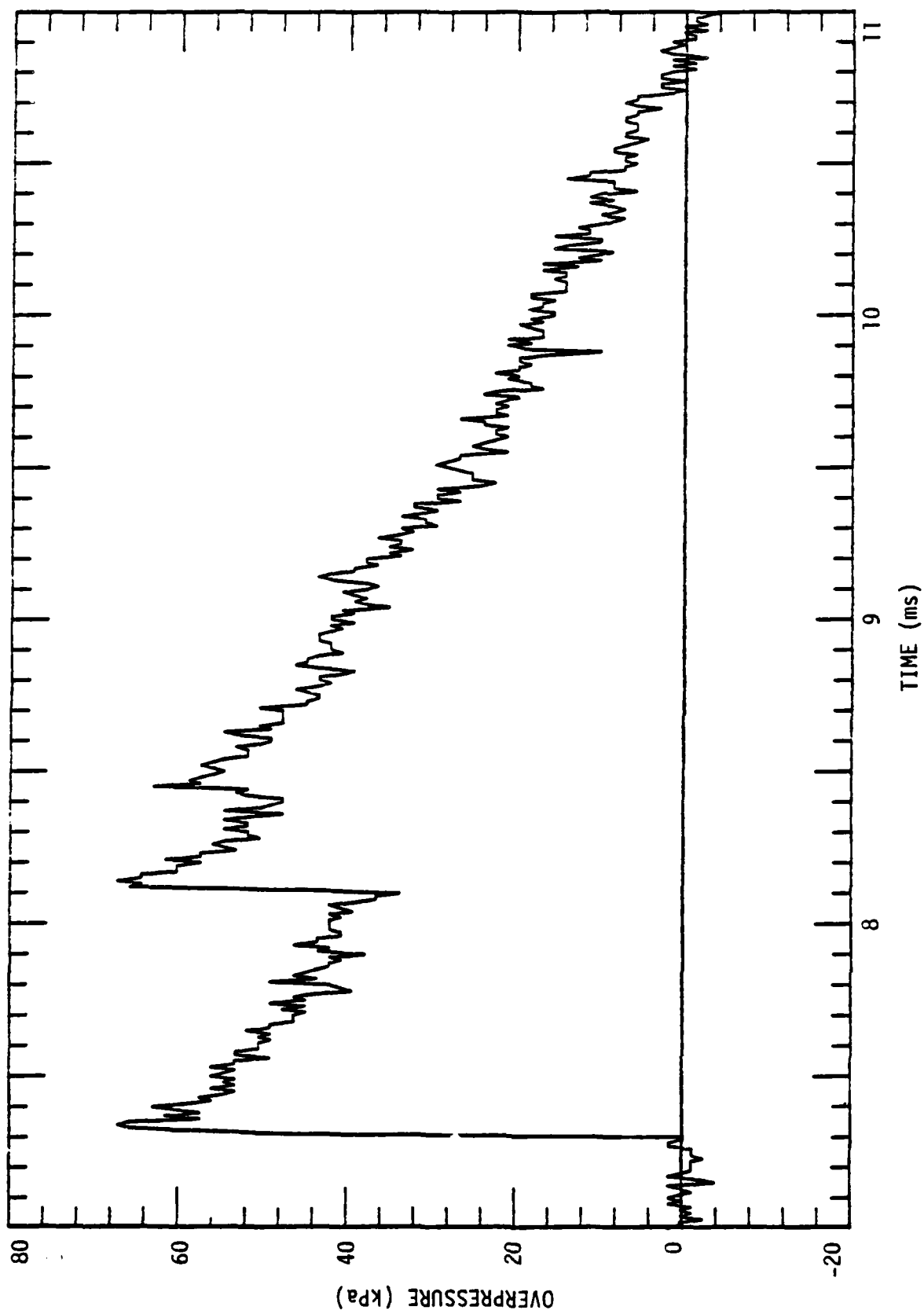Figure 37. Pressure record taken during Test CD25 at R = 4.13 m.

Figure 38. Pressure record taken during Test CD 23 at R = 4.13 m.

On Test CD25, with a global equivalence ratio of three, no shock-coupled combustion appeared on the films and the pressure decayed in an essentially monotonic manner. However, on the films and pressure records from CD23, in which the global fuel-air ratio was reduced to twice stoichiometric, a clear, shock-fronted secondary wave was observed. On Figure 35, the secondary wave can be seen just overtaking the cloud boundary. This wave correlates with the secondary front on Figure 38 (which was taken from approximately the same position).

On the remaining high-speed films from Test CD23, a shock-coupled reaction zone could be seen propagating behind the blastwave front. This reaction zone was assymetric. At early times it appeared on both sides of the cloud, as observed through the camera. It extended to the ground but was not visible on the top part of the cloud. Well before the blast front arrived at the cloud boundary, combustion on one side of the cloud had discontinued. Luminosity on the other side (which was in the direction of the pressure instrumentation line) continued until after the shock emerged from the cloud.

These two tests, CD23 and CD25, taken together, again appeared to indicate marginal initiation conditions. It is known that blastwaves are rapidly attenuated by sprays. In Test CD25, the blastwave apparently was attenuated to an extent that no shock-coupled reaction resulted outside the immediate vicinity of the initiator fireball. On Test CD23, however, with a reduced amount of fuel present in the cloud, the attenuation was not as severe.

It should be noted in addition that the dwell time in both these tests was short, leading to minimal pre-detonation droplet evaporation. By comparison, the spray loading was lower and the dwell time longer on Tests CD17B and CD17C. On those tests, using the same initiator as in tests CD23 and CD25, detonation initiation was (at least partially) achieved.
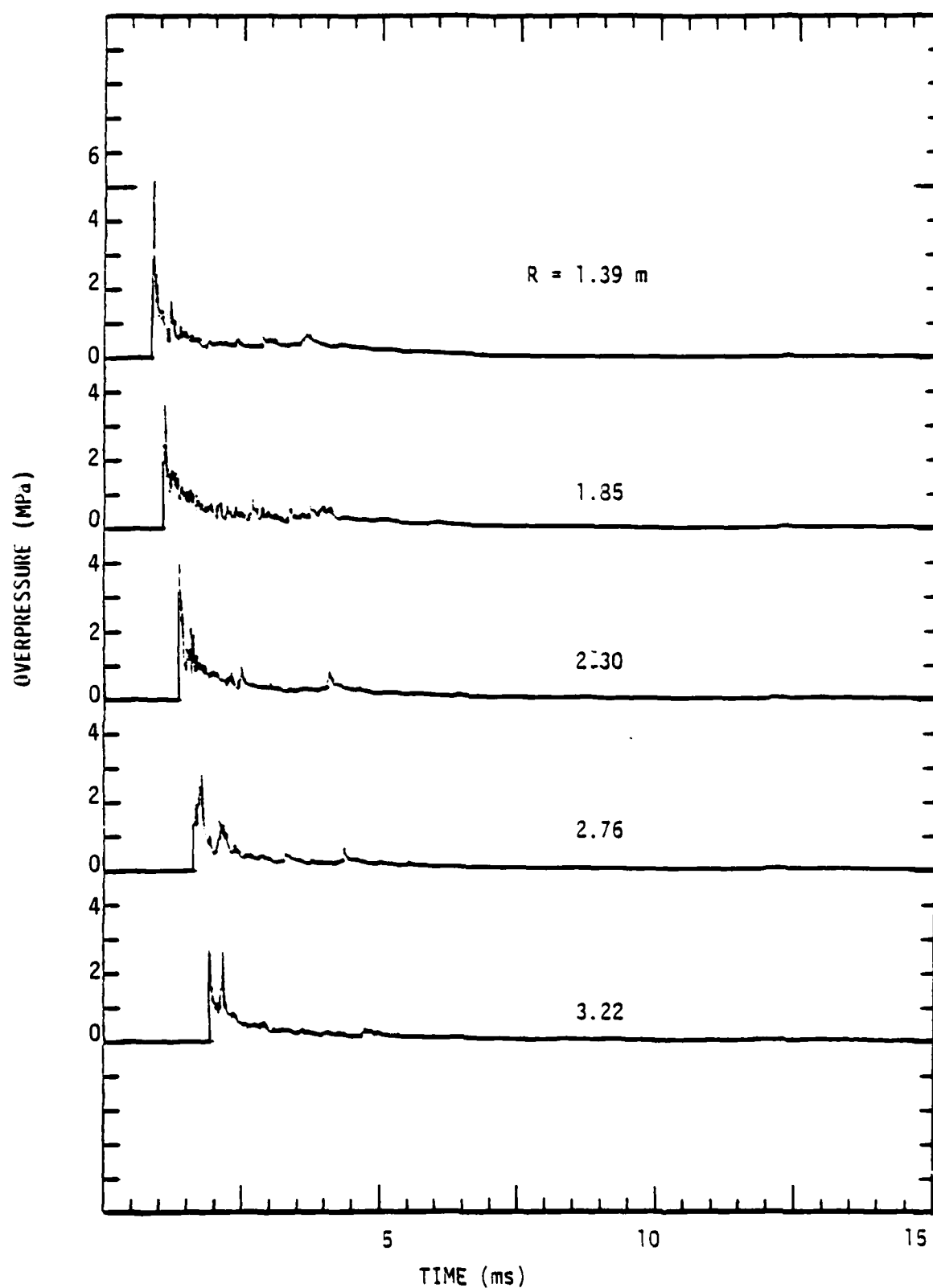
81

Figure 39. Pressure records taken during Test CD25, R = 1.39 m to 3.22 m.

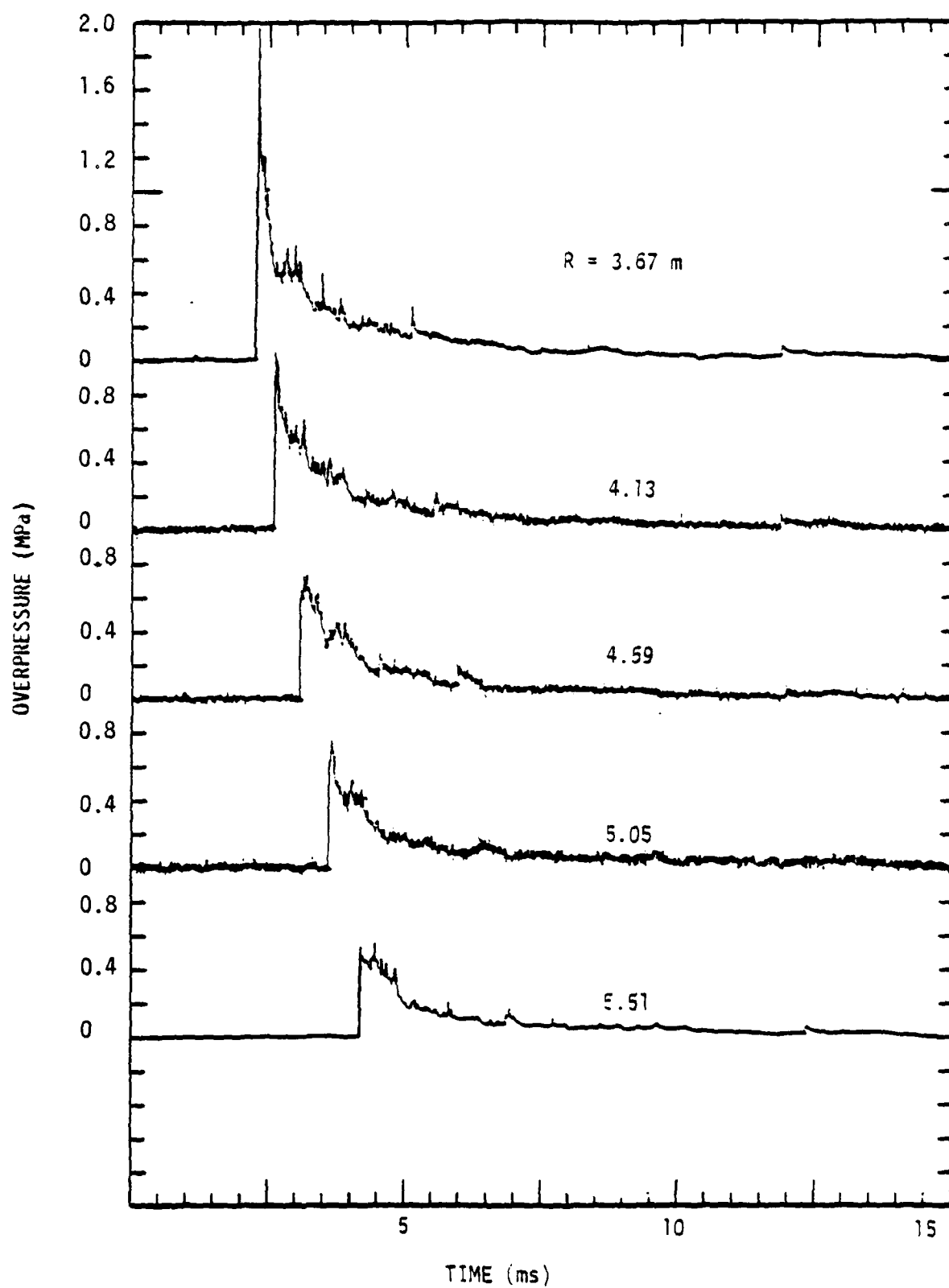Figure 40. Pressure records taken during Test CD29, R = 3.67 m to R = 5.51 m.
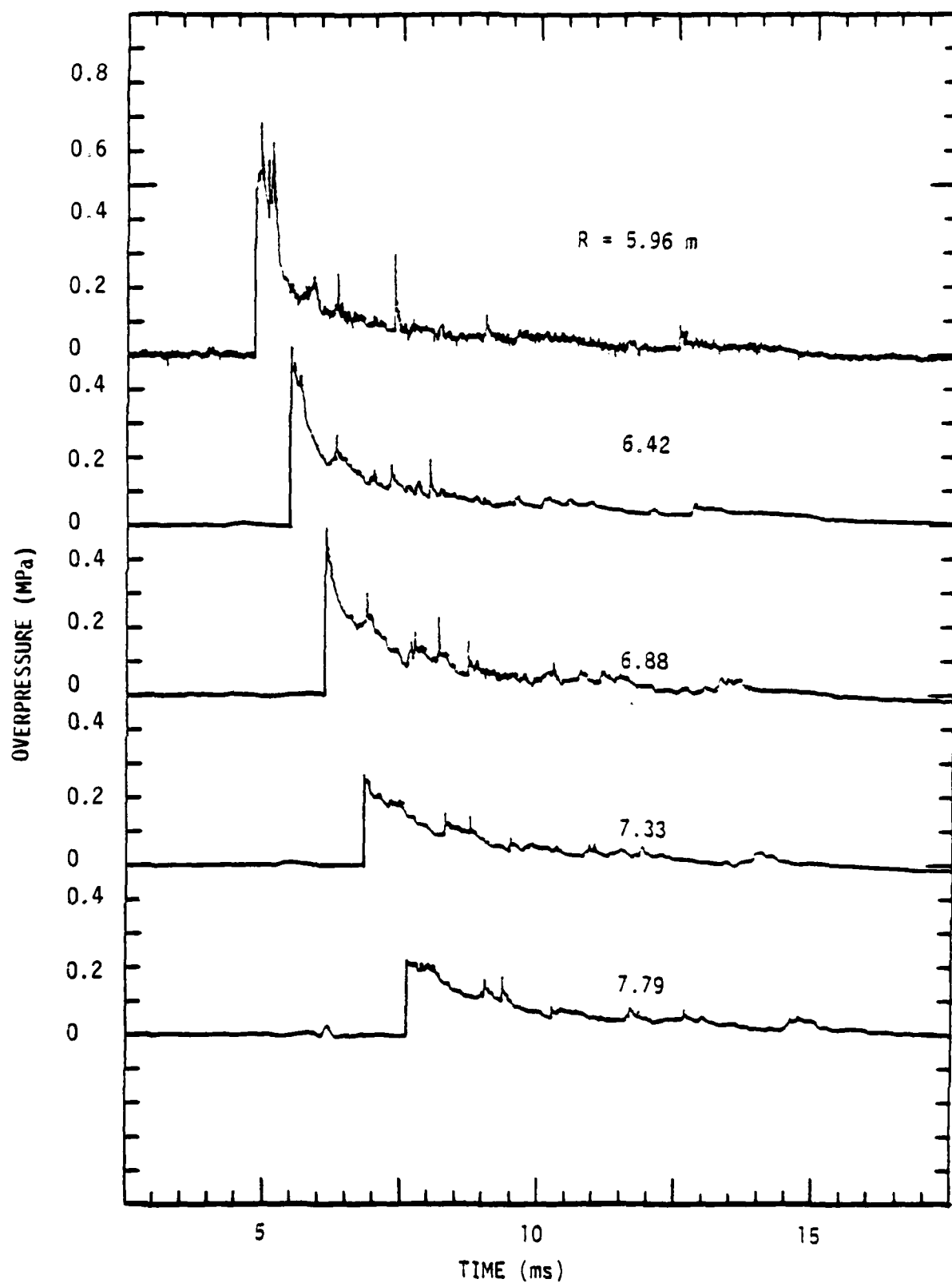
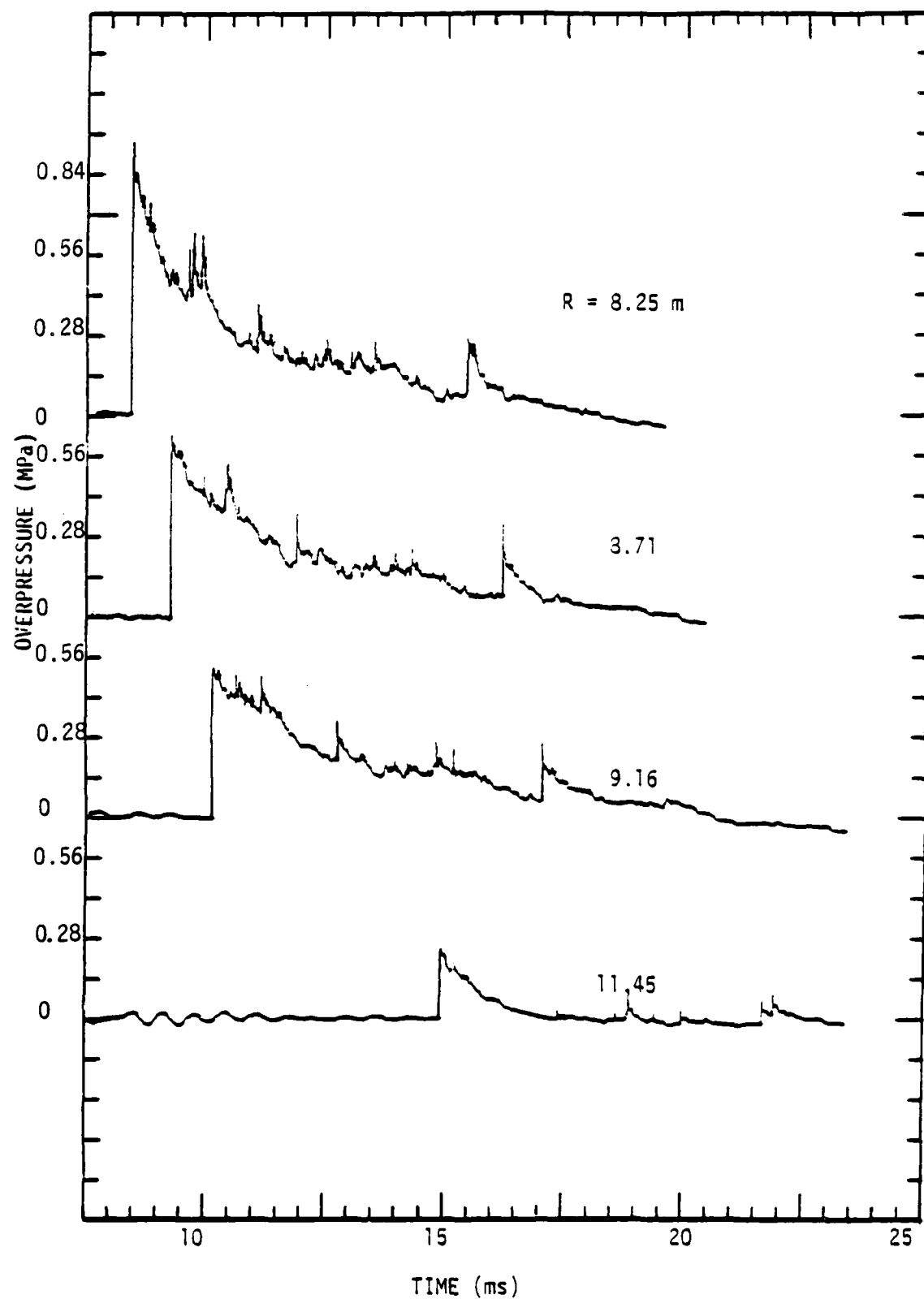Figure 41. Pressure records taken during Test CD29, R = 5.96 m
            to 7.79 m.

Figure 42.   Pressure records taken during Test CD29, R = 8.25 m
to R = 11.45 m.

4.5   Test CD29 (Initiator Location)

Resources permitted only one further test to follow CD23 and CD25. S-CUBED decided to conduct a test in which detonation initiation would be almost assured. The test selected was CD29 (Table 3), with somewhat modified test specifications (Table 4):   the initiator offset was reduced from 2.29 m (7.5 ft) to 1.07 m (3.5 ft), and the initiator mass increased from 50 gm to 950 gm.

The cloud on Test CD29 detonated. The set of nineteen primary pressure records appears on Figures 39–42. The records have been plotted on equal time bases to facilitate wave tracing. The furthest transducer was moved from 9.62 m (31.5 ft) to 11.5 m (37.7 ft) for this test, although that particular transducer appears to have been faulty. A three–dimensional plot of the data from CD29 is given on Figure 43.

In many respects, Test CD29 was very similar to Tests CD17B and CD17C. Times of arrival are plotted against range for all three of these tests on Figure 44. The average wave strengths and decay rates are closely comparable. Like Tests CD17B and CD17C, Test CD29 never attained the steady, normal stiuchiometric detonation speed of approximately 1800 m/s, in spite of the large initiator. The front velocity fell below the minimum possible detaontion speed (1520 m/s at the lean limit) beyond about 2.6 m (8.20 ft) radius, which is half the nominal cloud radius.

Figure 45 is a plot of the wave front velocity along the ground versus range. When the front reached the vicinity of the cloud boundary, its velocity was less than 70 percent of the normal (Chapman–Jouget) detonation speed. The wave-front velocity ocillations were not as severe as those in Tests CD17, particularly as compared with CD17C (Figure 19).

Figure 46 is a frame from the half-frame Hycam camera located in the south camera position, using infared film. Figure 47 is a strobe/streak shadowgraph of the blast front emerging from the

86
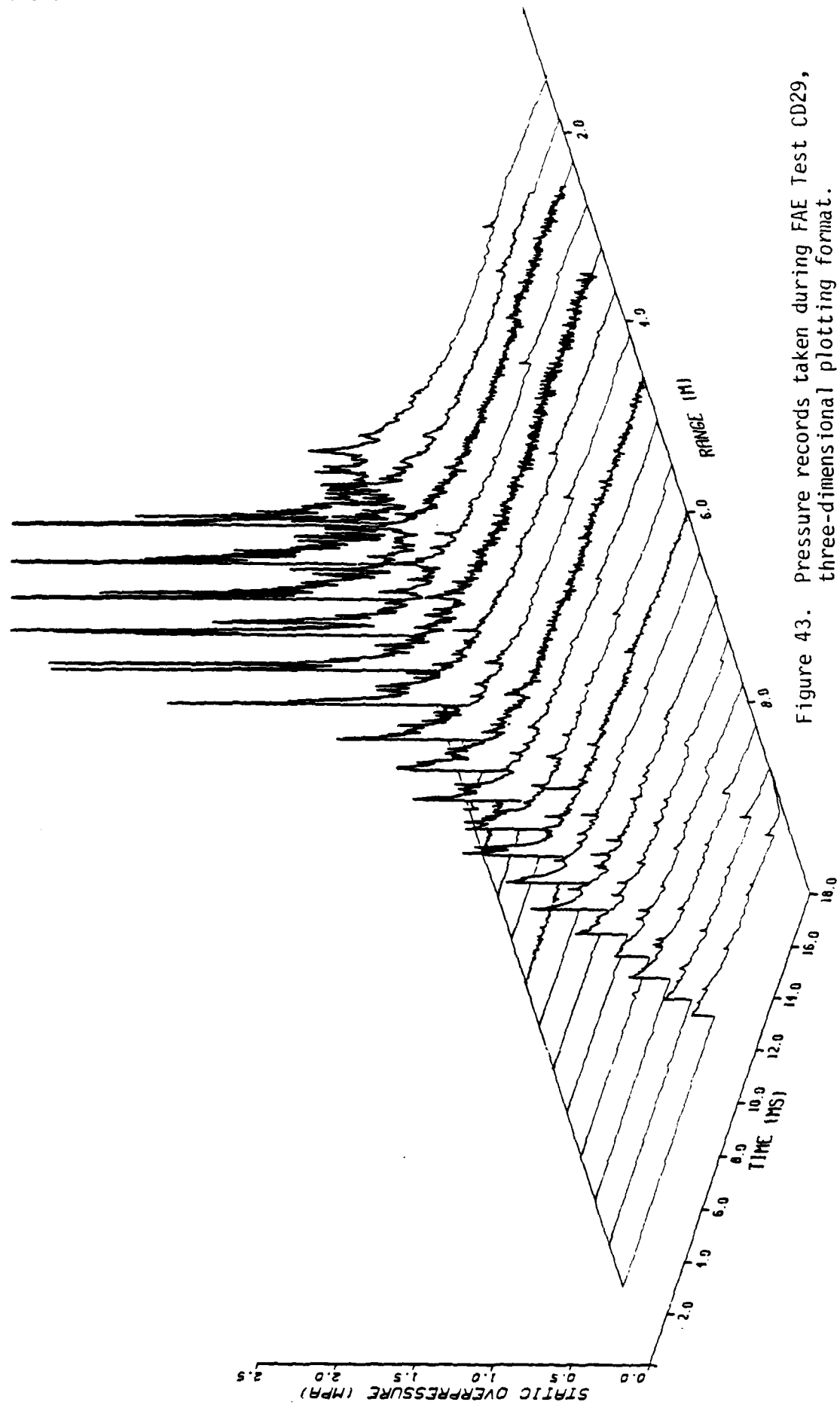
Figure 43. Pressure records taken during FAE Test CD29, three-dimensional plotting format.
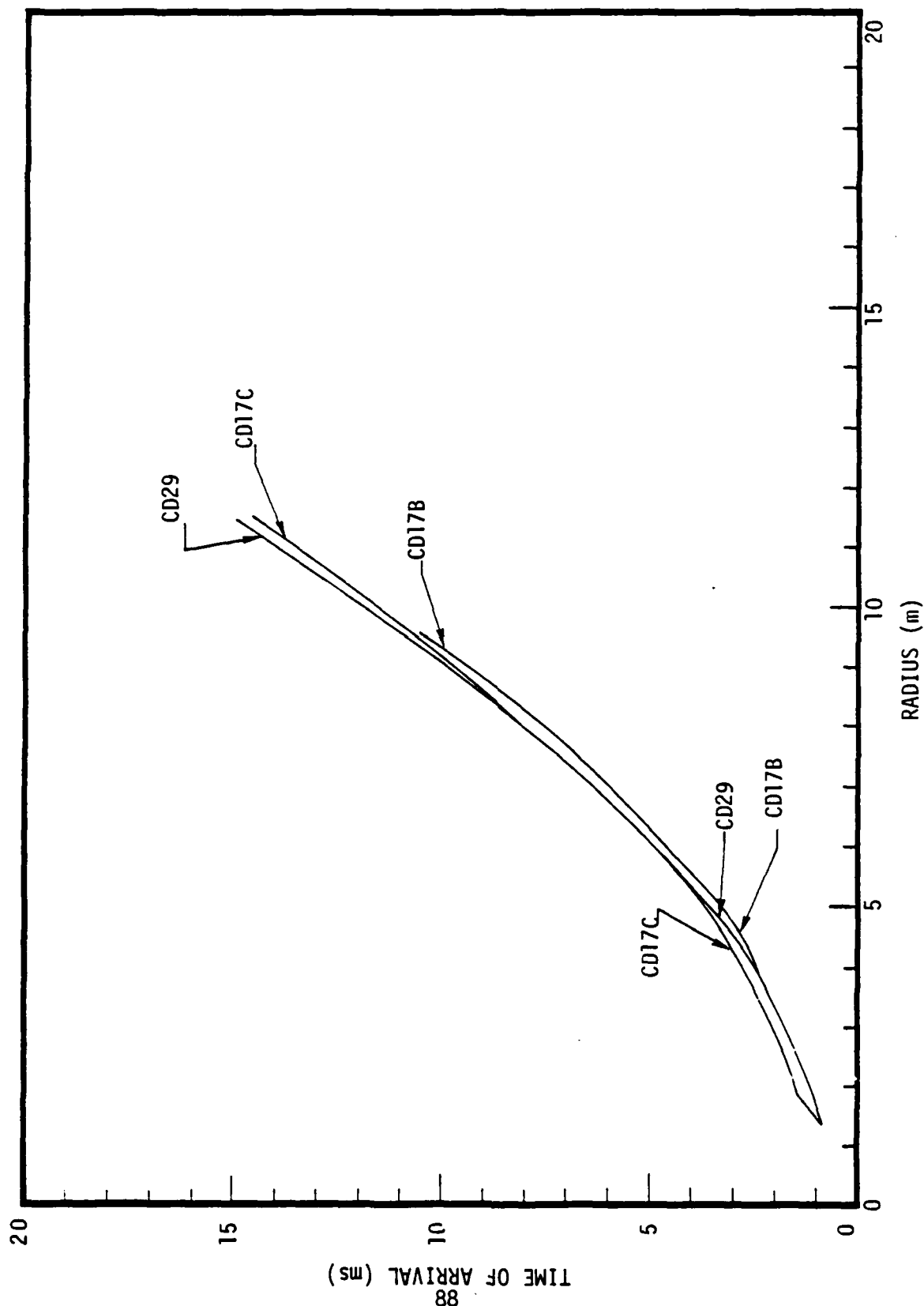
Figure 44. Time of arrival versus radius during Tests CD17B, CD17C, and CD29.
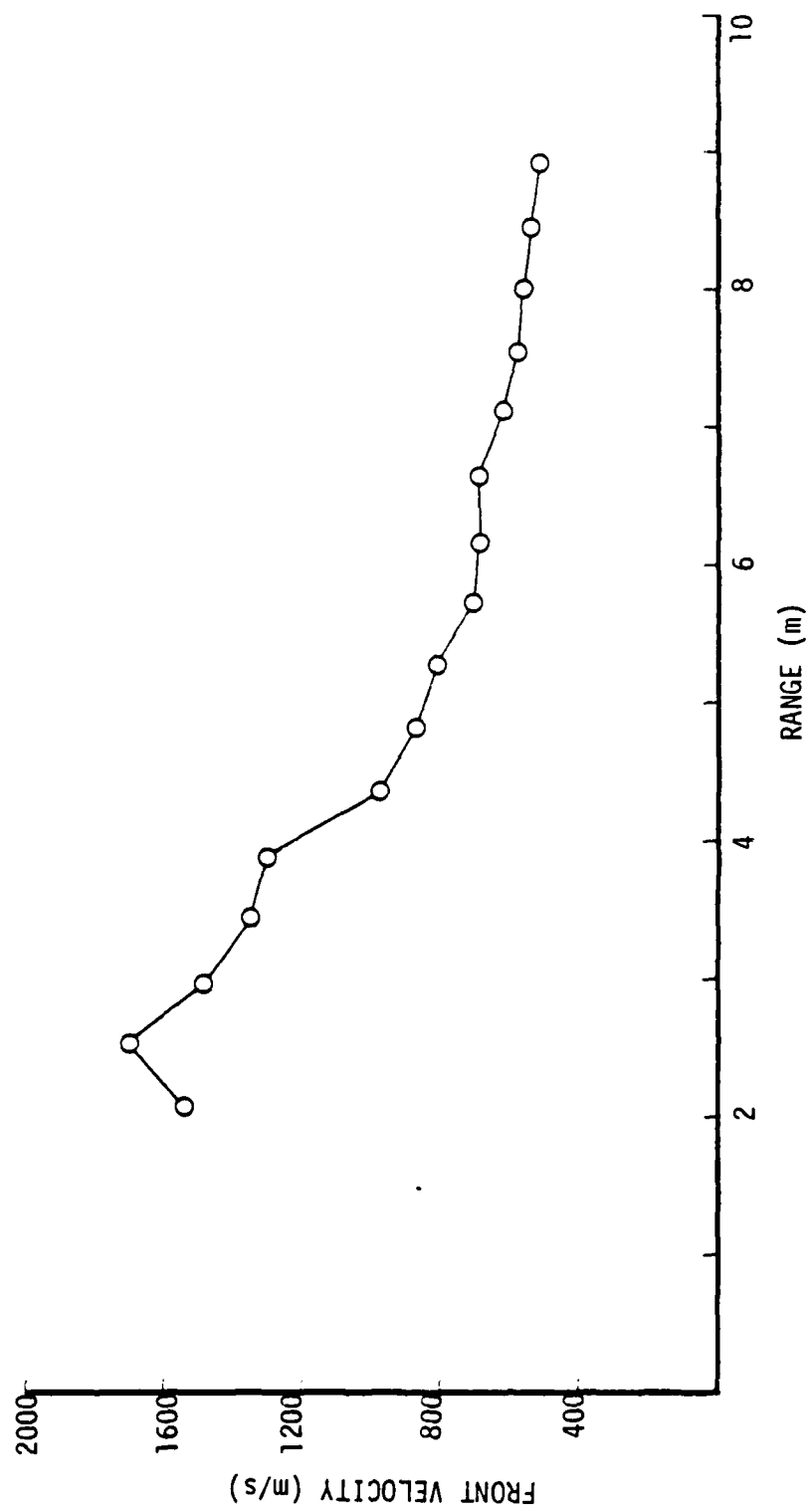
Figure 45. Wavefront velocity versus range for Test CD29, derived from time of arrival data.
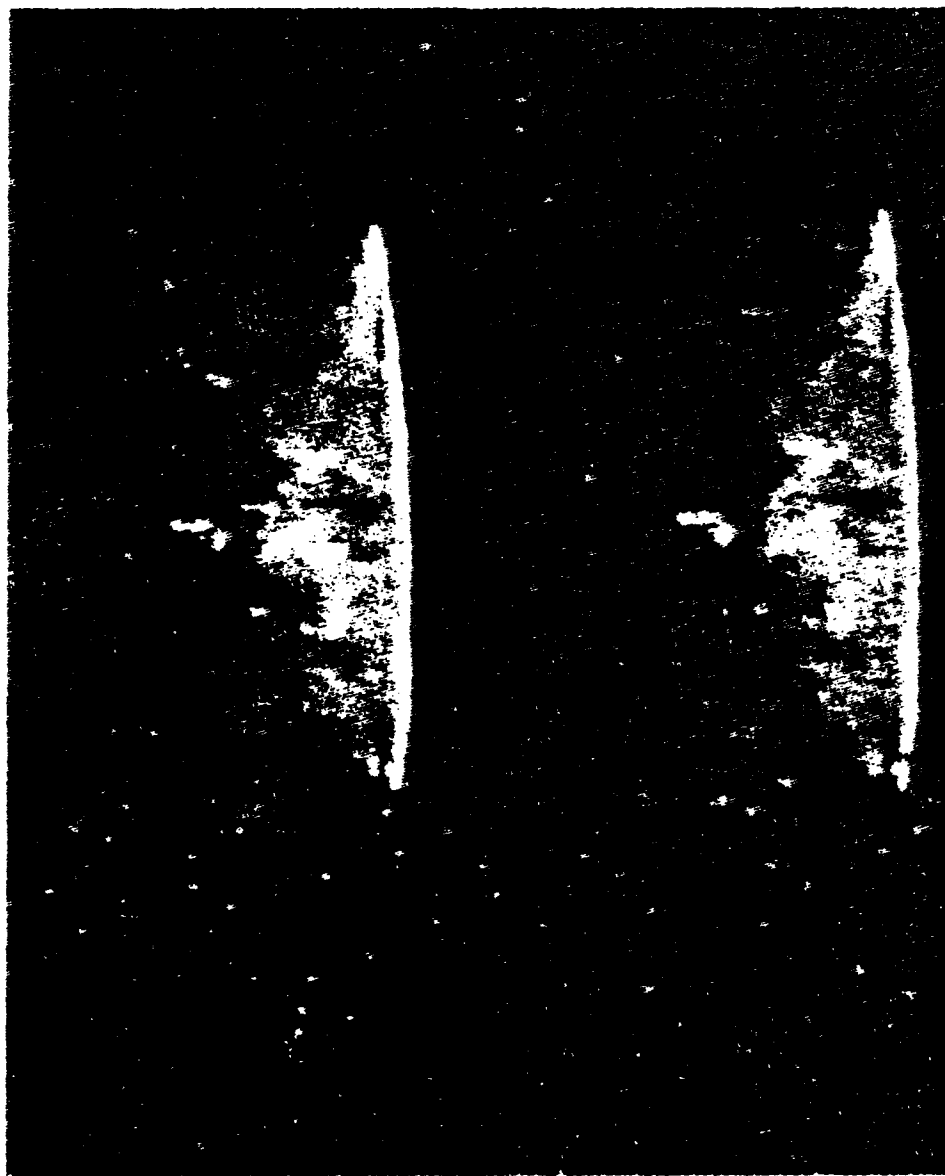
Figure 46. Split frame photograph from high-speed camera using infrared film, Test CD29.

90

R = 5.68 m

4.3 m

Figure 47. Strobe/streak shadowgraph photograph taken during Test CD29.

END

FILMED

DTIC
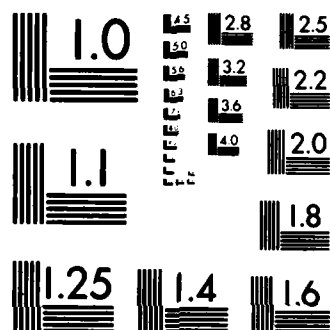
MICROCOPY RESOLUTION TEST CHART

NATIONAL BUREAU OF STANDARDS-1963-A

cloud. The detonation reflection is well defined on Figure 46. It appears as a region of increased luminosity extending across the entire cloud. The increased luminosity may be due simply to the additional compression of the detonation products, or it may be the result of secondary combustion behind the reflected detonation front. The reflection formed the Mach stem which is visible on Figure 47. A reflection of this kind had been observed on tests in previous FAE experiments in which ordinary (visible), high-speed film was used (Reference 3). However, this was the first time the reflection had been photographed as a Mach stem, by means of a shadowgraph technique.

The detonation front again appeared to be cellular. In particular, the large bulges on both sides of the cloud (Figure 46) were noted. As in Tests CD17, the reaction product luminosity was not uniform inside the cloud. Patches of varying intensity gave the exploded cloud a mottled appearance.

In the shadowgraph image on Figure 47, a number of waves can be seen extending to the ground. These are almost certainly responsible for some of the pressure excursions near the cloud boundary. The waves could be seen as they emerged from the exploded cloud, but their origins within the cloud could not be traced. None of the waves observed on these films was moving in a direction transverse to the front.

The pressure records (Figures 39–43) show several wave packets which originate within the cloud. One of these waves can be seen interacting with the leading shock at $R = 3.67$ m and another at $R = 6.42$ m. Additional wave packets can be traced on the three dimensional plots which did not overtake the lead shock in the time period plotted. One of the clearest among these waves originates near $R \sim 4$–4.5 m and $t \sim 11$ ms and consists of components which move inward toward the explosion center and outward toward the leading shock. This particular wave could be due to an interface reflection or due to a secondary volumetric explosion near the cloud boundary.

On the pressure record at R = 9.16 m it appears at about 17 ms. On this record the magnitude of this wave has become of some significance. This increased significance is not due to an increase in incremental overpressure but rather to the diminution of the leading shock strength. The incremental overpressure of this secondary wave remained between 60-80 kPa (9-12 psi). On the record at R = 9.16 m, it represented a shock strength of Mach 1.21; the leading shock at that range had a strength of Mach 1.44.

5. DISCUSSION AND CONCLUSIONS

5.1 Summary of Findings

In its present configuration, the FAE simulator represents a technique for generating free-field airblasts inexpensively and at a high repetition rate, but with limitations as discussed below. The facility that was developed in conjunction with this project is capable of generating airblasts in the overpressure range below 0.7 MPa (100 psi), at the 1/4-ton nuclear equivalence level. The extent to which the FAE simulator could be scaled to larger sizes is still uncertain, but it is felt that it may be possible to achieve free-field simulations at the 1-2 KT level.

The quality of simulation attained with the FAE system in the present configuration has been variable. Direct comparisons of scaled FAE airblasts with nuclear curvefits (References 1 and 2) are thought to be favorable with respect to peak overpressure, overpressure-impulse, and positive phase duration.

In many of the tests, however, anomolous secondary waves were present. The secondary waves have appeared mainly in the 0.07-0.7 MPa (10-100 psi) range. While some progress was made on the present investigation in probing for the causes of these waves, their origins were not isolated. Without further development, therefore, it is suggested that the FAE simulator be used in applications for which the waveform smoothness is not highly critical, or in the far field below about 0.07 MPa (10 psi).

The following list summarizes the observations made during the investigations reported herein:

a. All of the tests appeared to be underinitiated or marginally initiated. Steady Chapman-Jouget detonation speeds were not achieved within the clouds in any of the experiments. Shock supported supersonic combustion was observed in three tests, CD17B, CD17C, and CD29. In

94

these cases, the front velocity appeared to oscillate within the cloud, but the average front speed steadily decreased, and fell below minimum detonation levels, well before reaching the cloud boundaries. In addition, identical clouds were initiated on Tests CD17B and CD17C with a 200 gm HE charge at 0.32 m (1.04 ft) height, but initiation was not successful on CD18 in an identical cloud with a 50 gm charge at 0.192 m (0.63 ft). These results also indicate marginal initiation conditions.

b. There appeared to be considerable fuel distribution nonuniformities within the clouds, on both small and large scales. The cloud shapes were not hemispherical in any of the tests. Rather, they were lifted above ground around the lower periphery, and flattened or dished inward on top. The clouds appeared to be approximately symmetrical rotationally about the vertical axis. This geometry distorted the detonation front near the cloud boundaries, most noticeably producing large, above-ground wave blisters. These blisters seemed to heal very quickly once the wave was entirely outside the cloud. The remainder of the detonation front appeared to be cellular on smaller scales. Local pockets of residual fuel and air appeared to ignite at late times. This gave the clouds a nonuniform, mottled or glittering appearance when viewed by high-speed infared cine photography.

c. Several secondary waves, rather than just one, were produced by each of the three detonation tests. Most of these waves could be traced to the cloud interior, but their origins were not clear. One wave appeared to originate at the cloud boundary, with inward- and outward-moving components.

95

d.   The majority of the secondary wave packets were of low incremental impulse. On only one test was the incremental overpressure and impulse of a secondary wave judged to be significant with respect to the primary wave overpressure and impulse. On that test, CD23, detonation was not initiated but some combustion was observed behind the initiator shock.

e.   A Mach reflection was observed on Test CD29, but it was not in the photographic field of view on Tests CD17B and CD17C. This difference is attributed to the greater initiator height (effective height-of-burst) and the concomitant greater integrated detonation energy prior to reflection on Test CD29.

f.   An increase in initiator mass by nearly a factor of five, accompanied by a significant initiator height increase, did not significantly alter the qualitative or quantitative character of the FAE-produced blastwave along the ground.

g.   Secondary wave motions transverse to the leading shock were not observed, with the exception of the Mach reflection.

h.   Cloud initiation was attained using a 200 gm H.E. charge in clouds with a global equivalence ratio of one and a dwell time of 430-450 ms. Initiation with a 200 gm charge was not successful in clouds with global equivalence ratios of 2 and 3 and dwell times of 113 and 63 ms, respectively.

i.   Shadowgraph photography was useful for examining shock structures outside the cloud, but the origins of these structures within the cloud were obscured by the cloud itself. Infared photography was useful for observing hot pockets within the cloud.

5.2 Conclusions

On the basis of these observations, it was concluded that:

a. The required minimum initiator strength increases when the spray density in the vicinity of the initiator is increased and/or the amount of fuel in the vapor phase is decreased.

b. The initiator should be located as closely as possible to the ground to minimize the strength of the reflected cloud detonation.

c. Fuel and cloud shape nonuniformities contribute to blastwave irregularities in the immediate vicinity of the cloud boundaries.

d. Marginal detonation initiation may be accompanied by shock front speed oscillations within the cloud. This is a possible source of some of the secondary waves.

5.3 Recommendations

The following recommendations are based on the preceding observations and conclusions in addition to prior experience with the FAE simulator.

a. The fuel dispensing technique should be modified to enable more control over cloud shape and fuel distribution. One possible approach would be to abandon the central nozzle cluster configuration. Instead, nozzles distributed over a larger part of the ground area under the cloud could be used. The benefits from this configuration are (1) not all nozzles would need to spray fuel to a distance equal to the cloud radius; (2) the high explosive initiator could be located on the ground in the exact center of the cloud; (3) a group of secondary nozzles could inject a highly volatile primer fuel in the vicinity of the initiator charge to increase the

97

detonable sensitivity of the cloud; (4) the nozzles could
be oriented in directions other than vertical, to coun-
teract large-scale air movements which tend to distort
the clouds and to enhance mixing.

If the central nozzle cluster design concept is retained, then
it is recommended that the design be changed so that the distri-
butions in the number density of nozzles, the nozzle diameters, and
the dispensing pressure can be varied within the cluster. Not all
nozzles need necessarily to be aimed in radial directions.

b. The high-explosive initiator needs to be of adequate
size. The minimum size must be determined empirically.
If it is objectionably large, then it can be reduced by
introducing fuel vapor in the initiator vicinity, either
by allowing more cloud pre-ignition dwell time, or by
separately injecting additional vapor.

c. A direct comparison of the FAE simulator with raw
nuclear airblast data would be useful for assessing the
degree of waveform comp_tibility at various pressure
levels.

REFERENCES

1.   Sedgwick, R. T., Kratz, H. B., and Herrmann, R. G., "Feasibility Investigation of a Permanent Fuel-Air Explosive Blast Simulator", DNA 5059T, 9 August, 1978.

2.   Pierce, T. H. and Sedgwick, R. T., "Fuel-Air Explosive Simulation of Far-Field Nuclear Airblasts", DNA 5280, December, 1979.

3.   Pierce, T. H., Sedgwick, R. T., and Groethe, M. A., "Investigation of a Reusable Fuel-Air Explosive Nuclear Airblast Simulator", DNA Draft Final Report, March, 1981.

4.   Gabrijel, Z. M., "Blastwave Initiated Heterogeneous and Gaseous Detonation Waves", Ph.D. Thesis, University of Michigan, Ann Arbor, 1978.

99

APPENDIX
FAE TEST CT-1

Due to the large number of revisions which were made in the FAE test apparatus, a preliminary experiment was conducted to verify proper functioning of all components. In addition, this test was utilized to compare the performance of the transducer mounting arrangement used in the 0° and 90° instrumentation legs with that of the newly-constructed 45° instrumentation leg.

The transducer mounts on the 0° and 90° legs consist of steel plates 15.2 cm x 61 cm x 1.9 cm (6 ins x 24 ins 2 3/4 ins). Transducers are installed on these plates in Delrin inserts which are epoxied into the plates. The mounting plates are installed, with six screws, on angle iron supports embedded in the concrete instrumentation leg above individual recesses. The top surface of the plate is flush with the concrete. Details of this mounting arrangement are given in Reference 2.

The transducer mounting blocks used with the 45° instrumentation leg are described in Section 2.1 of this report. The blocks are 15.2 x 15.2 x 6.4 cm (6 x 6 x 2.5 ins.). The blocks are made of steel and are fastened with two screws each on a supporting shoulder of the continuous instrumentation trough.

A schedule of transducer positions for FAE test CT-1 is given on Figure A-1. Positions are designated by a number in which the first two digits represent the azimuthal angle of the instrumentation leg on which the transducer is mounted; the remaining digits represent the actual radial distance (in meters) from the center of the test pad. The symbol A designates an active transducer, and the symbol D designates a dummy gage.

Active and dummy transducers were located on the three instrumentation legs at a range of approximately 6 m. Each dummy gage was mounted in a blind hole machined as closely as practical to the active gage on the same mounting plate. In addition to the active/dummy gage pair at the 6 m position on the 45° leg, two pairs of active gages were placed at adjoining mounting plate positions as indicated in Figure A-1. These active gage pairs included PCB,

101

Transducer			
Position	Type[1]	Serial Number	Range (psi)
A9005.92	P1	1658	500
D9005.92	P1	1662	500
A4505.96	P1	2186	500
D4505.96	P1	1659	500
A0006.03	P1	1655	500
D0006.03	P1	1657	500
A4506.12	P1	2188	500
A4506.12	K1	3-11	2000
A4506.27	P1	2656	500
A4506.27	K2	A-30	1000

Note: 1. Transducer Designations

K1: Kulite Model HKS
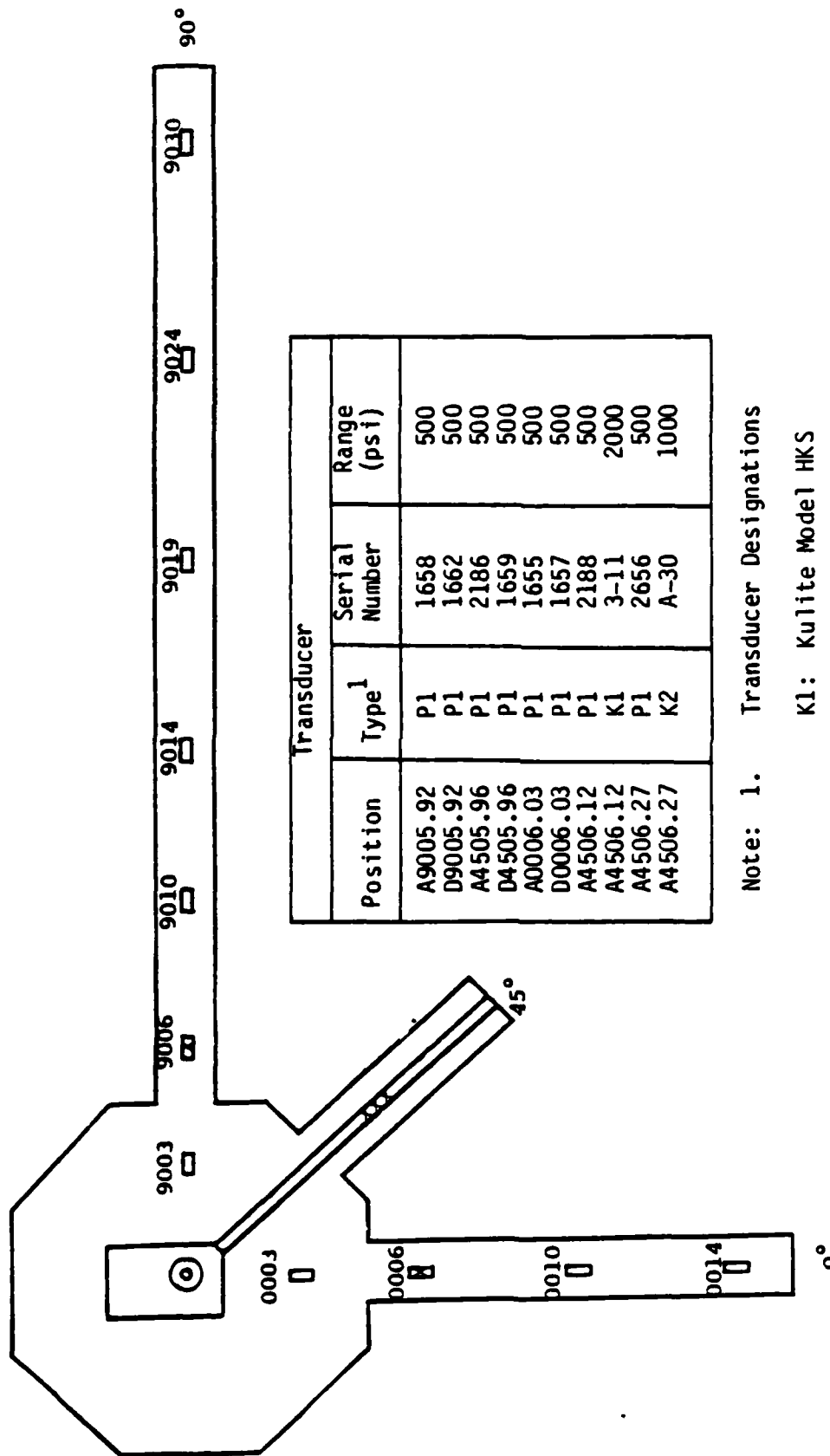
K2: Kulite Model XTS-190

P1: PCB Model 102M58

Figure A1. Schedule of transducer locations for Test CT1. Location numbers alongside fixed instrumentation troughs are nominal.

102

Kulite HKS, and Kulite XTS transducers. The specific pairings were chosen to enable performance comparisons between the three transducer types.

Test CT-1 was conducted using 7 gallons of propylene oxide in conjunction with the 600-hole dome nozzle head, which generates nominally 15-foot radius fuel-air clouds. The cloud formation time was approximately 600 ms. The initiator was a 350 gm sphere of C-4 explosive mounted 15.5 in. above the top surface of the dome nozzle head on a 1/4-inch threaded brass rod. At the time of the test, there was absolutely no wind whatsoever. No unusual problems were encountered during execution of this test.

The output from the active/dummy transducer pairs located at the (nominal) 6 m position on the 0°, 45° and 90° legs, is shown on Figures A-2 to A-4. The six transducers at these positions had been chosen so as to match acceleration response as closely as possible. Output from the dummy gages is presented on Figure A-2 through A-4 as a virtual pressure. The dummy gages responded to mounting plate motions on all three instrumentation legs. However, on the 45° leg, the duration of the acceleration-induced output was much shorter than that on the 0° and 90° legs.

A baseline shift occurred in the output from the dummy transducer on the 45° leg. This was not thought to be an electronics problem. A very small diameter vent hole had been machined into the transducer mounting block to relieve pressure introduced into the void space above the dummy transducer face during the installation of the transducer into the blind hole. It was thought that this void space slowly pressurized and depressurized during the experiment, causing an apparent baseline shift.

The output from the active transducers at the 6m position in the three legs are compared on Figures A-5 and A-6. On Figure A-5, the traces are plotted in real time during the test (measured from
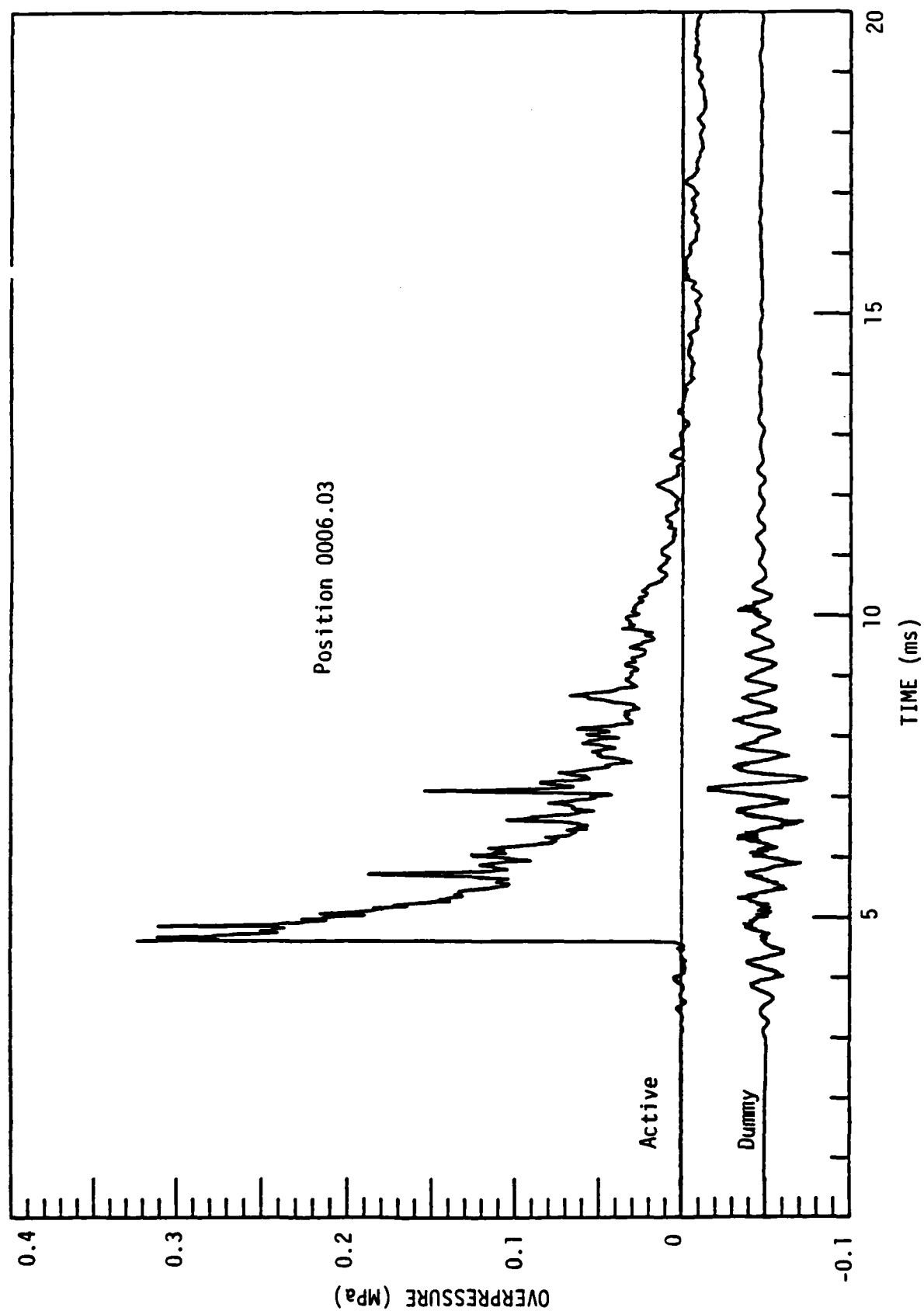
103

Figure A2. Active and dummy gage records at R = 6.03 m, 0° leg.

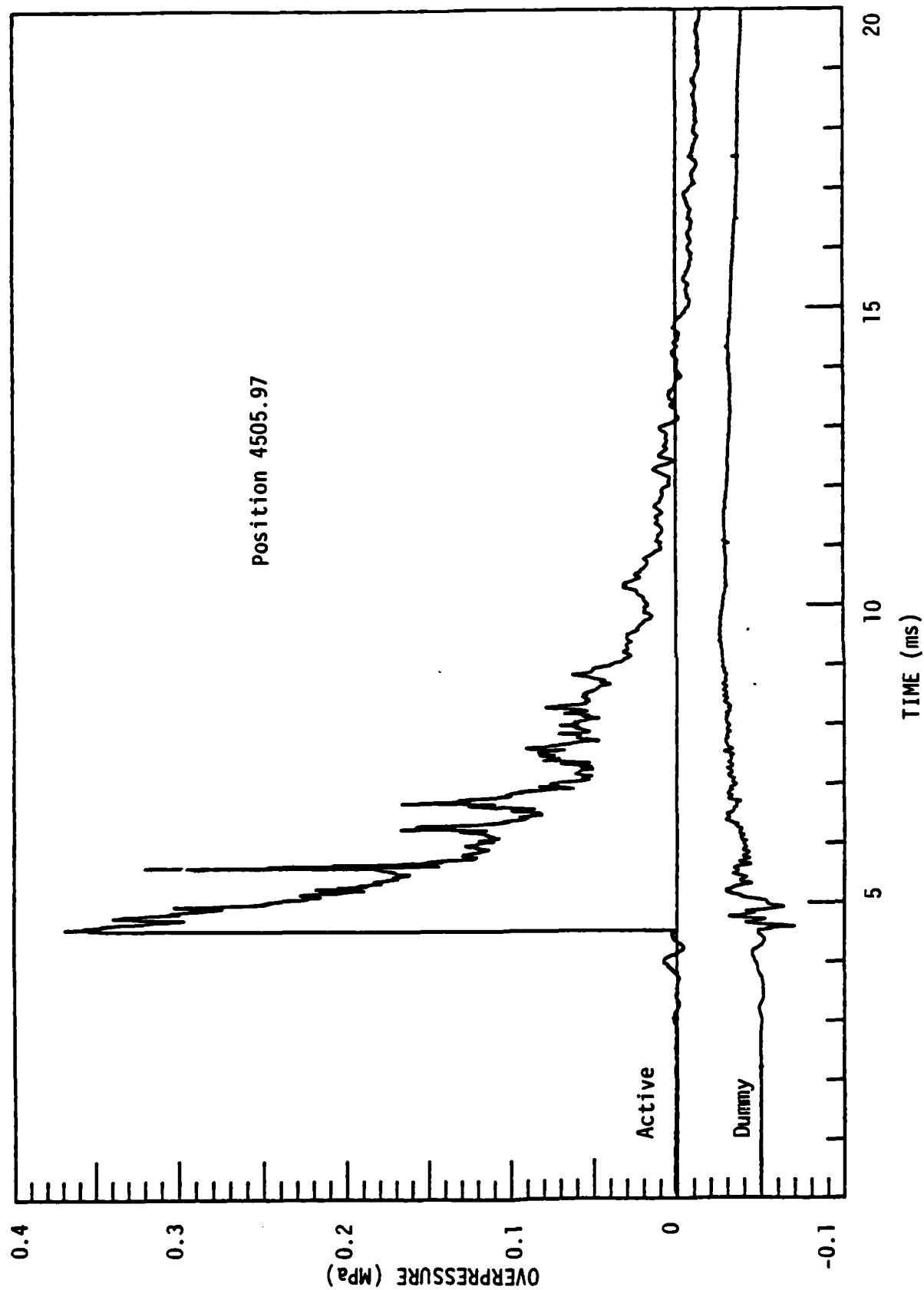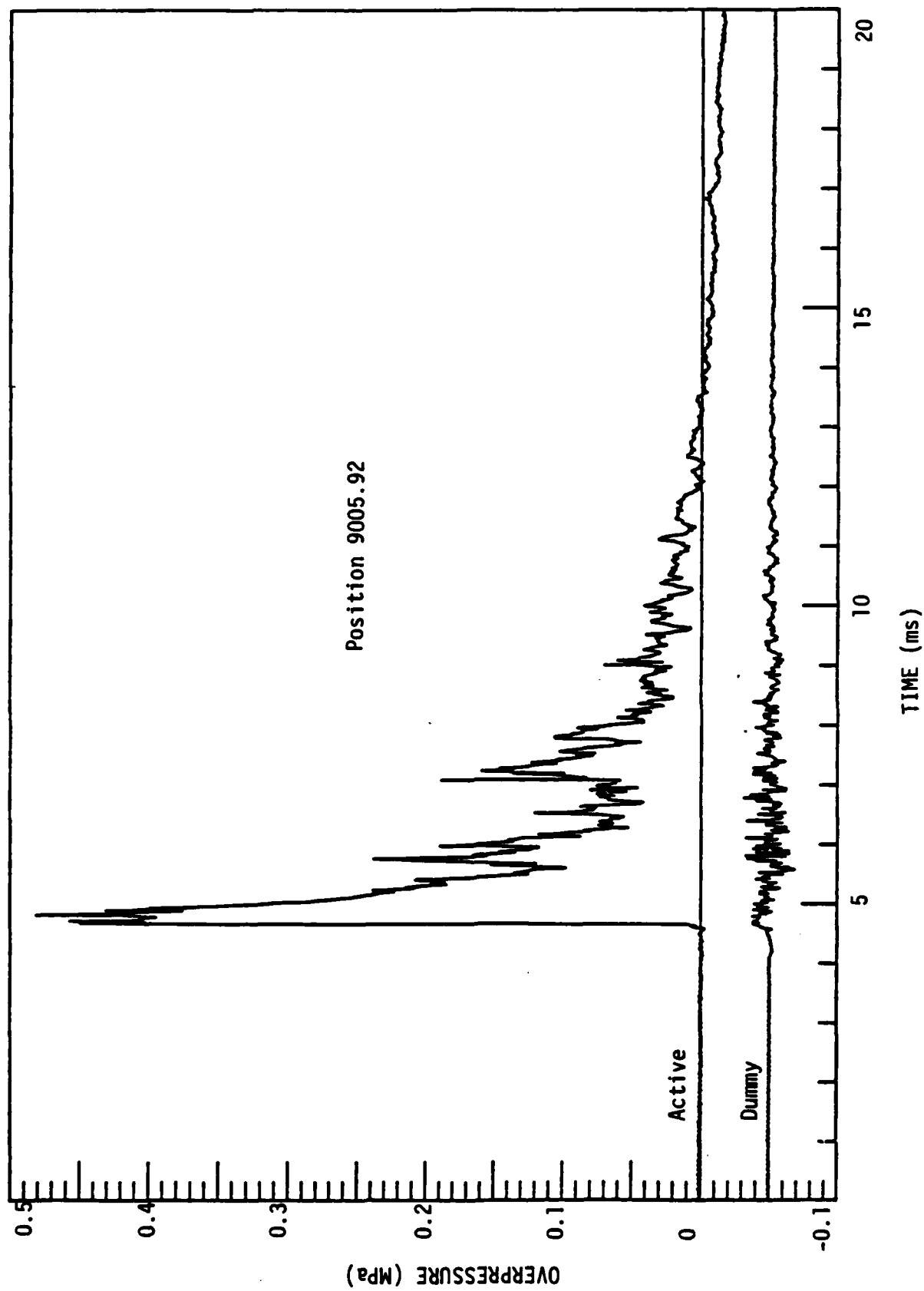Figure A3. Active and dummy gage records at R = 5.97 m, 45° leg.

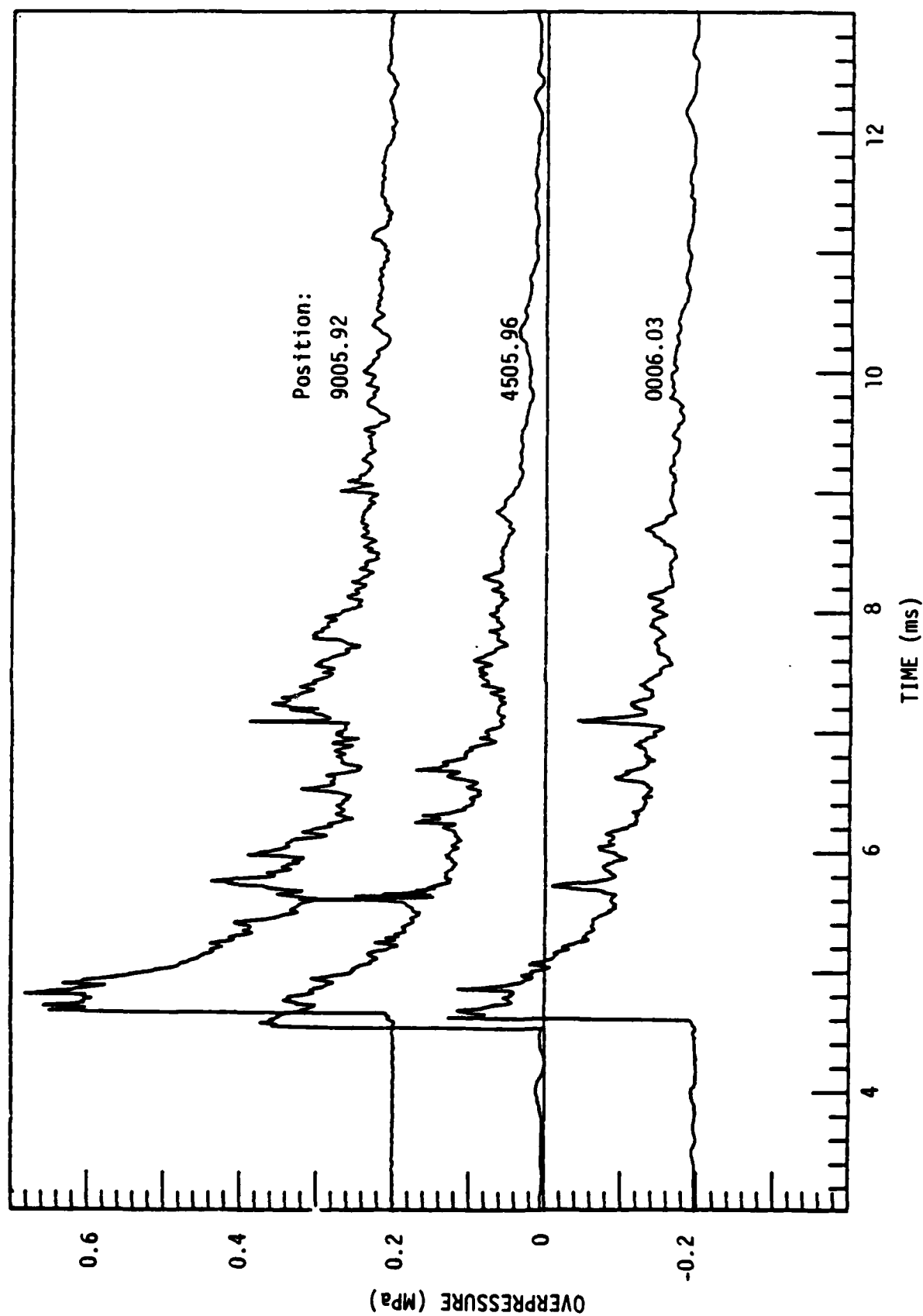Figure A4. Active and dummy gage records, R = 5.92 m, 90° leg.

106

Figure A5. Pressure records in real time (after H.E. initiation) R = 5.96 m, 45° leg;
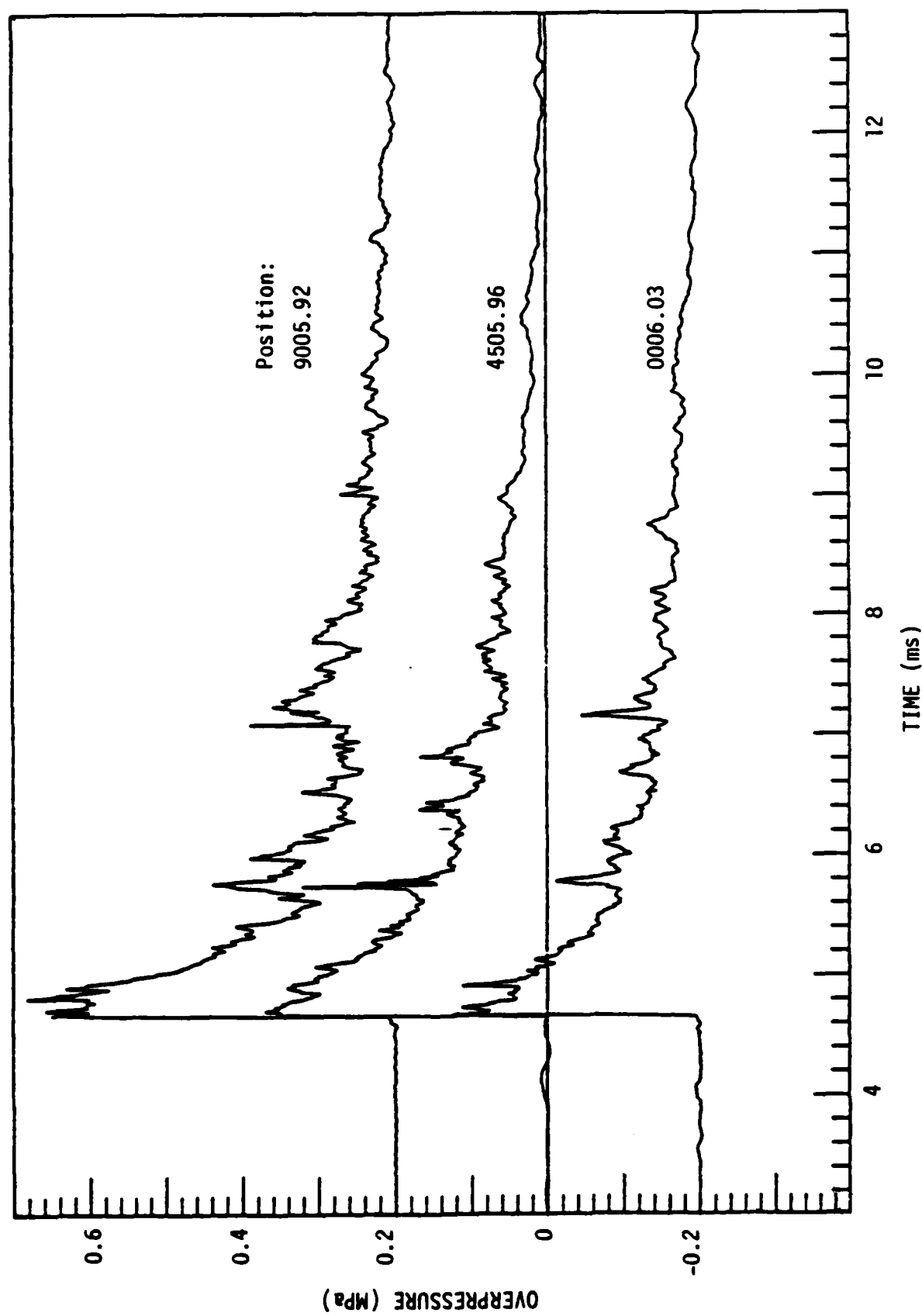R = 6.03 m, 0° leg.

107

Figure A6.   Pressure records at R = 5.92 m, 90° leg; R = 5.96 m, 45° leg; and R = 6.03 m, 0° leg.   Shock fronts have been aligned artificially.

108

H.E. initiation), while on Figure A-6, times of arrival have been artificially adjusted to align the shock fronts. Peak pressures on the three records were within ± 8 percent of 55 psi, and the traces are qualitatively similar.

Pressure records from the active transducer pair which was located at the 6.12 m position on the 45° leg are shown on Figures A-7 and A-8. Tracing equivalence between the two transducers during the positive phase was judged to be very good. The measured peak overpressures were almost identical. However, the pressure excursion which occurs approximately 200 µs after the lead shock was more pronounced on the PCB gage than on the Kulite gage. Over a greater time period the PCB transducer appeared to exhibit a thermal excitation. The reason for this was not clear since the PCB transducer was thermally protected during the test, following the procedures described in Reference 3.

A comparison of the records from the active transducer pair located at the 6.27 m position on the 45° leg is given on Figures A-9 and A-10. Tracing equivalence in this pair of transducers was considered superior. The majority of significant pressure excursions was duplicated both qualitatively and quantitively. The pressure trace characteristics just after the time of arrival were more closely duplicated on this pair of transducers than at the 6.12 m position (Figures A-7 and A-8). In addition, the PCB transducer at the 6.27 m position did not display the long-term thermal response tnat was noted at 6.12 m. At 6.27 m, both the Kulite and PCB transducers exhibited long-term baseline shift. The Kulite transducer snifted somewhat more than the PCB. Also, the extended traces show some 60-cycle pick-up from an undetermined source.

As an additional comparison, pressure records at the 5.96, 6.12, and 6.27 meter positions along the 45° instrumentation leg are plotted together on Figures A-11 and A-12. The records are displayed in real time on Figure A-11 and with artificial shock front alignment on Figure A-12. The three records in this sequence
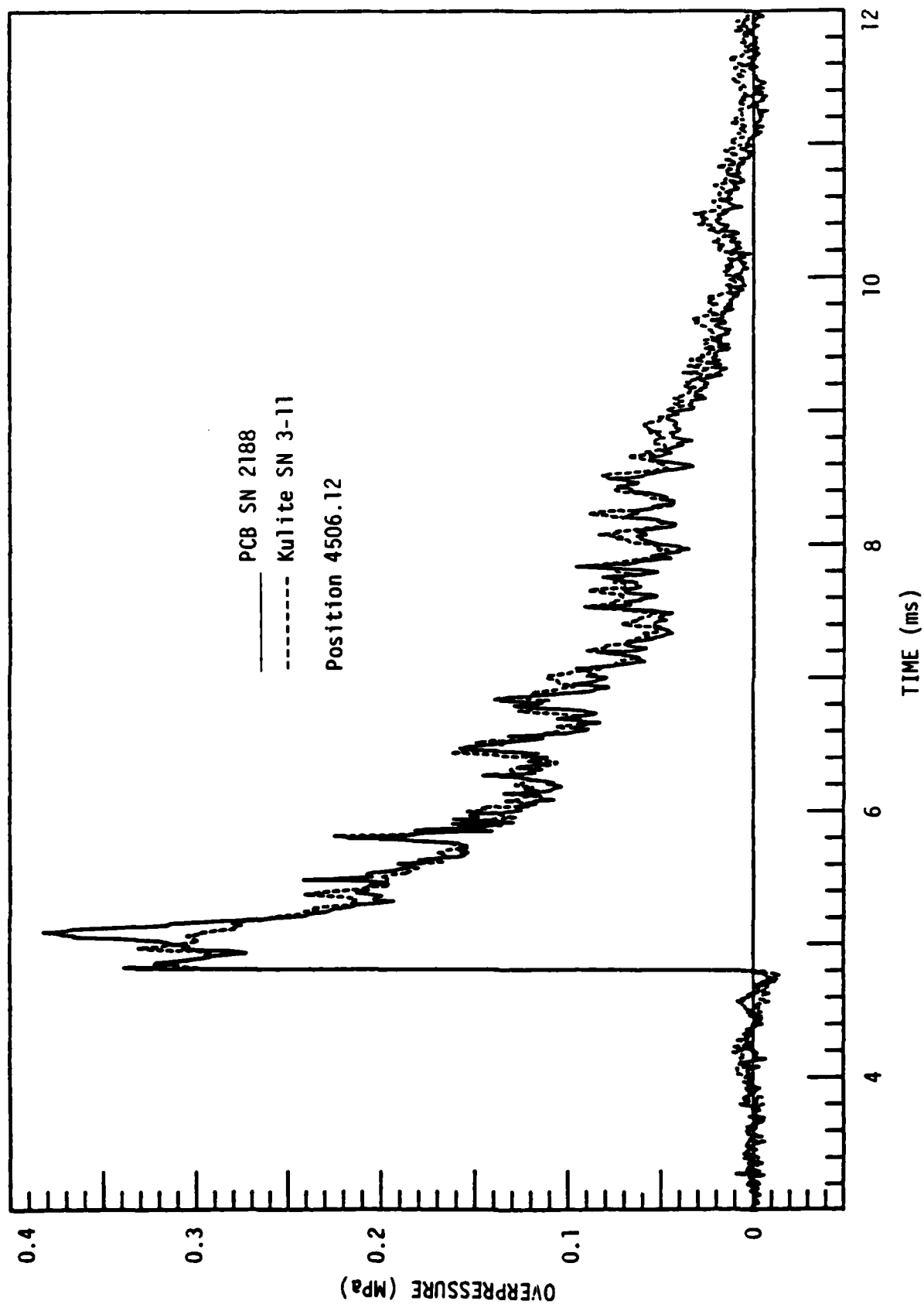
Figure A7. Comparison of pressure records from redundant pair located at R = 6.12 m on 45° leg.

110
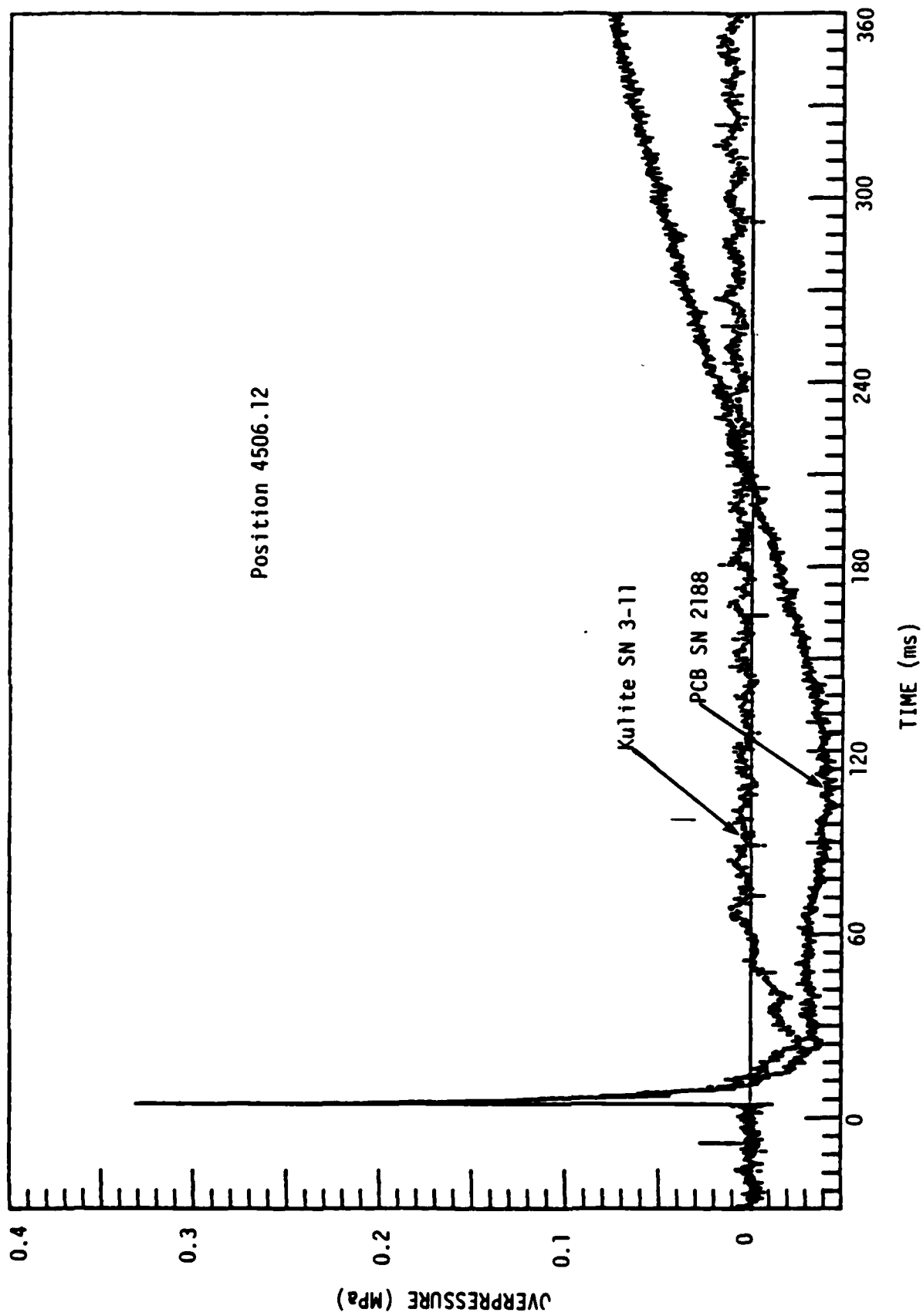
Figure A8. Comparison of pressure records from redundant pair located at R = 6.12 m, on 45° leg.

111

Figure A9. Comparison of pressure records from redundant pair located at R = 6.27 m on 45° ley.

112
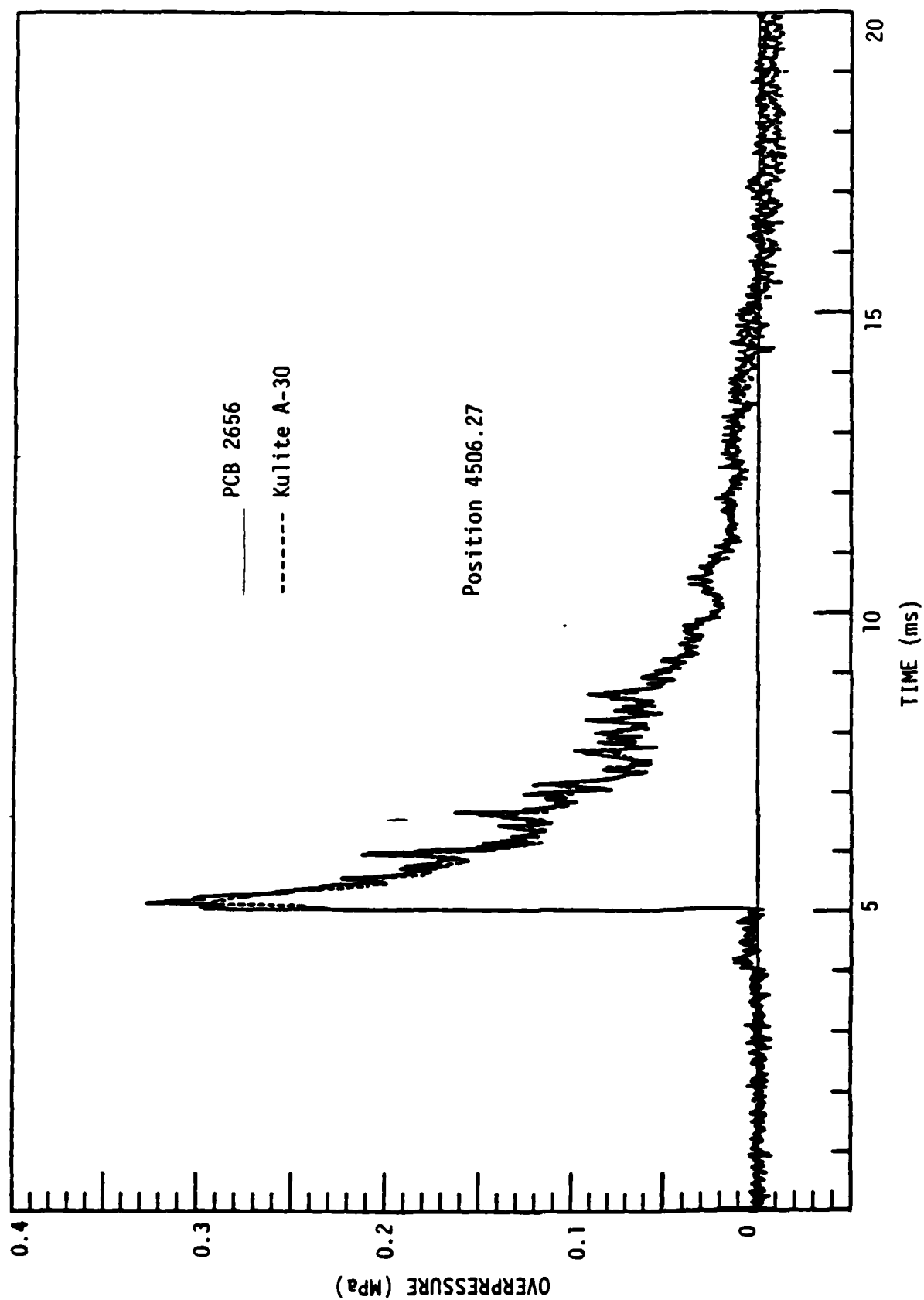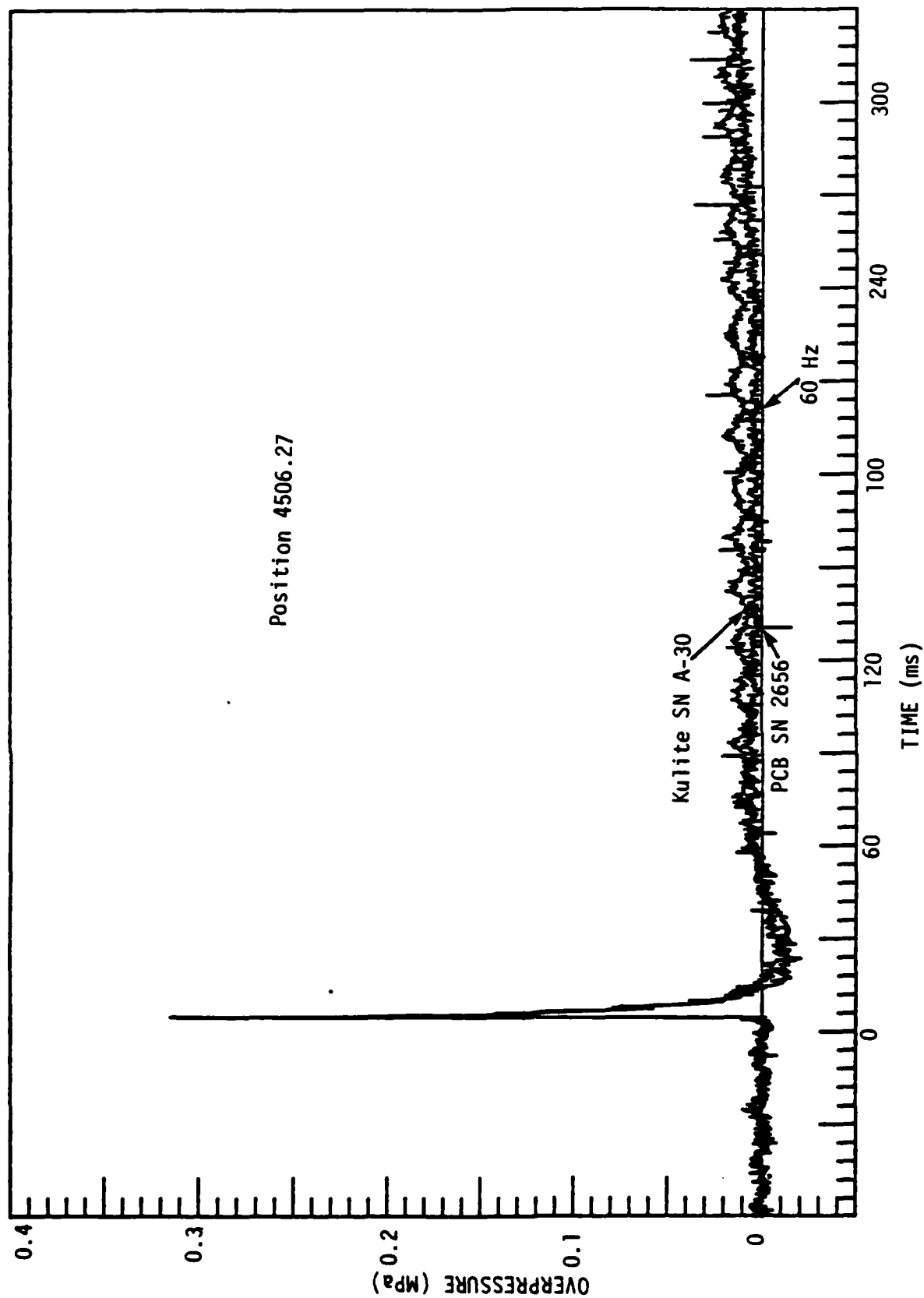
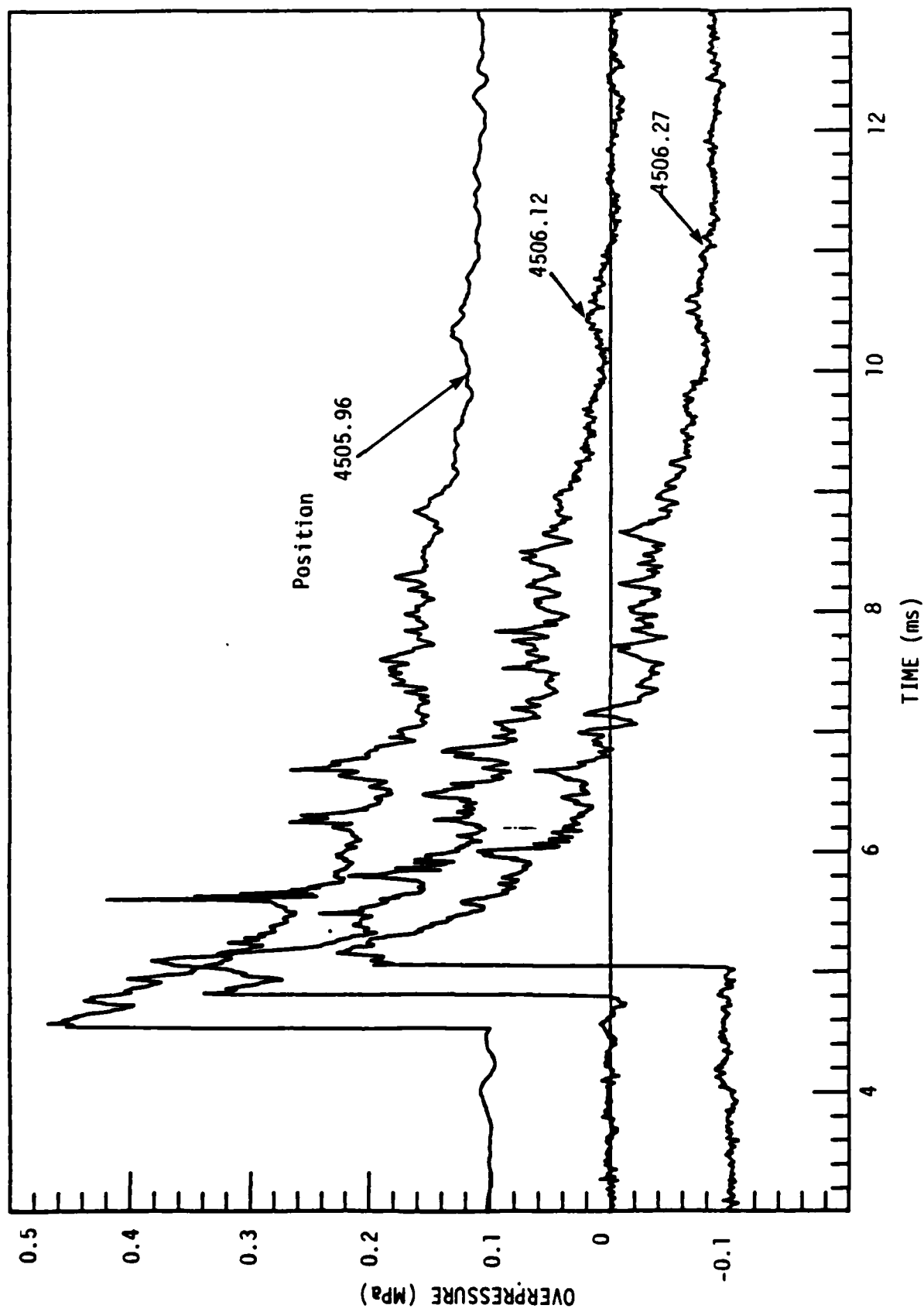Figure A10. Comparison of pressure records from redundant pair located at R = 6.27 m on 45° leg.

113

Figure A11. Comparison in real time (from H.E. initiation) of pressure records on 45° leg at R = 5.96, 6.12, and 6.27 m.

114
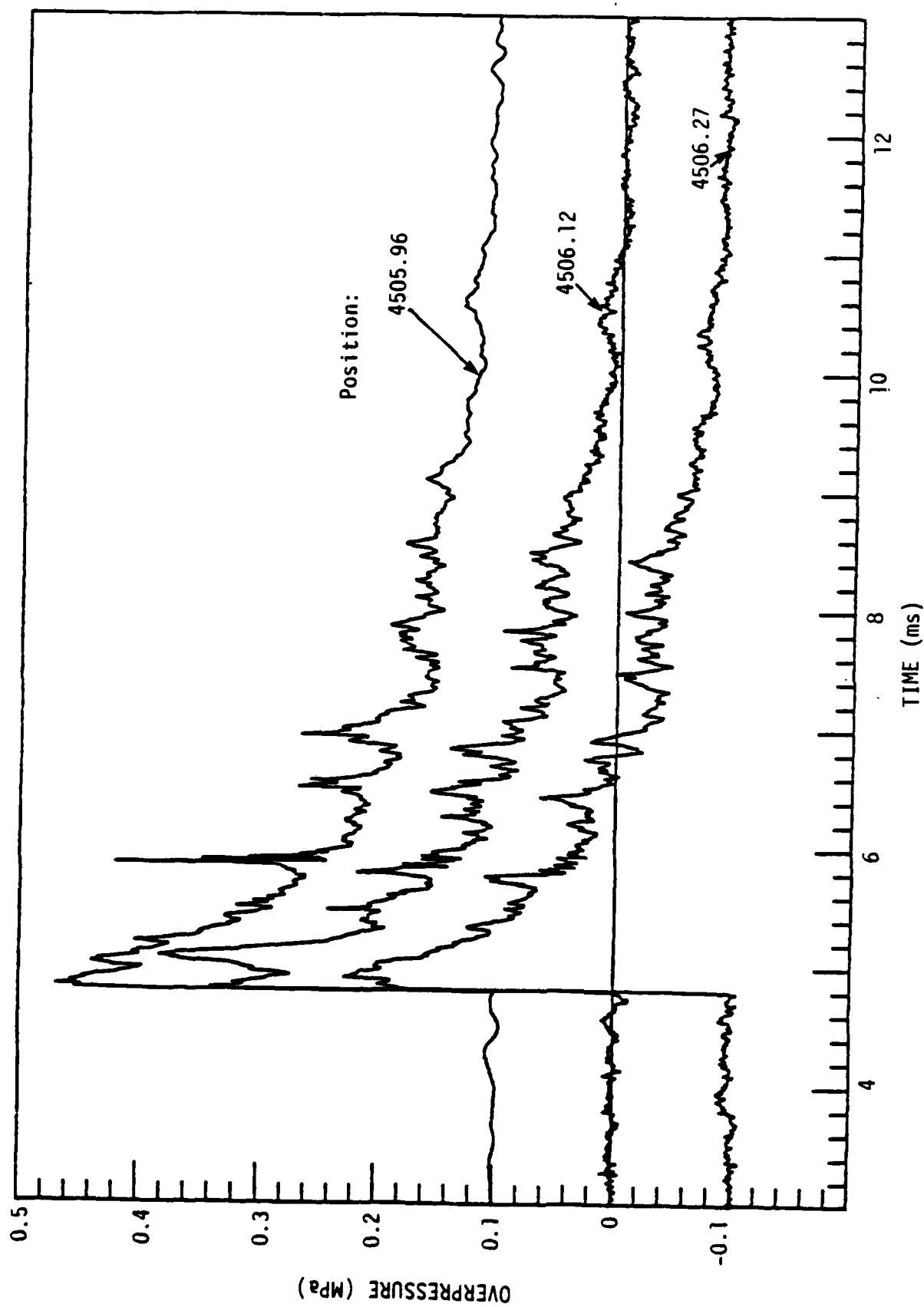
Figure A12. Comparison of pressure records on 45° leg at R = 5.96, 6.12, and 6.27 m. Shock fronts have been aligned artificially.

115

of transducer positions are qualitatively similar. (Certain wave groups of pressure excursions can be identified which appear to be approaching the lead shock. On Test CT-1, there appeared to be no individual excursions with a significant amount of impulse at this range.) Note that the pressure record at the 5.96-meter position was obtained by recording the transducer output directly onto a transient recorder, while the pressure records at the 6.12 and 6.27-m positions were recorded on tape. The high frequency, low amplitude noise which appears on the latter two transducer records is attributed to the tape recorder.

The conclusions from Test CT-1 were as follows: (1) the transducer mounting blocks used in conjunction with the new 45° instrumentation leg were judged to perform as well as or better than the mounting plates used with the other two instrumentation legs; (2) the vent hole used with the dummy gage mounting blocks would be deleted; and (3) in terms of transducer response over time periods associated with the positive phase in small-scale FAE experiments, performance of the Kulite and PCB transducers was judged to be reasonably equivalent.

DISTRIBUTION LIST

DEPARTMENT OF DEFENSE

Assistant to the Secretary of Defense
Atomic Energy
    ATTN: Executive Assistant

Defense Intelligence Agency
    ATTN: DB-4C
    ATTN: DT-1C
    ATTN: DT-2

Defense Nuclear Agency
        ATTN: SPTD
2 cy ATTN: SPSS
4 cy ATTN: STTI/CA

Defense Technical Information Center
12 cy ATTN: DD

Department of Defense Explo Safety Board
    ATTN: Chairman

Field Command/DNA, Det 1
Lawrence Livermore National Lab
    ATTN: FC-1

Field Command
Defense Nuclear Agency
    ATTN: FCPR
    ATTN: FCTT, W. Summa
    ATTN: FCT
    ATTN: FCTT
    ATTN: FCTXE

Field Command Test Directorate
    ATTN: FCTC

Joint Strat Tgt Planning Staff
    ATTN: JLAA
    ATTN: JPST

Under Secy of Def for Rsch & Engrg
    ATTN: Strategic & Space Sys (OS)

DEPARTMENT OF THE ARMY

Chief of Engineers
    ATTN: DAEN-MPE-T
    ATTN: DAEN-RDL

Harry Diamond Laboratories
    ATTN: DELHD-NW-P
    ATTN: 00100 Commander/Tech Dir/Div Dir

US Army Ballistic Research Labs
    ATTN: DRDAR-BLA-S, Tech Library
    ATTN: DRDAR-BLT, J. Keefer
    ATTN: DRDAR-BLT, W. Taylor

US Army Concepts Analysis Agency
    ATTN: CSSA-ADL, Tech Library

US Army Engr Waterways Exper Station
    ATTN: WESSD, J. Jackson
    ATTN: Library
    ATTN: WESSA, W. Flathau

DEPARTMENT OF THE ARMY (Continued)

US Army Material & Mechanics Rsch Ctr
    ATTN: Tech Library

US Army Materiel Dev & Readiness Cmd
    ATTN: DRXAM-TL, Tech Library

US Army Mobility Equip R&D Cmd
    ATTN: DRDME-WC, Tech Library

US Army Nuclear & Chemical Agency
    ATTN: Library
    ATTN: MONA-OPS, J. Kelley

US Army Missile Command
    ATTN: Documents Section

DEPARTMENT OF THE NAVY

David Taylor Naval Ship R&D Ctr
        ATTN: Code 1844
        ATTN: Code L42-3, Library
        ATTN: Code 17
        ATTN: Code 1770
2 cy ATTN: Code 1740.5, B. Whang

Naval Civil Engineering Laboratory
    ATTN: Code L51
    ATTN: Code L51, J. Crawford

Naval Electronic Systems Command
    ATTN: PME 117-21

Naval Facilities Engineering Command
    ATTN: Code 04B

Naval Material Command
    ATTN: MAT 08T-22

Naval Research Laboratory
    ATTN: Code 2627, Tech Library

Naval Sea Systems Command
    ATTN: SEA-09G53, Library
    ATTN: SEA 55X

Naval Surface Weapons Center
    ATTN: Code R15
    ATTN: Code F31
    ATTN: Code R14
    ATTN: Code R40, I. Blatstein

Naval Surface Weapons Center
    ATTN: Tech Library & Info Svcs Br

Ofc of the Deputy Chief of Naval Ops
    ATTN: NOP 03EG
    ATTN: NOP 981

Office of Naval Research
    ATTN: Code 474, N. Perrone

Strategic Systems Project Office
    ATTN: NSP-272
    ATTN: NSP-43, Tech Library

117

DEPARTMENT OF THE AIR FORCE

Air Force
        ATTN: Int

Air Force Geophysics Laboratory
        ATTN: LWH, H. Ossing

Air Force Institute of Technology
Air University
        ATTN: Library

Air Force Systems Command
        ATTN: DLW

Air Force Weapons Laboratory
        ATTN: NTE, M. Plamondon
        ATTN: NTES
        ATTN: SUL
        ATTN: NTEO
        ATTN: NTED, E. Seusy

Air University Library
        ATTN: AUL-LSE

Ballistic Missile Office/DAA
        ATTN: ENBF, D. Gage
        ATTN: PP
 2 cy ATTN: ENSN

Deputy Chief of Staff
Research, Development, & Acq
        ATTN: AFRDQI

Strategic Air Command
        ATTN: NRI/STINFO Library
        ATTN: DOTP

DEPARTMENT OF ENERGY

Department of Energy
Albuquerque Operations Office
        ATTN: D. Richmond
        ATTN: CTID

Department of Energy
Office of Military Application
GTN
        ATTN: OMA/RD&T

Department of Energy
Nevada Operations Office
        ATTN: Doc Con for Tech Library

OTHER GOVERNMENT AGENCY

Central Intelligence Agency
        ATTN: OSWR/NED

NATO

NATO School, SHAPE
        ATTN: US Documents Officer

DEPARTMENT OF ENERGY CONTRACTORS

University of California
Lawrence Livermore National Lab
        ATTN: Technical Info Dept Library

DEPARTMENT OF ENERGY CONTRACTORS (Continued)

Los Alamos National Laboratory
        ATTN: Reports Library
        ATTN: J. C. Hopkins

Sandia National Laboratories
        ATTN: Library & Security Classification Div

Sandia National Laboratories
        ATTN: Tech Library 3141

DEPARTMENT OF DEFENSE CONTRACTORS

Aerospace Corp
        ATTN: Library Acquisition M1/199

Applied Research Associates, Inc
        ATTN: N. Higgins
        ATTN: J. Bratton

Applied Research Associates, Inc
        ATTN: J. Shinn

Applied Research Associates, Inc
        ATTN: D. Piepenburg

Applied Research Associates, Inc
        ATTN: R. Frank

BDM Corp
        ATTN: T. Neighbors
        ATTN: Corporate Library

Boeing Co
        ATTN: Aerospace Library

California Research & Technology, Inc
        ATTN: M. Rosenblatt
        ATTN: K. Kreyenhagen

California Research & Technology, Inc
        ATTN: D. Orphal
        ATTN: F. Sauer

Cushing Associates
        ATTN: V. Cushing

EG&G Wash Analytical Svcs Ctr, Inc
        ATTN: Library

Electro-Mech Systems, Inc
        ATTN: R. Shunk

Electro-Mech Systems, Inc
        ATTN: L. Piper

GEO Centers, Inc
        ATTN: E. Marram

H-Tech Labs, Inc
        ATTN: B. Hartenbaum

IIT Research Institute
        ATTN: Documents Library

Institute for Defense Analyses
        ATTN: Classified Library

JAYCOR
        ATTN: Library

118

DEPARTMENT OF DEFENSE CONTRACTORS (Continued)

Kaman Sciences Corp
    ATTN: Library

Kaman Sciences Corp
    ATTN: E. Conrad

Kaman Tempo
    ATTN: DASIAC

Kaman Tempo
    ATTN: DASIAC

Lockheed Missiles & Space Co, Inc
    ATTN: T. Geers
    ATTN: Tech Library

Lockheed Missiles & Space Co, Inc
    ATTN: TIC-Library
    ATTN: S. Taimuty

Martin Marietta Denver Aerospace
    ATTN: D-6074, G. Freyer

Mitre Corp
    ATTN: MS E190

National Technical Systems
    ATTN: P. Lieberman

University of New Mexico Engineering Research
Institute
    ATTN: N. Baum
    ATTN: G. Leigh
2 cy   ATTN: D. Calhoun

Pacific-Sierra Rsch Corp
    ATTN: H. Brode, Chairman SAGE

Pacifica Technology
    ATTN: G. Kent

Physics Applications, Inc
    ATTN: F. Ford

Weidlinger Assoc, Consulting Engrg
    ATTN: M. Baron

Weidlinger Assoc, Consulting Engrg
    ATTN: J. Isenberg

Weidlinger Assoc, Consulting Engrg
    ATTN: A. Misovec

Physics International Co
    ATTN: Tech Library
    ATTN: E. Moore

R&D Associates
    ATTN: C. Lee
    ATTN: Tech Info Ctr
    ATTN: D. Simons
    ATTN: J. Lewis
    ATTN: P. Haas

Rand Corp
    ATTN: P. Davis

Rand Corp
    ATTN: B. Bennet

S-CUBED
    ATTN: Library
    ATTN: D. Grine
    ATTN: T. Pierce
    ATTN: M. Groethe

Science Applications, Inc
    ATTN: Tech Library

Science Applications, Inc
    ATTN: M. Knasel
    ATTN: W. Layson
    ATTN: J. Cockayne

Southwest Research Institute
    ATTN: A. Wenzel
    ATTN: W. Baker

SRI International
    ATTN: J. Colton
    ATTN: G. Abrahamson

Structural Mechanics Associates, Inc
    ATTN: R. Kennedy

Teledyne Brown Engineering
    ATTN: F. Leopard
    ATTN: D. Ormond

TRW Electronics & Defense Sector
    ATTN: D. Baer
    ATTN: Technical Information Center
2 cy   ATTN: N. Lipner

TRW Electronics & Defense Sector
    ATTN: E. Wong
    ATTN: P. Dai

120

END

FILMED

5-85

DTIC